8-27-2010

Climate Impacts of Land Cover and Land Use Changes in Coastal Tropical Regions Under Conditions of Global Climate Change

Daniel E. Comarazamy
Santa Clara University

Santa Clara University

Department of Mechanical Engineering

Date: August 27, 2010

I HEREBY RECOMMEND THAT THE THESIS PREPARED UNDER MY SUPERVISION BY

Daniel E Comarazamy

ENTITLED

Climate Impacts of Land Cover and Land Use Changes in Coastal Tropical Regions Under Conditions of Global Climate Change

BE ACCEPTED IN PARTIAL FULFILLMENT OF THE REQUIREMENTS FOR THE DEGREE

OF

DOCTOR OF PHILOSOPHY IN MECHANICAL ENGINEERING

Thesis Advisor	Thesis Reader
Chairman of Department	Thesis Reader
	Thesis Reader
	Thesis Reader

Climate Impacts of Land Cover and Land Use Changes in Coastal Tropical Regions Under Conditions of Global Climate Change

By

Daniel E Comarazamy

Dissertation

Submitted in Partial Fulfillment of the Requirements
for the Degree of Doctor of Philosophy
in Mechanical Engineering
in the School of Engineering at
Santa Clara University, 2010

Santa Clara, California

Acknowledgements

This research was partially funded by the Graduate School of Engineering at Santa Clara University, by the EPSCoR program of the University of Puerto Rico, and by NOAA-CREST (grant number NA06OAR4810162). The atmospheric model simulations were performed at the High Performance Computing Facility of the University of Puerto Rico at Río Piedras. The Airborne Thermal and Land Applications Sensor (ATLAS) data was processed at the Global Hydrology and Climate Center, Huntsville, AL, under the supervision of Dr. Douglas Rickman and the assistance of Ana J. Picón. The National Centre for Environmental Prediction (NCEP) provided Reanalysis data by the NOAA-CIRES Climate Diagnostic Center (CDC) in Boulder, Colorado via their NOMADS web servers. The CDC also provided the COOP stations data thru the Southeastern Regional Climate Center CIRRUS website. The NOAA-CICS Smith and Reynolds extended reconstructed sea surface temperature (ERSST) dataset was also obtained from the NOMADS servers, Dr. Thomas Smith was instrumental in processing and handling the ERSST data.

Last, but certainly not least, I would like to thank of all those whose direct, or indirect involvement helped bring this research to completion.

Climate Impacts of Land Cover and Land Use Changes in Coastal Tropical Regions under Conditions of Global Climate Change

Daniel E Comarazamy

Department of Mechanical Engineering
Santa Clara University
Santa Clara, California
2010

ABSTRACT

The work presented in this document is an investigation of the climate impacts of land cover and land use (LCLU) changes in coastal tropical regions under conditions of global climate change (global warming, GW) using the Regional Atmospheric Modeling System (RAMS) as the main research tool, and taking the northeastern region of the Caribbean island of Puerto Rico as the test case. To achieve this goal an ensemble of climate simulations were performed, combining two LCLU and two GW scenarios. Reconstructed agricultural maps combined with reconstructed sea surface temperatures (SST) form the Past (1951-1956) climate scenario, while the Present (2000-2004) scenario was supported with high-resolution remote sensing data. The climate reconstruction approach is validated with observational data from surface weather stations for both timeframes. Results indicate that LCLU changes produced the largest air temperature differences over heavily urbanized regions and that these changes occur near the surface. The influence of the global warming signal is to induce a positive inland gradient for maximum temperature, possibly due to increased trade winds in the present climatology. In terms of minimum temperatures, the global warming signal induces temperature increases along the coastal plains and inland lowlands. The global warming signal also produced stronger trade winds with an easterly-southeasterly direction. These

changes cause a shift in the location of a convergence zone north of the Central Mountains, where without orographic lifting clouds have higher bases and the total column liquid water content is decreased above higher elevations. This combination of factors translates into a dramatic decrease in surface accumulated precipitation in the highlands of the region of interest due to global climate change. Regarding the combined effects of LCLU changes and global warming, results indicate that the impact of LCLU changes on temperatures, total column liquid water content, and surface accumulated precipitation are relatively independent of the large-scale climate conditions, and vice versa.

TABLE OF CONTENTS

LIST OF FIGURES

LIST OF TABLES

Nomenclature

Symbols	
u, v, w	Horizontal and vertical wind components
θ	Potential temperature
π	Exner function
f	Coriolis parameter
K	Eddy viscosity coefficient for momentum (m), heat and moisture (h)
g	Gravity
r	Water species mixing ratio
R	Shortwave (s) and longwave (l) atmospheric radiative fluxes
C	Volumetric specific heat
ρ	Density
Δz	Vertical layer depth
α	Albedo
λ	Soil thermal diffusivity
τ	Shortwave transitivity through the vegetation layer
Subscripts	
il	Ice-liquid
n	Water categories
g	Ground surface
a	Air
veg	Vegetation layer
*	Surface layer fluxes

Chapter 1

Introduction

Human activity has profound climate and environmental impacts. Most of these impacts are considered to have negative effects on living conditions on planet Earth, and therefore require especial attention for humans to have the ability of producing adequate adaptation and mitigation policies (depending on the scale and severity of such impacts). The scales of these impacts range from global, to regional, to local and include, but are not limited to, changes in the atmospheric composition and radiative forcing, global warming, effects on the water cycle, ocean changes and rising sea levels, ecosystems modifications, among many others.

At the global scale, the link between human activities and climate change is well documented and widely studied, with the most prominent a marked increase in global average temperatures, i.e., global warming, mainly due to an increase of anthropogenic emissions of atmospheric greenhouse gases (IPCC, 2007; Trenberth et al., 2007 [see Figures 1.1 and 1.2]). Nevertheless, our understanding of the contribution of local and regional anthropogenic factors, like changes in land cover and land use (LCLU), to the observed climate change at specific locations, within the above mentioned conditions of global climate change, is incomplete, yet critical to determine how the environment's atmosphere-ocean-land components interact in a connected system. This leads to the major fundamental question to be answered by this research: What is the individual and combined regional climate impact of local anthropogenic environmental changes, namely

in the form of LCLU changes, and global anthropogenic-induced atmospheric and oceanic changes, e.g., global warming and increased sea surface temperatures (SST).

In this sense, tropical coastal regions represent one of the most interesting cases to study the climate impacts of local and regional LCLU changes under conditions of global climate change over a limited geographical area because these are regions in which global, regional and local effects converge through general atmospheric and oceanic circulations, large urban centers and population dynamics, pristine rain forests, deforestation, reforestation, and other factors that may have an impact on, or are impacted by, climate (Ray et al., 2006; Van der Molen et al., 2006; Velazquez-Lozada et al., 2006). Because of this unique combination of factors, the Caribbean, Mesoamerica, Southeast Asia, the Philippines, and other tropical coastal regions represent a major part of the global biodiversity hotspots and thus require focused attention (Myers et al., 2000). Moreover, the northeastern region of the Caribbean island of Puerto Rico offers a unique opportunity for this kind of study because of the close proximity of the San Juan Metropolitan Area (SJMA), Luquillo Experimental Forest (LEF, hereon referred to as El Yunque), and Central Mountain range, because of evidence of global and local effects on regional climate, historical LCLU practices that include changes in agricultural patterns, urban sprawl, deforestation, and reforestation, and equally important, the availability of a long-term, reliable observational climate dataset from a large network of surface weather stations. As such, the northeastern region of Puerto Rico is taken as the test case to study the climate impacts of LCLU changes in coastal tropical regions under conditions of global climate change.

Furthermore, the northeastern coast of Puerto Rico shows an interesting contradictory pattern when comparing long-term daily minimum and maximum temperatures averaged over the entire island with the trends averaged over the SJMA (Figure 1.3). From 1950 to 2006, the island-wide trend shows decreasing maximum temperatures and increasing, if only slightly, minimum temperatures, whereas the SJMA shows a pronounced increase in both daily maximum and minimum temperatures. This trend, especially the increase in maximum temperatures, might be due to the strong and increasing Urban Heat Island (UHI) effect generated by the rapid growth of the SJMA (~19% growth in 50 years, see Figure 1.4) (Duchon, 1986; Velazquez-Lozada et al., 2006), one of the largest and most heavily urbanized cities in the Caribbean. The UHI is defined as a dome of high temperatures observed over urban centers as compared to the relatively low temperatures of the rural surroundings (Landsberg, 1981; Oke, 1987). Some of the factors that lead to the formation of a heat island are the widespread use of diverse construction materials (e.g., concrete, asphalt, steel, glass); as the city grows the area where the weather station is located is increasingly enveloped by these materials, possibly producing the increasing trend in air temperatures recorded by those stations. Although this would be an important aspect of the theory, it does not take into account what would be the contribution of global warming and other phenomena associated with global climate change, like changes in Sea Surface Temperatures (SSTs), trade wind patterns, evaporation, and moisture availability, among others, to this observed temperature increase. This question, and the type of possible added and competing effects

that it carries, are the main focus of this research and are addressed throughout this document.

In the next Chapter, background information on the topic of urban heat islands, LCLU changes, and their effects on tropical coastal regions and Puerto Rico, as well as how global climate change is reflected in the region of interest, are given. Chapter 3 expands on the fundamental research questions and explains the methodology used in this research to answer those questions, which employs a regional atmospheric model as the main research tool, and includes a description and analysis of the LCLU data used. The atmospheric model chosen is the Regional Atmospheric Modeling System (RAMS); results from control runs were validated for accuracy and reliability against observations (Chapter 4), and a simulation matrix was performed to study the individual and combined effects of LCLU changes and global warming in northeastern Puerto Rico (Chapter 5). In Chapter 6 the major findings of this research are summarized, with recommendations for future work, possible implications in related fields, and other tropical coastal regions were the methodology could be applied and be useful.

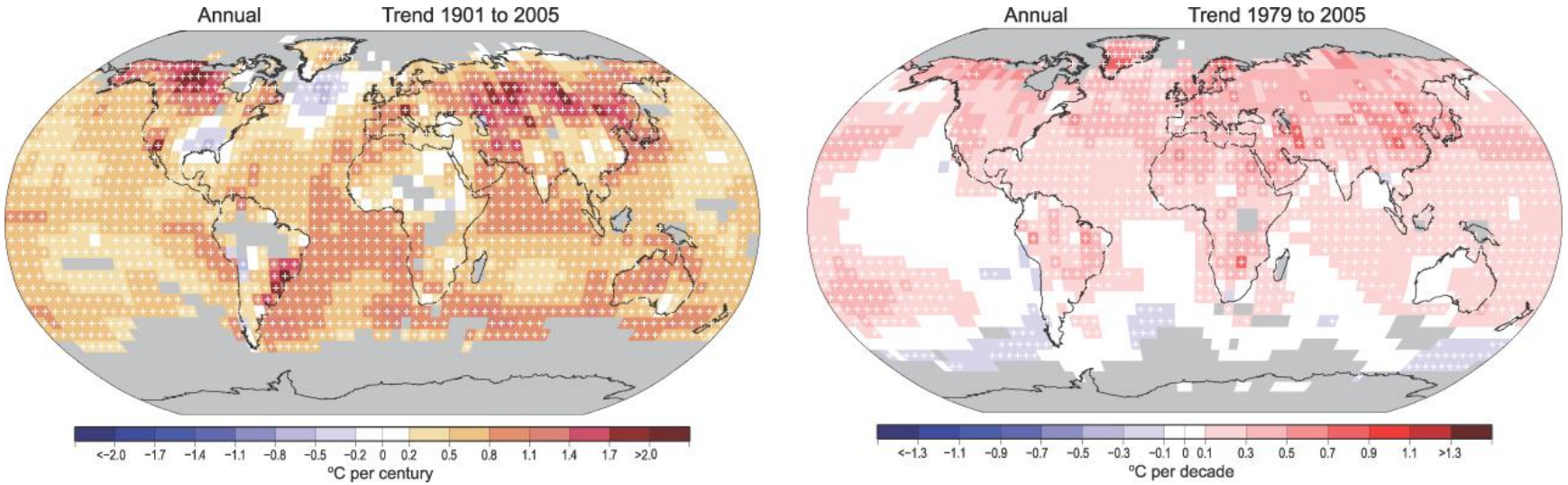

Figure 1.1: Linear trend of annual temperatures for 1901 to 2005 (left panel, °C per century) and 1979 to 2005 (right panel, °C per decade). Areas shaded in grey have insufficient data to produce reliable trends. Trends significant at the 5% level are indicated by white + marks (from Trenberth et al., 2007).

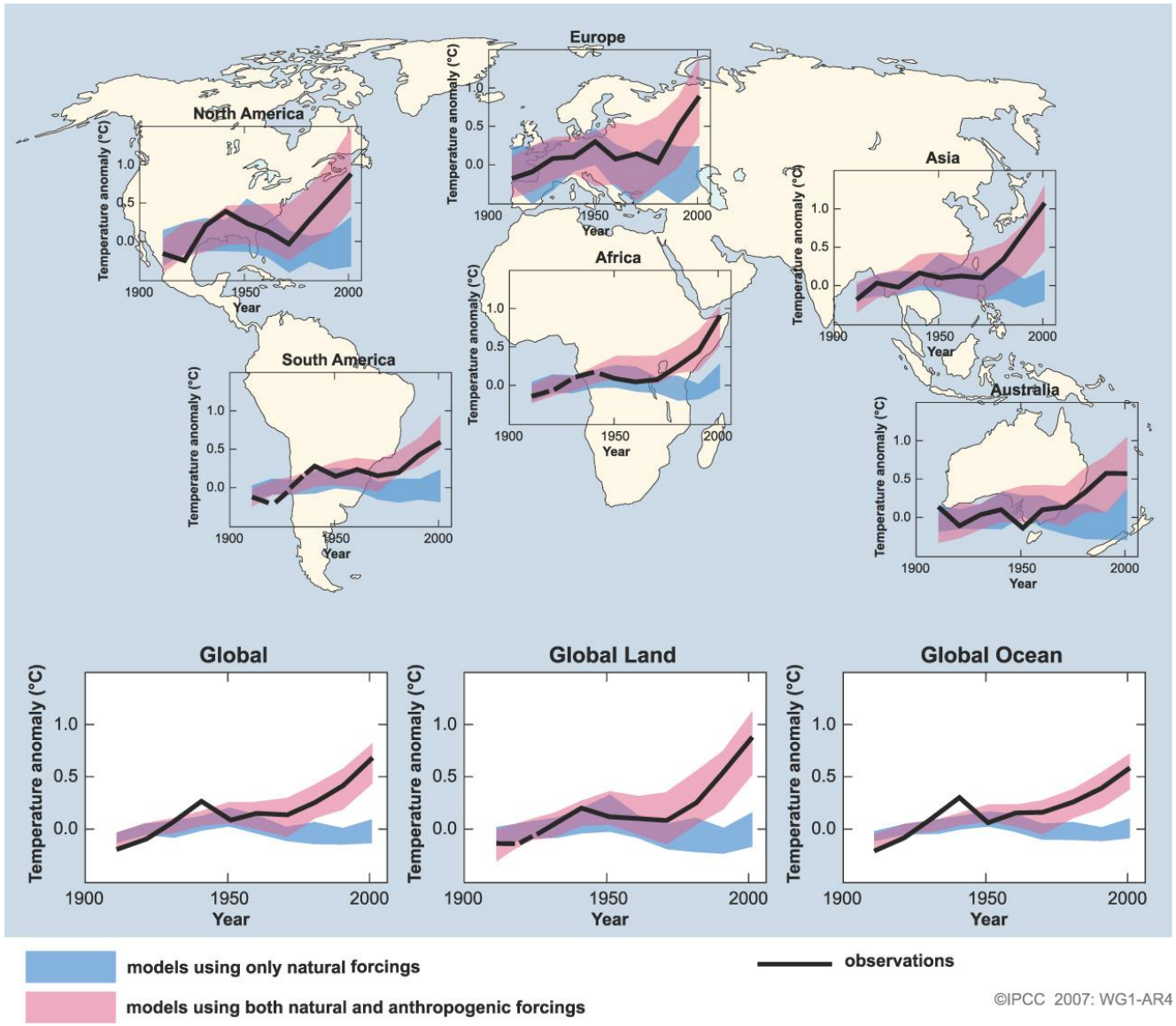
Europe
North America
Asia
Africa
South America
Australia
Temperature anomaly (°C)
Year
1900
1950
2000
1.0
0.5
0.0
Global
Global Land
Global Ocean
models using only natural forcings
models using both natural and anthropogenic forcings
observations
©IPCC 2007: WG1-AR4

Figure 1.2: Comparison of observed continental and global changes in surface temperature with results simulated by climate models using natural and anthropogenic forcings. Decadal averages of observations are shown for the period 1906 to 2005 (black line) plotted against the centre of the decade and relative to the corresponding average for 1901–1950. Lines are dashed where spatial coverage is less than 50%. Blue shaded bands show the 5–95% range for 19 simulations from five climate models using only the natural forcings due to solar activity and volcanoes. Red shaded bands show the 5–95% range for 58 simulations from 14 climate models using both natural and anthropogenic forcings (from IPCC, 2007).

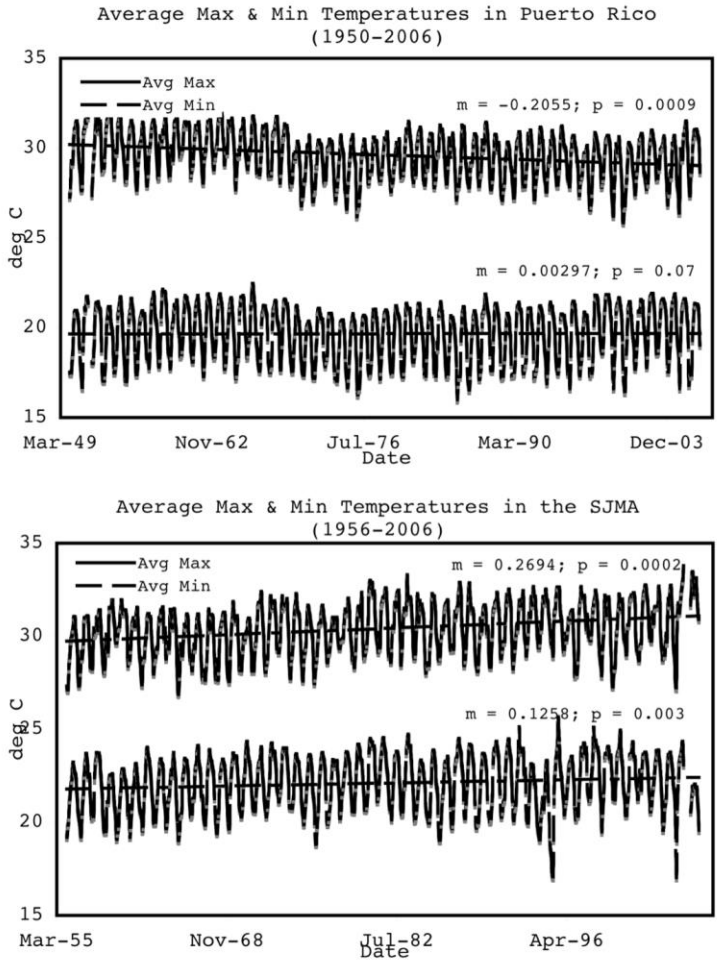

Figure 1.3: Time series and linear regression trend of daily maximum and minimum temperatures for 1950 to 2006 averaged over 26 surface COOP stations located throughout Puerto Rico (top panel) and 1956 to 2006 averaged over those stations located within the SJMA (bottom panel). Linear regression slopes, *m*, are ˚C per decade. Statistical significance *p* values are also shown. For more information on the climate data from which the plot was constructed see Section 4.1.

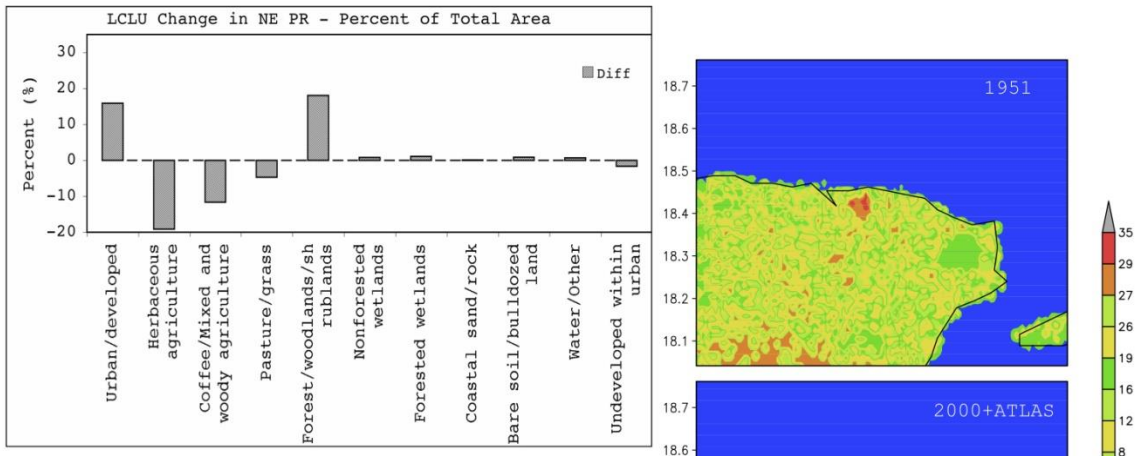

Northeastern Puerto Rico

Description	class	1951	2000	Diff
Background/water	0			
Urban/developed	30	1.92	17.81	15.89
Herbaceous agriculture	8	19.19	0.09	-19.10
Coffee/Mixed and woody agriculture	12	12.38	0.76	-11.62
Pasture/grass	27	33.73	28.99	-4.74
Forest/woodlands/shrublands	3	9.37	27.43	18.06
Nonforested wetlands	16	0.00	0.76	0.76
Forested wetlands	19	0.00	1.08	1.08
Coastal sand/rock	26	0.00	0.14	0.14
Bare soil/bulldozed land	29	0.00	0.91	0.91
Water/Other	1	0.23	0.93	0.70
Undeveloped within urban	7	1.71	0.00	-1.71

Figure 1.4: Map showing the LCLU specifications in northeastern Puerto Rico for 1951 and 2000 (right panels), the 2000 information is complemented with remote sensing data obtained from the ATLAS sensor. Histogram of historical LCLU changes in percent of total area covered from 1951 to 2000 (top left panel) and description of the most relevant vegetation and land classes with percent change and conversion rates (bottom left panel).

Chapter 2

Literature Review

In building the background information in the topic of climate impacts of LCLU changes, the starting point should be one of the most extreme cases of environmental change that has been the focal point of both policymaking and scientific research over resent years: urbanization. The clearest indicator of climate changes due to urbanization is a well-known urban/rural convective circulation known as urban heat islands (UHI). The urban heat island is defined as a dome of high temperatures observed over urban centers as compared to the relatively low temperatures of the rural surroundings (Landsberg, 1981; Oke, 1987).

As mentioned before, some of the factors that lead to the formation of a heat island are the widespread use of diverse construction materials, such as concrete, asphalt, steel, glass, among many others. Materials used in cities have a much higher thermal inertia than natural vegetation-covered surfaces, resulting in large differences in temperature during the first several hours after sundown, when all the energy absorbed and stored during daylight is released to the lower atmosphere over the city. Tall, vertical surfaces and other geometric shapes of the urban landscape create what is known as the canyon effect (Grimmond and Oke, 1999; Masson, 2000; Martilli et al., 2002), another aspect of the UHI effect. In the spaces between buildings, long-wave radiation emitted by the surface at night is reflected and absorbed by the walls, resulting in trapped energy and

higher temperatures. The urban topography also interrupts wind flows and results in decreased heat loss. Paved surfaces prevent precipitation from entering the soil and subsoil, resulting in less moisture available in green areas for evapotranspiration, a non-radiative air-cooling phenomenon. These temperature contrasts are greater in clear and calm conditions, and tend to disappear in cloudy and windy weather by effects of thermal and mechanical mixing.

The UHI was first recognized in London in 1820 when observations showed that the city was up to 2.1˚C warmer at night than the surrounding countryside, and up to 0.19˚C cooler during the day (Landsberg 1981). Since then it has been widely studied and urban heat islands of diverse magnitude, and its causes and patterns, have been reported for a number of cities along with some of its most important regional and local effects (e.g., Landsberg, 1981; Jauregui and Romales, 1996; Jauregui, 1997; Noto, 1996; Dixon and Mote, 2003; Ochi et al., 2003; Rozoff et al., 2003; Inoue and Kimura, 2004; Shepherd, 2005; among many others). The majority of these previous studies rely on observational station data and satellite information, simplified numerical simulations, and idealized laboratory experiments, and focus on large continental cities, generally located in northern temperate regions, and although the general UHI pattern reported is similar, each city is exposed to diverse local and synoptic factors, which causes the study of UHI to be complex and specific of the locality. Urban heat islands in tropical regions have been identified in Kuala Lumpur, Malaysia, the island state of Singapore (Tso, 1996), and in San Juan, Puerto Rico (Velazquez-Lozada et al., 2006), by comparing historical temperature differences between urban centers and their rural surroundings, followed by

numerical simulations where the consensus in each study was that they had limited scope and analysis, were too simplified in their atmospheric modeling approach, and more work needed to be done.

Studies of LCLU changes and its associated climatic impacts in tropical coastal regions have been limited. It was recently reported that lowland deforestation is leading to increases in cloud base heights and thinner clouds in rain forests in Central America (Lawton et al., 2001; Nair et al., 2003; Ray et al., 2006), which is resulting in increases of regional droughts. Regional model simulations of pasture and forested scenarios showed that lowland and premontane deforestation increases air temperatures and sensible heat fluxes and decreases the dew point temperatures and latent heat fluxes of air masses that when lifted eventually form orographic cloud banks at higher elevations. However, a similar numerical experiment conducted in Puerto Rico reported a similar increase in cloud base height, but using a forested island (Van der Molen, 2002; Van der Molen et al., 2006), they produced apparently contradictory results. These studies concluded that under clear and calm conditions the development of the sea breeze circulation dominates atmospheric flow over the island. Forested runs produced a stronger sea breeze with a more defined convergence front and consequently with stronger updrafts transporting moisture to higher levels and thus increasing cloud base heights when compared to pasture simulations.

The alleged discrepancy on the results by these two studies is addressed in Ray et al. (2006) and settled by explaining that the effect on cloud base height is linked to the

net effect the LCLU change has on the local Bowen ratio, the ratio of energy fluxes from the ground to the atmosphere by sensible and latent heating, respectively. It was argued that as the Puerto Rican pasture fields were specified as well watered sites, even during the early rainfall season (ERS), and the forest was made to be coastal swamp forests, this resulted in the forests having less evaporation and higher sensible heat fluxes than the well watered pastures. The Costa Rican studies, on the other hand, the forests were specified with constant access to deep soil water, whereas pastures did not reach as deep, resulting in the reported increase in sensible heat flux and decreased latent heat flux in the deforestation cases.

It has also been reported that warm coastal UHI effects may induce precipitation (Shepherd and Burian, 2003; Shepherd, 2005), which in turn may be competing with the reported reduction in precipitation caused by an increase in cloud base heights in a deforested landscape (Ray et al., 2006). These combined net effects have not investigated before. Urban-induced precipitation may be attributed to enhance sensible heating of air directly in contact with the increasingly urbanized or deforested surface, which may lead to further convective destabilization of low-level air. This effect, combined with the surface convergence associated with increased surface roughness, particularly in heavily urbanized settings, lead to stronger updrafts. This would favor the formation of convective clouds and lead to increased precipitation over and downwind of these areas. On the other hand, the reduction of surface moisture that occurs as a result of a hampered evapotranspiration process, associated with the removal of water-rich biosphere, raises the lifting condensation level (LCL). In other words, drier surface conditions yield

higher cloud bases, as represented by the LCL, which will make it more difficult for moist convection to organize and for condensates to fall out and reach the ground.

It may be assumed that with such a large supplier of water vapor like the ocean, coastal tropical cities will not be affected by drought-inducing higher cloud bases, especially since moisture is being almost constantly transported inland by the synoptic-scale trade winds or by a strong sea breeze in stable stratified conditions. However, this hypothesis remains inconclusive and believed to underestimate the complexity of the competing multi-scale factors involved in these land-ocean-atmosphere interactions, and the mechanisms by which precipitation and fresh water is produced in small islands and other tropical coastal locations. These effects also include the feedbacks and interactions associated with possible changes in the hydrological cycle and those associated with changes in the interaction of the sea breeze with large coastal UHIs. The interaction between an inland UHI and a sea breeze circulation has also been somewhat neglected in tropical coastal regions, as they have been limited to mainly laboratory experiments or numerical simulations in other parts of the world (e.g., Melas et al., 1995; Noto, 1996; Cenedese et al., 2000; Cenedese and Monti, 2003; Freitas et al., 2007). Thus, a number of research questions arise regarding the understanding of these effects due to LCLU changes in tropical coastal regions under climate change conditions.

As mentioned above, Velazquez-Lozada et al. (2006) conducted an observational and numerical study that proved the existence of an UHI for the tropical coastal city of San Juan, Puerto Rico, and some of the potential impacts of increasing urbanization on

the local climate. They found that larger temperature differences between the city and the surrounding countryside were more noticeable during the Caribbean Dry and Early Rainfall Seasons, which together comprise the period from December to June, when the weather is drier and calmer at both synoptic and convective scales. The Late Rainfall Season, from September to November, is more humid and convectively active (Daly et al., 2003; Taylor et al., 2002). These results motivated the development of more extensive and wide-ranging experimental campaigns and numerical experiments with the objective of determining the particular characteristics of the San Juan Metropolitan Area (SJMA) UHI, and investigate the possible impacts of LCLU changes in tropical coastal regions. The first of these field campaigns was designated as the San Juan Atlas Mission, which took place on 11-16 February 2004 (González et al., 2005; González et al., 2006). Data from weather stations and temperature sensors deployed during the Atlas Mission revealed a strong daytime UHI consistently ranging between 7-9˚C and heavily influenced by the occurrence of short-lived and weak precipitation events, apparently modulated by the availability of soil moisture within the urban area and the thermal inertia of wet soil (both in the city and the surrounding rural areas). These conclusions are in agreement with observational studies of UHI characteristics performed at different climate zones by Imamura (2005). Here urban micrometeorological observations were carried out in different cities in different climate zones, and it was found that rural soils in wet climates produce daytime UHIs and dry-climate rural-soils produce nighttime UHIs. Daytime UHIs in wet climates are larger than nighttime values due to the high thermal inertia of wet rural soils.

The high-resolution remote sensing information obtained during an Atlas Mission was used by Comarazamy et al. (2010) to identify the geographical extension of the SJMA and to update some of the surface characteristics available in regional models to obtain a detailed, heterogeneous configuration of the SJMA (see Appendix E). The main objective was the validation of a mesoscale modeling system that would allow feasible and reliable studies of climate impacts due to LCLU changes. The Regional Atmospheric Modeling System (RAMS), driven with global reanalysis data for a 10-day simulation, yielded satisfactory results in near-surface air temperatures and vertical profiles of temperatures and wind speeds.

The impact analysis, performed with the updated SJMA configuration and an interpolated natural vegetation configuration, showed that the simulation with specified urban LCLU indexes in the bottom boundary produced higher air temperatures over the area occupied by the city, with positive values of up to 2.5ºC. Changes in the surface radiative balance in the urban case attributed to modifications in the LCLU were also shown. This additional heat source seems to motivate additional vertical advection that may be leading to possible downwind enhancement of precipitation. This was evident in a precipitation disturbance when the city is present (~0.9mm, 30% increase) captured by the model that was accompanied by increases in cloud formation and vertical advection mainly downwind of the city.

A further complication resides in the fact that UHI effects and LCLU change impacts in tropical coastal regions both occur under conditions of global climate change

and environmental change, and in the particular case of Puerto Rico in a region highly susceptible to large-scale multi-decadal oscillations. Since the late 1800s, the global average concentration of atmospheric CO_2 has been increasing and has been related to increases in air temperatures ($0.6 \pm 0.2^{\circ}C$) and changes with several other climate variables. Furthermore, the Caribbean islands are likely among the most seriously impacted regions in the world by global climate change (IPCC 2007; Trenberth et al., 2007). Historical temperature trends in Puerto Rico based on cooperative (COOP) station data show some of these impacts, as reflected in increasing daily minimum temperatures and decreasing daily maximum temperatures (Duchon, 1986; CDC data). Duchon (1986) explained the increasing trend of both daily maximum and minimum temperatures at a station located in the San Juan Airport due to sprawling urbanization and to the expansion of the local UHI, but was unable to account for the asymmetric trend in daytime and nighttime temperatures observed in stations at other locations. Dai et al. (1999) found that clouds, combined with secondary damping effects from soil moisture and precipitation, can reduce the diurnal range of surface air temperature (DTR) by 25–50%, as compared with clear-sky days over most land areas, while atmospheric water vapor increases both nighttime and daytime temperatures. Clouds greatly reduce DTR by sharply decreasing surface solar radiation, while soil moisture decreases DTR by increasing daytime surface evaporative cooling. Given the strong damping effect of clouds on the daytime maximum temperature and DTR, the well-established worldwide asymmetric trends of the daytime and nighttime temperatures and the DTR decreases during the last four to five decades are consistent with the reported increasing trends in cloud cover and precipitation over many land areas and support the notion that the hydrologic cycle has intensified.

Thus, any comprehensive study of the impacts of LCLU changes in tropical coastal regions under conditions of global warming should include a detailed analysis of the contribution of each of these factors individually and combined.

Chapter 3

Fundamental Research Questions and Methodology

Given the importance of tropical coastal regions and the relatively lack of studies that include the contribution of all factors involved at resolutions fine enough to draw strong conclusions, the following fundamental research questions are proposed as an attempt to bridge the knowledge gap in the topic of the possible climate impacts of LCLU changes in tropical coastal regions under conditions of global climate change:

1) What has been the effect of LCLU changes on the local and regional early rainfall season climate of tropical coastal regions?

2) What has been the climatic impact of global climate change on tropical coastal regions during the region's early rainfall season?

3) Under these conditions of LCLU changes and global climate change, what has been their combined effect (LCLU plus global climate change) in tropical coastal regions?

3.1 General Model Configuration

To answer these questions, an ensemble of numerical atmospheric model simulations was performed to separate the signals discussed in the previous section. The model chosen for the study is the Regional Atmospheric Modeling System (RAMS), a highly versatile numerical code developed at Colorado State University to simulate and forecast meteorological phenomena (Pielke et al., 1992; Cotton et al., 2003). The version of RAMS used in this investigation, v.4.3, contains an upgraded cloud microphysics module described by Saleeby and Cotton (2004), an advancement over the original package available in the current model release (Meyers et al., 1997). The atmospheric model formulation is found in Appendix A.

The simulations will focus on the northeastern coast of Puerto Rico, with especial interest in the San Juan Metropolitan Area (SJMA) and the Caribbean National Rainforest, and will be conducted with three grids making use of the grid nesting capabilities of the model. Grid 1 covers great part of the Caribbean basin with a horizontal resolution of 25km and 10^4 horizontal grid points. Grid 2, which is nested within Grid 1, covers the island of Puerto Rico with 3100 horizontal grid points at a resolution of 5km. Grid 3, with 9184 horizontal grid points and 1km resolution, is nested within Grid 2, is centered in the city of San Juan, and covers the SJMA, complete Luquillo Experimental Forest east of San Juan (LEF, hereon El Yunque), relatively non-developed regions west and south of the city, and ocean areas to the north (see Figure 3.1 for the horizontal grid configuration). The vertical grid structure consists of a grid spacing Δz of 30m near the surface and stretched at a constant ratio until a Δz of 1000m is reached. The depth of the model reaches approximately 25km.

To clearly identify trends in daily minimum, maximum, and mean air temperatures, accumulated precipitation, wind components, cloud cover and cloud base height, and other variables, a five-year climatology is constructed from the model results. All the runs performed will span the Caribbean Early Rainfall Season, from April to June. This is the season most convenient to study UHI effects (Velazquez-Lozada et al., 2006), and represents the end of the Dry Season and the onset of the Mid-Summer Drought (Magaña et al., 1999), a critical period in the annual hydrological cycle of the island, during which the atmospheric model has performed satisfactorily (Comarazamy and González, 2008). A spin-up time of one week will be specified at the start of each three-month simulation to allow for numerical stabilization of the atmospheric model and the numerous sub-models and parameterizations available in the modeling system. This period has been proven adequate for monthly simulations during the Caribbean ERS.

3.2 Numerical Experiments to Separate LCLU and Global Warming Signals

To answer the proposed research questions, a set of numerical simulations are configured combining two LCLU scenarios (representing current and pre-urban conditions) with two large-scale

atmospheric conditions (representing different periods of global warming and their corresponding levels of green house gases [GHGs]), resulting in the run matrix in Table 3.1.

Table 3.1: Simulation Matrix

Run ID	LCLU	Driving Conditions	Science Questions
PRESENT1*	2000+ATLAS	Present Clim. & GHG concentration	3
PRESENT2	2000+ATLAS	Past Clim. & GHG concentration	1, 3
PAST1	1951 (Pre-Urban)	Present Clim. & GHG concentration	2, 3
PAST2*	1951 (Pre-Urban)	Past Clim. & GHG concentration	1, 2, 3

*Serve as the control runs to perform model validation.

The timeframe for the present and past climatologies were selected to reduce the influence of the El Niño Southern Oscillation (ENSO) and the North Atlantic Oscillation (NAO) on the Caribbean Early Rainfall Season (ERS) climate, as identified by previous studies, in accordance with periods of major historical LCLU changes; the large-scale data are used as initial and four-dimensional (4-D) boundary conditions.

3.3 Timeframe Selection

The Caribbean early season climate is greatly influenced by variations of several important large-scale oscillations, most notably the El Niño Southern Oscillation (ENSO) index and the North Atlantic Oscillation, ENSO and NAO respectively (e.g., Chen and Taylor, 2002; Taylor et al., 2002; Malmgren and Winter, 1998). In the case of the ENSO index, the correlation is such that warm winter ENSO anomalies are related to positive ERS rainfall departures in the Caribbean basin one season after the observed Equatorial Pacific anomaly, noted as El Niño+1 years (Chen and Taylor, 2002). The relationship between NAO and the climate record was determined using the statistical Burnaby (1953) test, Malmgren et al. (1998) calculated a high inverse correlation between the winter NAO index and the standardized mean annual precipitation for five stations in Puerto Rico. Using this information, the long-term record (1950 – Present) of ENSO and NAO indices as archived by the Climate Prediction Center, was analyzed to select

two five-year periods of comparable low warm ENSO values and low NAO variability that are far removed from each other to reflect a significant change in relevant climate variables.

The five-year periods from 1955 to 1959 and from 2000 to 2004 are the best available in the long-term record, in terms of the ENSO and NAO indices, to perform the simulations proposed in the Run Matrix (Figures 3.2 and 3.3, respectively). The period of the late 1950s presents an El Niño event towards the end of the decade, making the years 1959/1960 potential El Niño+1 years; regardless, the two periods selected present a similar ENSO climatology. In terms of the NAO index, the period 2000-4 shows less variability of the index within the $\pm\sigma$ and $\pm 2\sigma$ range as compared to other periods in the record. The 1950s decade shows stronger individual warm and cold events, but has in general less variability than the rest of the data, as it stays between the $\pm 2\sigma$ bands. The two NAO timeframes do not show a clear indication of periodicity, but slight indications of periodicity are present in both periods. An analysis of the global oscillations and the Caribbean climate for the two periods selected yielded similar teleconnection results as those found in the literature. Appendix B expands on the teleconnection calculations, the physical link between the oscillation indices, and the CPC data employed to perform the analysis.

To verify that the two timeframes selected are in accordance with historical LCLU changes, a first step was carried out to analyze census data for the island of Puerto Rico taking population dynamics and housing data as a proxy for LCLU change. Population and housing have been in steady increase in the island, with fractional urban and rural population crossing after the 1960 census (Figure 3.4). These changes in population and housing presumably indicate a large increase in surface area covered by urbanization and a shift away from an agriculture-based economy (Helmer, 2004; Lugo and Helmer, 2004; Kennaway and Helmer, 2007; Martinuzzi et al., 2007), both concepts evidenced by Figure 1.4, where a ~34% increase in the surface covered by urbanization and natural vegetation (i.e., shrublands, forest, woodlands) can be seen, as well as a ~30% decrease of agricultural lands. Population in general and population density in the SJMA increased heavily since 1950, while increases in population for other cities has been steadier (Figure 3.5). A complete analysis and description of the LCLU maps used to support our hypothesis, and for updating the regional model surface characteristics, is given in the next sub-section.

Lastly, for the three major selection criteria for the timeframes to perform the atmospheric model simulations, the availability of large-scale data to drive the model does not present a major problem. Current (2000-4) and pre-urban (1955-9) conditions of atmospheric 4-D fields of air temperature, horizontal wind components, and relative humidity are provided by the NCEP Reanalysis 2.5˚ large-scale data (Kalnay et al., 1996). Past and present specifications of SSTs are derived from the Smith and Reynolds Extended Reconstruction Sea Surface Temperature (ERSST v3b [Smith and Reynolds, 2003; Smith et al., 2008]). The horizontal distribution of differences in atmospheric temperatures and SSTs in Figures 3.6 and 3.9 are shown in the geographic area covered by Grid 1 (see Figure 3.1). Figure 3.6 shows the large-scale temperature changes at the times of local overnight low and daytime high temperatures over the Caribbean region, where moderate increases in temperature are observed on the order of 1.0 to 1.8˚C, respectively; these values increase towards the north Atlantic. These changes are found to penetrate vertically from the surface to about the 700mb pressure level over the island of Puerto Rico, located at approximately 66˚ west longitude (Figure 3.7). Domain-wide trade-wind speeds changes between the two climate periods are analyzed and presented in Figure 3.8, the increases in trade wind magnitude shown have been attributed to an increase in the North Atlantic high (Angeles et al., 2007), this change in the pressure difference between the Caribbean and the North Atlantic can also be evident in the SST change, as reflected in the Caribbean basin (Figures 3.9). Changes in sea surface temperature for the ERS peak only at about 0.1-0.2˚C around the island of Puerto Rico, but increase to the northeast of the island reach values closer to 1˚C in the region covered by modeling Grid 1.

3.4 Land Cover Land Use Characteristics

The two different LCLU scenarios configured for the island of Puerto Rico and its northeastern region, Grids 1 and 2, respectively, are intended to quantify the impact of LCLU changes in the northeastern region of Puerto Rico and the SJMA during the ERS, and are based on digital maps of LCLU available for 1951 and 2000 (Kennaway and Helmer, 2007). The first configuration is designed to represent the LCLU specification in a pre-urbanized Puerto Rico. Then, one of the model sub-routines is modified to represent the present urban extension, configuration, and optical characteristics of San Juan as observed by

an ATLAS sensor (see section 3.4.2 for an extended description). The variable modified in the sub-routine for these numerical simulations is the denominated Vegetation Index (VI) defined by the Biosphere-Atmosphere Transfer Scheme (BATS, Dickinson et al., 1986); this index includes the biophysical parameters of albedo, emissivity, leaf area index, vegetation percentage, surface roughness, and root depth. The configuration of the LCLU-VI and datasets used in these simulations is explained in more details on the next sub-sections.

3.4.1 Past LCLU

Reconstruction of the past LCLU scenario is based on digital maps of historical vegetation and land cover in Puerto Rico. LCLU maps and vegetation datasets for 1951 are available and are based on old hard copy maps, satellite imagery, climatic zones, geology, elevation, and rainfall (Brockman, 1952; Ewel and Whitmore, 1973; Franco et al., 1997; Helmer et al., 2002; Kennaway and Helmer, 2007). A reclassification of these past LCLU classes was done to match the modeling grids used in this study and the land classification index system used in the BATS/LEAF scheme, one of the atmospheric model's land-atmosphere transfer schemes. Thus obtaining the pre-urban LCLU dataset used as the surface characteristics for the PAST simulations (driven with either past or present atmospheric conditions) identified in Table 3.1.

3.4.2 Present LCLU

The present LCLU scenario was processed in the same way as the past specifications, but using digital vegetation information for the year 2000 complemented with remote sensing data from the ATLAS sensor. The Airborne Thermal and Land Applications Sensor (ATLAS) was flown over San Juan, Puerto Rico during February 2004 to investigate the impact of the urban growth and landscape in the climate of this tropical city. For more details on the ATLAS sensor and the San Juan Atlas Mission, refer to Gonzalez et al. (2005 and 2006). The ATLAS sensor operates in the visual and infrared bands and can detect 15 multi

spectral channels of radiation through the visible, near infrared, and thermal spectrums. The data are corrected for atmospheric radiation effects and are georectified before any analysis is performed.

To calibrate the ATLAS data, detailed atmospheric corrections are needed, which require direct measurements of atmosphere extinction coefficients by wavelength, ATLAS instrument characteristics and calibration, and profiles of atmospheric temperatures and water vapor (provided by weather balloon launched during the mission). Rickman et al. (2000) detail the procedure for calibrating the ATLAS sensor to produce the system transfer function to convert digital values (DV) into radiance measurements. These procedures produce ATLAS data files that are in physical units of energy, which are then used to generate files that derive albedo and surface temperature. The individual flight lines were also corrected to eliminate a banding, visible when the mosaic figure was generated, by a process called shadow correction. Figure 3.10 shows the process flow chart followed for this project, including the link between the airborne remote sensing and the mesoscale atmospheric modeling.

The canopy net all-wave radiation balance (W m^{-2}), temperature (˚C), and albebo can be determined following Oke (1987). Since the visible bands and the albedo information from the ATLAS sensor were used extensively for updating the surface characteristics of the atmospheric model, detailed next in this section, a brief description of the formulation to calculate the surface aldebo is given.

The net solar radiation, R_s, at the given wavelength is given by

$$R_s = (1 - \alpha)(R_s\downarrow) , \tag{3.1}$$

where α is site albedo and $R_s\downarrow$ is the incoming solar radiation.

The albedo is defined as

$$\alpha = R_s\uparrow / R_s\downarrow , \tag{3.2}$$

where $R_s\uparrow$ is the reflected solar radiation.

As mentioned before, airborne remote sensing data was used to configure the "urban and built up" Vegetation Indices. This process was the culmination of several steps (Figure 3.10). To start, a 1km subset of the 10m ATLAS data was extracted to match the horizontal resolution of the model grid where the analysis is performed. Then the geographical extension of the SJMA was identified using bands 1-2-3 of the sensor's visible spectrum, and was estimated to have a total surface area of 435km^2. Following this information, the 1km dataset of surface albedos corresponding to the SJMA was obtained using band one of the ATLAS sensor in the thermal spectrum. Figure 3.11 shows the 10m mosaic of ATLAS-derived albedos obtained from the San Juan flight lines.

For practical reasons, it was decided to lump the SJMA albedos into five groups: <0.15, 0.16-0.20, 0.21-0.25, 0.26-0.30, and >0.31. Each middle group was given a single albedo value calculated as the average of the range of each group, and the end groups were given a value of ±0.05, respectively, from their adjacent group. This process of averaging the albedos is justified, not only to facilitate the link with the atmospheric model grid, but also because the contribution of close albedo values is expected to be similar, and the averaged albedos produced a satisfactory level of heterogeneity within the urban area and still predicted accurate temperatures (Comarazamy et al., 2010; Appendix E). Furthermore, the methodology used leaves open possible subsequent improvements and additions to the Vegetation Index, to run hypothetical scenarios and to perform simulations that test possible mitigation and adaptation strategies.

Once the SJMA albedo groups were generated, five new Vegetation Indices were created following BATS by incorporating the SJMA albedos to the existing Urban and Bare Soil VIs, while maintaining the rest of the biophysical parameters constant. These new VIs were labeled Urban1 thru Urban5. Appendix C contains the full list of VI values and their corresponding biophysical parameters. Finally, to accurately match the location of each of the Urban cells with the atmospheric model grid, a natural landmark was identified and specified in RAMS (i.e., San Juan Bay in this case); then the rest of the dataset is located to obtain the complete Urban surface configuration. This methodology results in a present LCLU configuration that closely resembles the current land development, land use, and urban sprawl

mapping in Puerto Rico (Martinuzzi et al., 2007). When incorporated to the converted 2000 vegetation map, this represents the current LCLU dataset used as the surface characteristics for the PRESENT simulations (driven with either past and present atmospheric conditions) identified in Table 3.1. Figures 3.12 and 3.13 show graphically the LCLU specifications used for each of the PAST and PRESENT simulations for Grids 2 and 3, respectively.

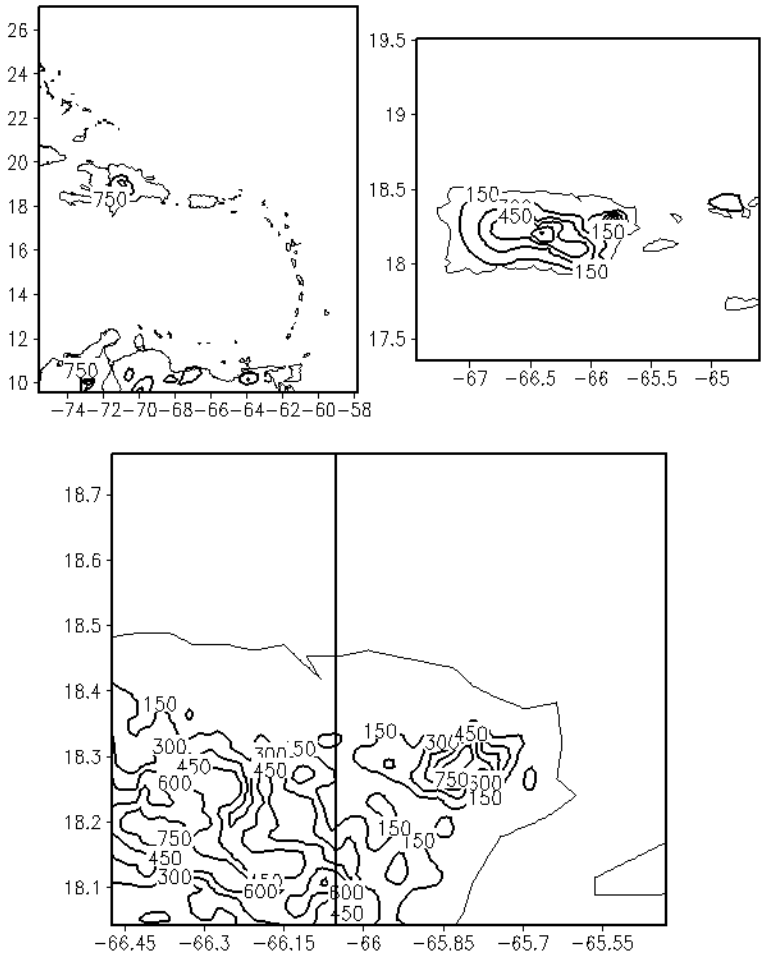

Figure 3.1: Model grids, with topography information, used in this research. Grid 1 showing the Caribbean Basin and islands (top left panel, contour interval 750m), Grid 2 covers the island of Puerto Rico and adjoining Vieques, Culebra, and Virgin Islands to the east of the domain (top right panel, contour interval 150m), and Grid 3 shows the northeastern region of Puerto Rico, the main area of interest in this research

(bottom panel, contour interval 150m). The thick solid vertical line in the bottom panel represents the location of the north-south vertical cross-section discussed in Chapter 5.

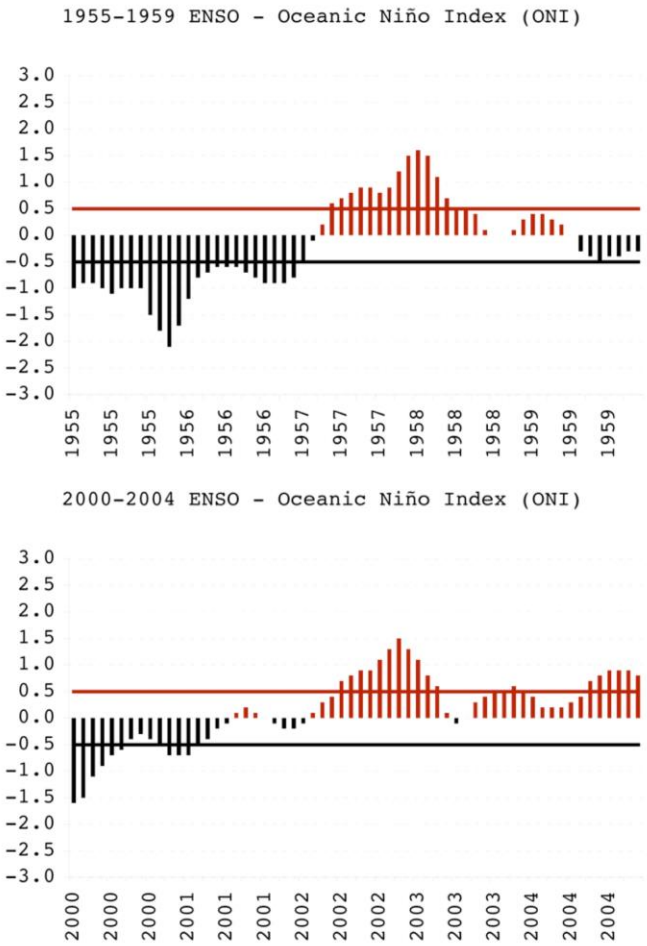

Figure 3.2: Three-point running mean of the Oceanic Niño Index (ONI) for 1955 to 1959 (top panels) and for 2000 to 2004 (bottom panels). Constructed using the bimonthly 1950 to present CPC, standardized departures from the 1950-1993 mean, dataset. Warm/cold periods, denominated as El Niño/La Niña respectively, occur when a +/-0.5˚C threshold is met for five consecutive overlapping periods, as defined by the CPC, and are represented in red/black horizontal lines in the left panels (top and bottom).

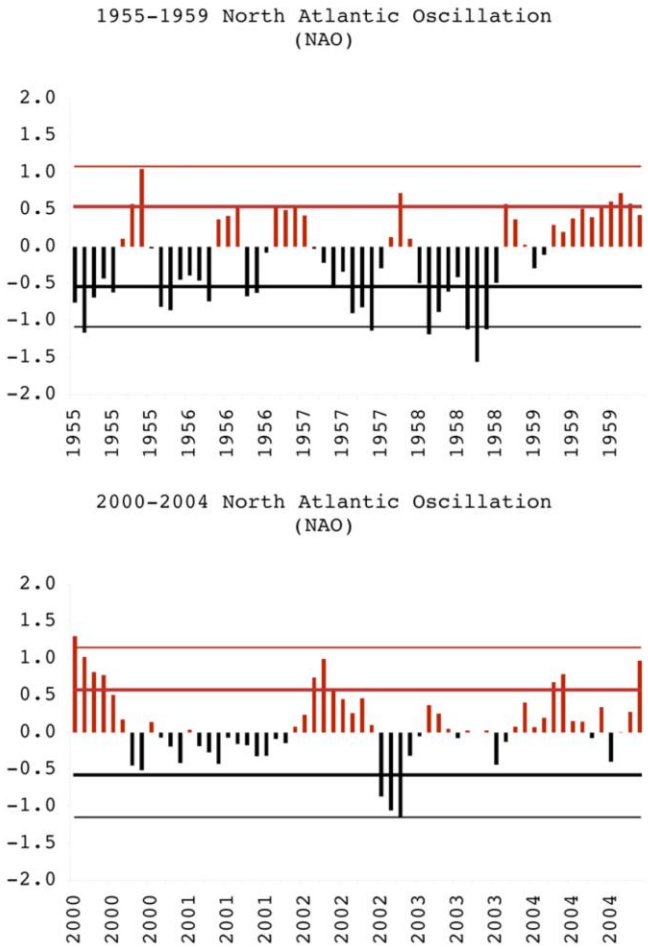

Figure 3.3: Three-point running mean of the standardized North Atlantic Oscillation Index (NAO_I) for 1955 to 1959 (top panels) and for 2000 to 2004 (bottom panels). Constructed using the daily 1950 to present CPC standardized dataset. Solid horizontal lines in the left panels (top and bottom) represent $\pm \sigma$ ($\pm$ 0.6213) and $\pm 2\sigma$ ($\pm$1.2427) calculated for the complete data record.

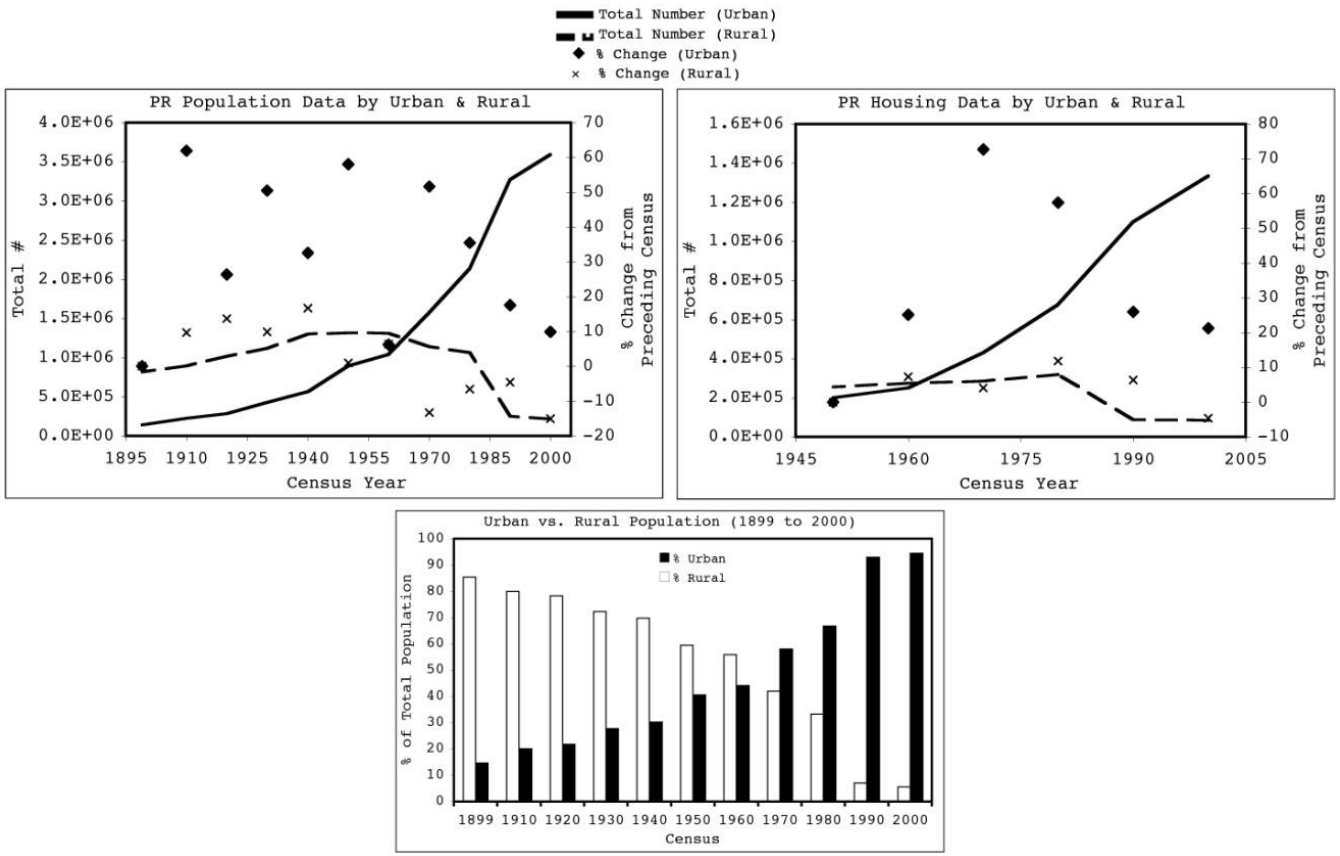

Figure 3.4: Puerto Rico population totals as number of inhabitants living in urban and rural areas for 1900 to 2000 (top left panel), total number of housing units in urban and rural areas for 1950 to 2000 (top right panel), and percent of total population living in urban and rural areas for 1900 to 2000 (bottom panel). Census data for the island of Puerto Rico provided by the US Census Bureau).

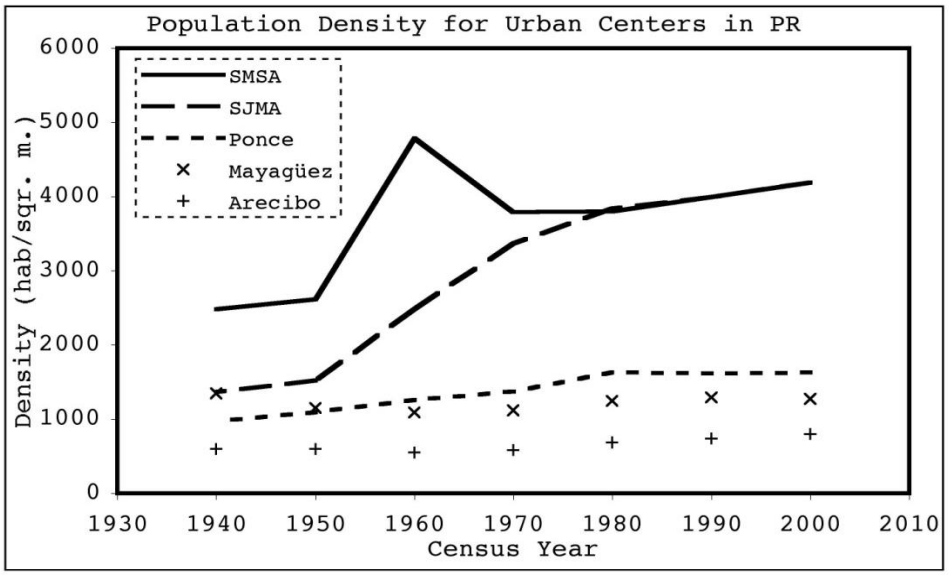

Figure 3.5: Population density data (habitants per m^2) for the four major urban centers in Puerto Rico: San Juan Metropolitan Area, Ponce (located on the south coast), Mayagüez (located on the west coast), and Areceibo (located on the northwester region). The San Juan Metropolitan Statistical Area (SMSA) is defined as the current metropolitan area for each census publication; its surface area increases as more municipalities are added with each subsequent period. The present surface area of the SJMA and SMSA are the same since the 1990 census.

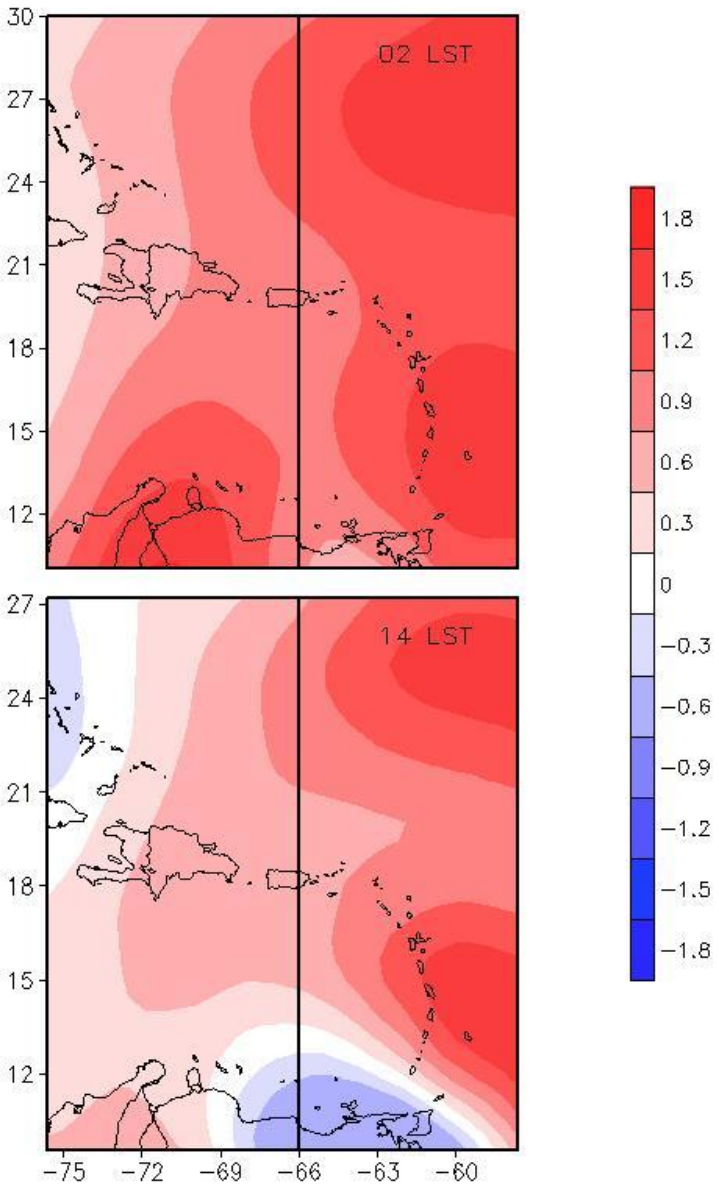

Figure 3.6: Large-scale temperature differences (˚C) between the 1955-59 and 2000-04 timeframes in the Caribbean basin calculated from the NCEP Reanalysis 2.5˚ resolution data averaged at 02 (top) and 14 local standard time (LST) (bottom), the two closest times in the four-hourly data to the local overnight low and daytime high temperatures, respectively, during the Caribbean three-month ERS. The thick solid vertical line in both panels represents the location of the north-south vertical cross-section in Figure 3.7.

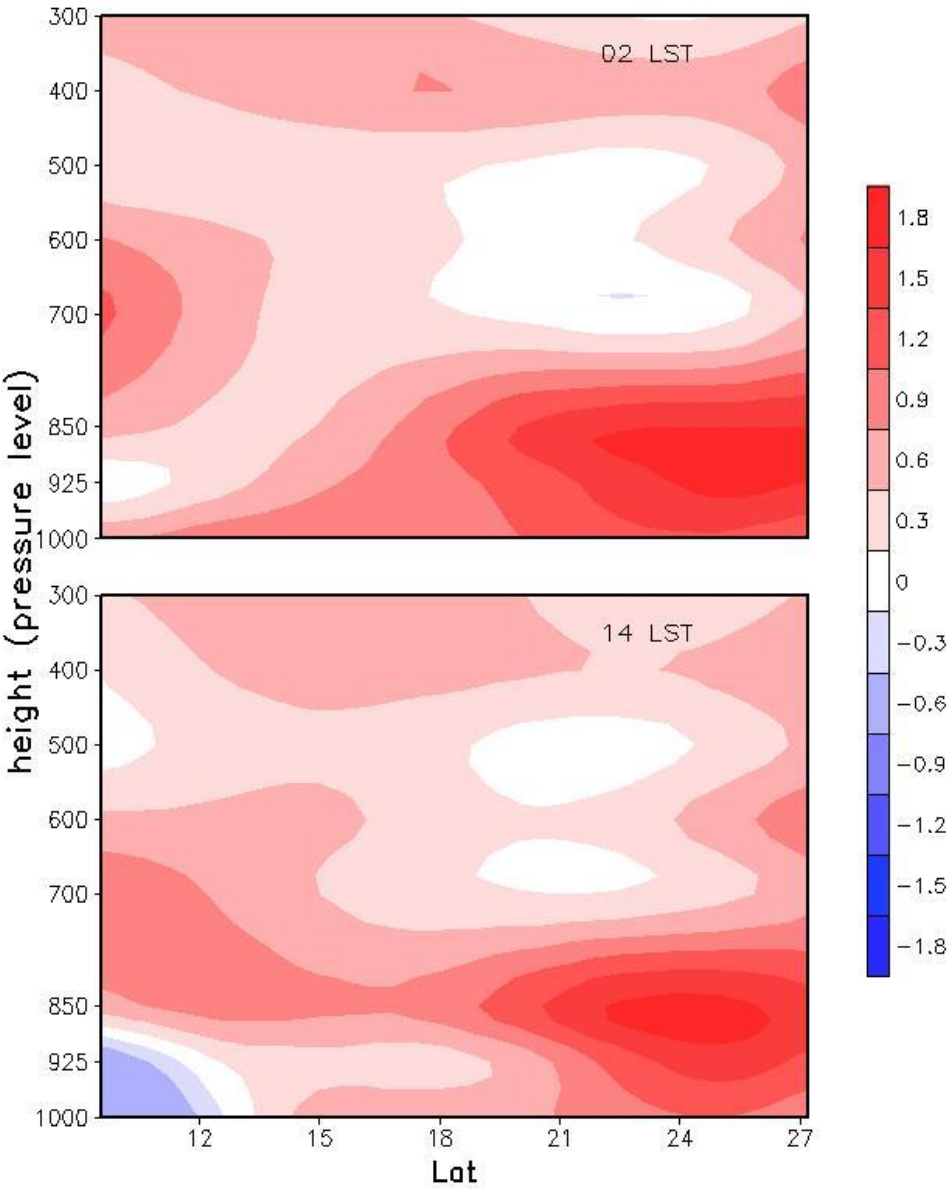

Figure 3.7: Vertical cross-sections of temperature differences (˚C) between the 1955-59 and 2000-04 timeframes thru the north-south line in Fig. 3.6 averaged at 02 (top) and 14 LST (bottom), the two closest times in the four-hourly data to the local overnight low and daytime high temperatures, respectively, during the Caribbean three-month ERS.

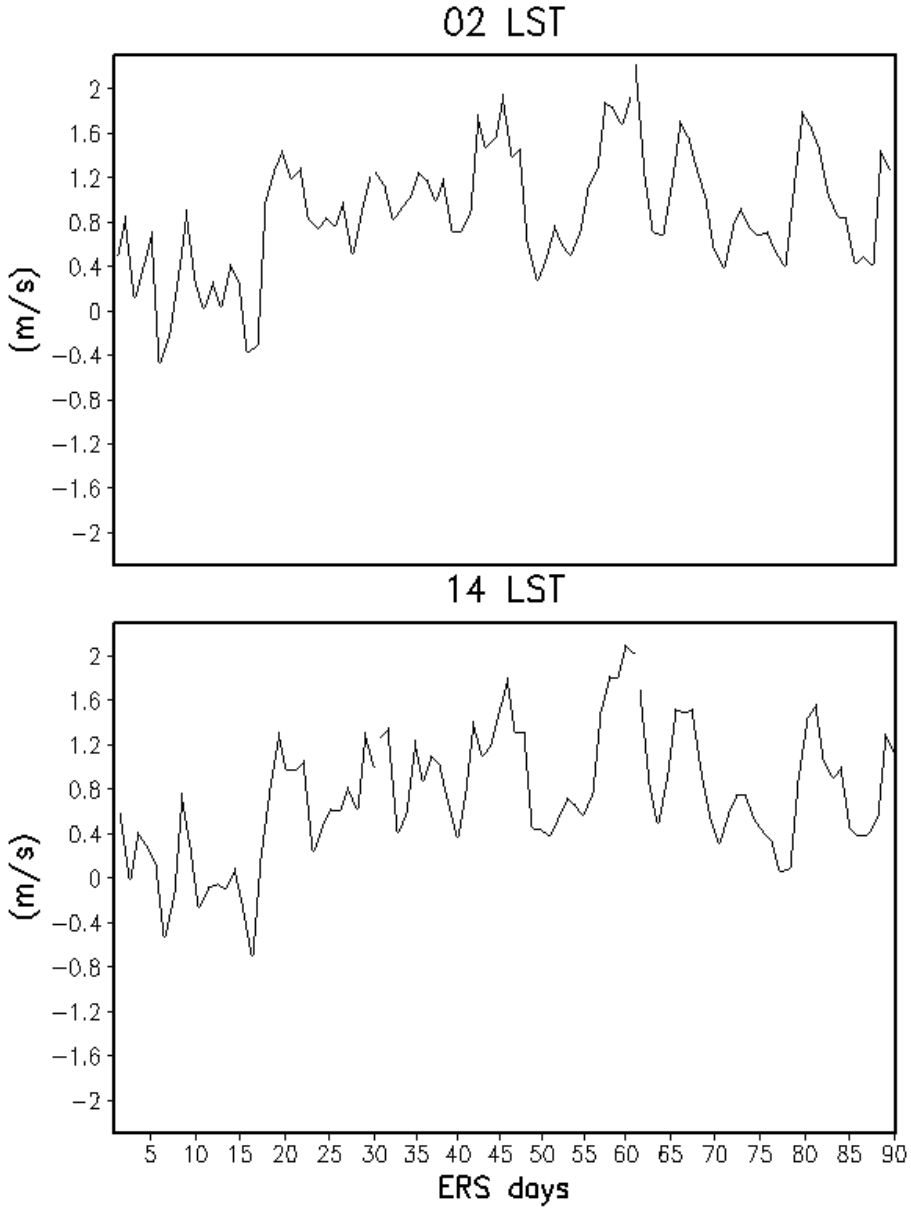

Figure 3.8: Large-scale basin-averaged horizontal wind magnitude (m s^{-1}) between the 1955-59 and 2000-04 timeframes and between pressure levels 1000 and 700mb, calculated from the NCEP Reanalysis 2.5˚ resolution data averaged at 02 (top) and 14 LST (bottom), the two closest times in the four-hourly data to the local overnight low and daytime high temperatures, respectively, during the Caribbean three-month ERS.

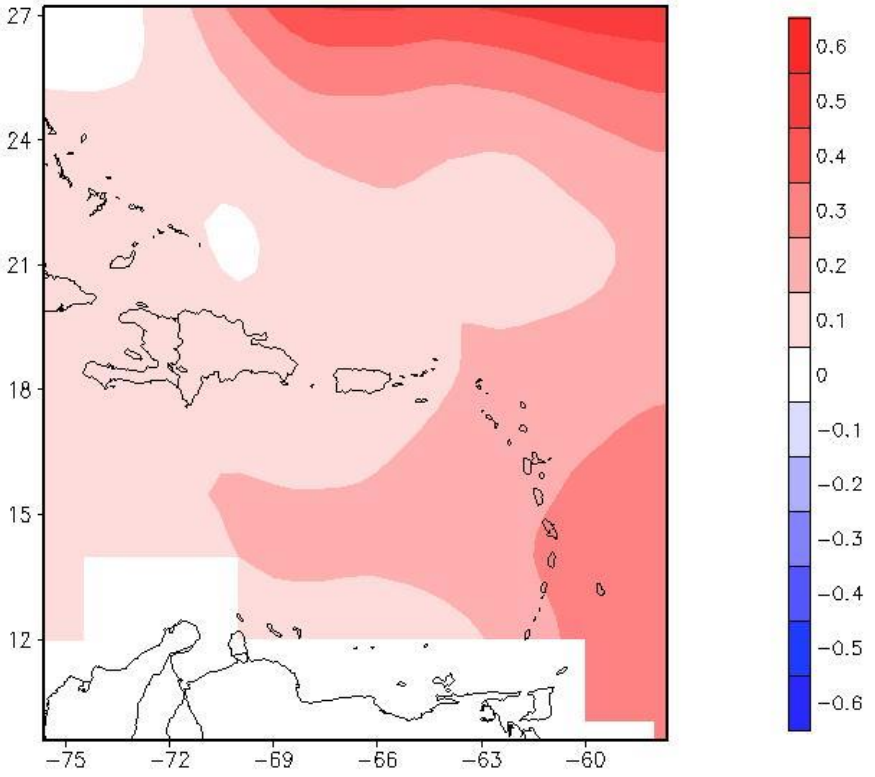

Figure 3.9: Large-scale sea surface temperature differences (˚C) between the 1955-59 and 2000-04 timeframes in Caribbean basin calculated from Smith and Reynolds ERSST dataset for month of April.

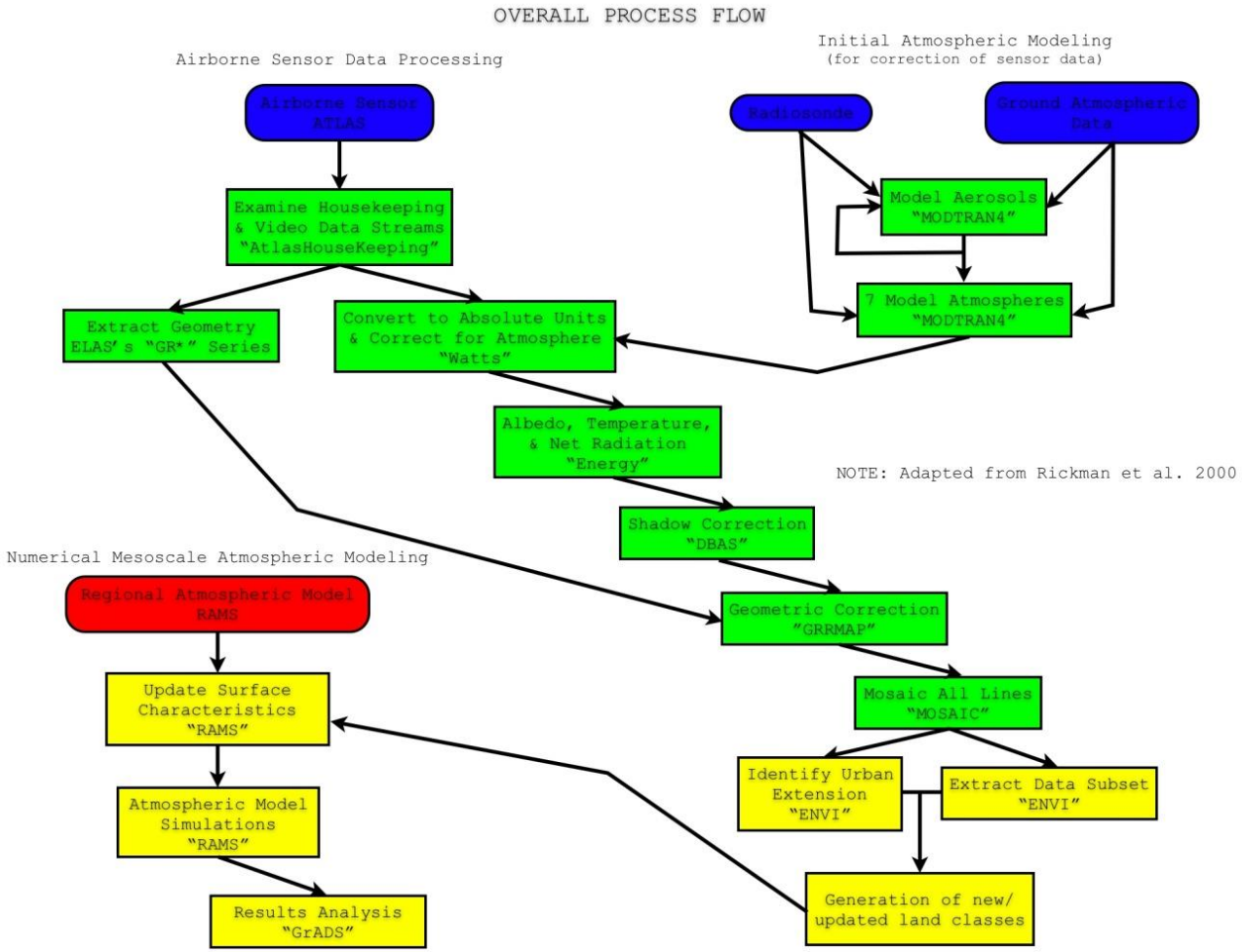

Figure 3.10: RAMS/ATLAS overall data processing flowchart to produce atmospheric, radiometric, and geometrically corrected data, and link to update the mesoscale model surface characteristics (adapted from Rickman et al., 2000).

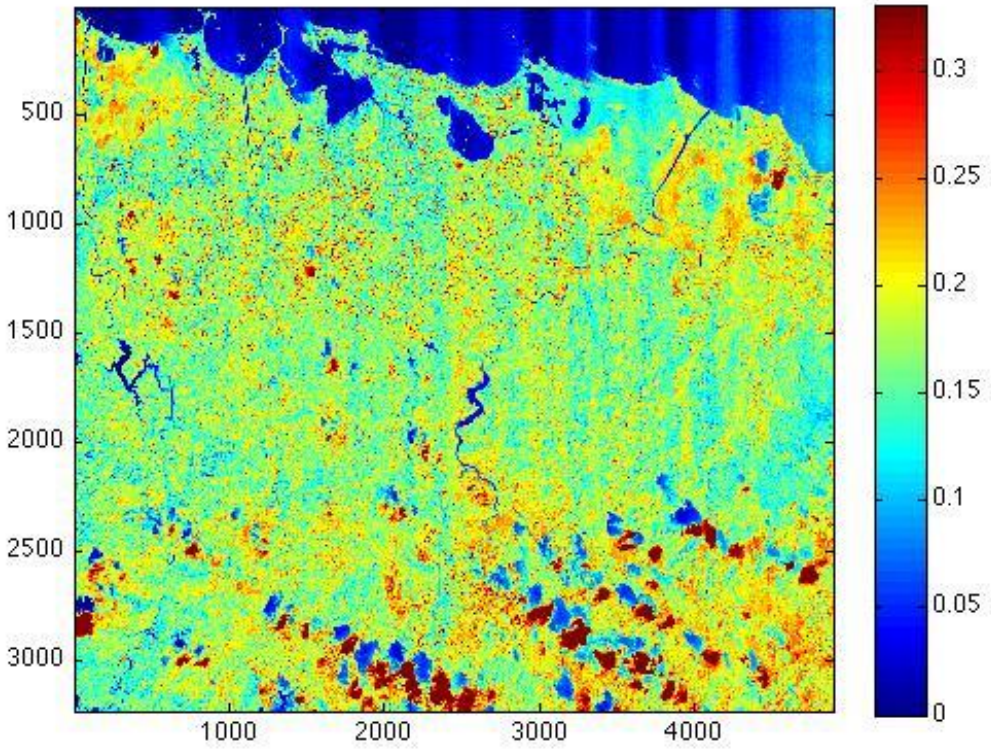

Figure 3.11: ATLAS-derived albedo dataset used to update the surface characteristics of the San Juan Metropolitan Area used in the regional atmospheric model configuration.

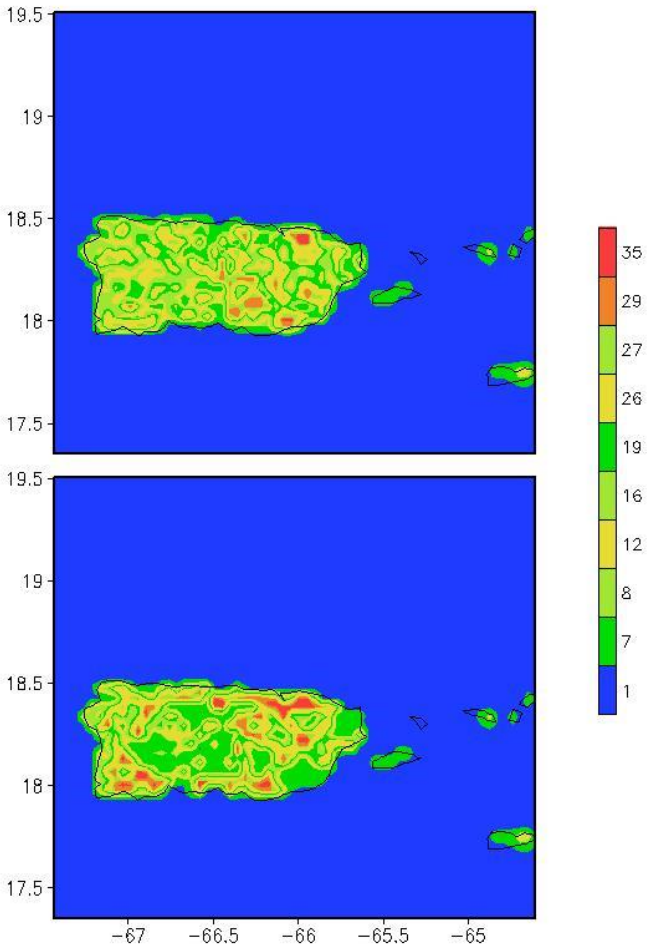

Figure 3.12: PAST (top panel) and PRESENT (bottom panel) surface characteristics specifications used in the two large-scale atmospheric condition scenarios described in Table 3.1 for Grid 2. Similar land classes were grouped together for visualization purposes (e.g., urban classes, forest classes, grassland with herbaceous agriculture). Appendix C contains a description of each class number and its corresponding biophysical parameters.

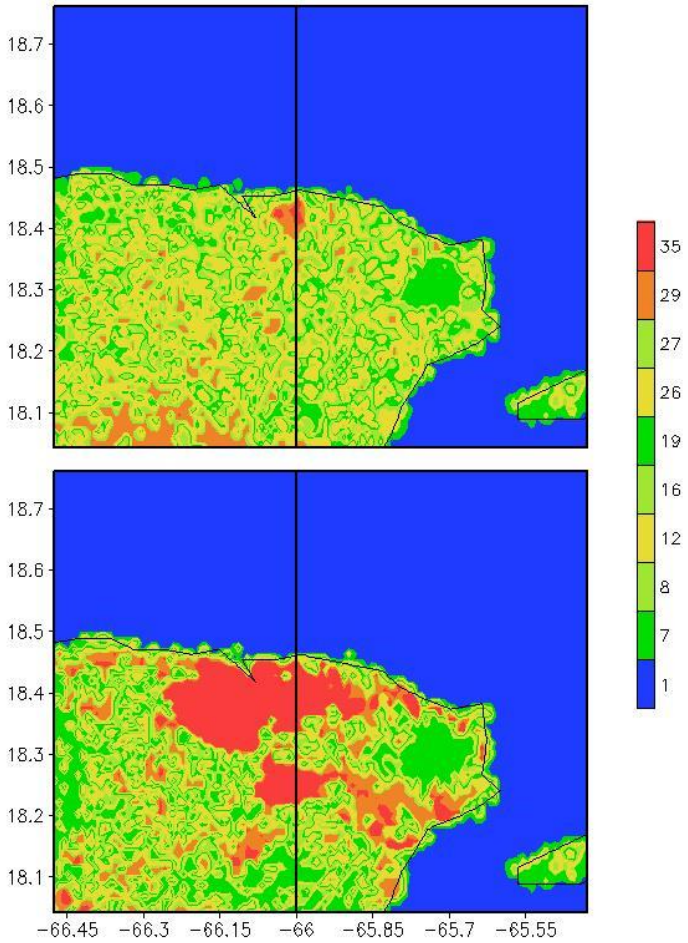

Figure 3.13: PAST (top panel) and PRESENT (bottom panel) surface characteristics specifications used in the two large-scale atmospheric condition scenarios described in Table 3.1 for Grid 3. Similar land classes were grouped together for visualization purposes (e.g., urban classes, forest classes, grassland with herbaceous agriculture). The thick solid vertical line in both panels represents the location of the north-south vertical cross-section presented in Chapter 5.

Chapter 4

Model Validation

A key element of studying the climate impact of LCLU changes and global warming in coastal tropical regions, or in any other geographical region, using a numerical atmospheric model as the main research tool, is producing accurate and reliable model results. The first step in the validation process is to prove that the incorporation of the ATLAS-derived information represents an improvement, not only in the representation of the urban areas as shown in the previous section, but in the results produced using such information to update the model's surface characteristics. Then, the climate results from the non-hypothetical simulations in Table 3.1 are compared and validated against observations from each of their corresponding time periods, given that reliable observations are available. These simulations are: PRESENT1, which consists of present LCLU specifications driven by present atmospheric conditions and PAST2, past LCLU driven by past atmospheric conditions.

The validation in Sections 4.3 and 4.4, as well as the climate impact analysis presented in the next Chapter, are performed using the five-year climatology for each model simulation and the observations. This procedure assures that the analysis is done to a climate dataset in which individual weather variations are averaged out and their influence reduced in the final result presented. The daily maximum and minimum temperatures presented in Figures 4.3-4.5 were obtained by averaging the corresponding temperature values predicted by the model over the entire area represented by the city and the forest at the time when the daytime highs and overnight lows were identified; they are then compared with the averaged values recorded by the COOP stations located within the same geographical area.

4.1 Cooperative Station Data

The observational data gathered and analyzed for this work is used primarily for comparison and assessment of the accuracy of the modeling results, but also to have an understanding of the historical climate pattern across the Caribbean island of Puerto Rico. The research makes use of the National Weather

Service cooperative station data, typically referred to as COOP stations, obtained from the Southeast Regional Climate Center and the Puerto Rico and U. S. Virgin Islands Climate Office. From a network of over approximately 70 stations that continually collected data for the island of Puerto Rico, 26 stations were selected. These stations were selected because they had the most complete record for the period encompassing the two timeframes chosen for the past and present climate conditions, and because their location covers the different climate zones that defined the Puerto Rico climatology (Malmgren and Winter, 1999). Figure 4.1 shows the locations of the 26 stations (see Tables 4.1 and 4.2 for details).

The station density for the island and area of study, 2.2×10^{-3} and 2.6×10^{-3} stations km^{-2} respectively, is below the World Meteorological Organization (WMO) standard for performing long-term climate studies in small mountainous islands with irregular precipitation (i.e., 3.3-7.1 $\times 10^{-3}$ stations km^{-2}, [WMO, 1981]). The sparce locations of the stations selected, and the incomplete record of many of the other stations, is one of the main reasons why a purely observational data analysis study was not performed, as also is the fact that any climate change reflected by the station data would represent the Total Change and the individual contributions of LCLU changes and global warming could not the quantified separately.

The daily maximum and minimum temperature values from the 26 stations were analyzed for the periods of interest. The most complete record was obtained for the stations in the SJMA for validation of the PRESENT1 and PAST2 climatologies generated using the model results and for comparison of the total changes. Temperatures in El Yunque could not be validated since data for the second half of the 1950s is not available for station located in that area. Precipitation was more difficult because there is no data available for the past period to use in the validation for stations at key locations, i.e., the SJMA and El Yunque. Alternatively, precipitation data for the stations within these areas was obtained for the period 1970-2006 (Table 4.2).

4.2 Atlas Mission Period

The model results produced by a 10-day run were compared with the observations obtained during the Atlas Mission experimental campaign conducted in Puerto Rico during the month of February 2004

(Gonzalez et al., 2005). These observational data consist of air temperatures at 2m above ground level as recorded by weather stations and temperature sensors.

The daily temperature cycle presented in Figure 4.2 was obtained by averaging the temperature values predicted by the model over the entire area represented by the city at each hour for the duration of the Atlas Mission, and is compared with the stations and ground sensors averaged over the same geographical area and time span (10-20 February 2004). This comparison shows that the model performs satisfactorily, even though it produced temperatures slightly higher than the observed ones during the late morning and early afternoon hours when surface heating is more intense. The improvement in the temperature prediction by using the five new urban categories is evident when compared to results obtained with a preliminary configuration using a homogeneous slab of concrete in the urban area, also shown in Figure 4.2.

The over prediction of this preliminary configuration could be explained by the use of a homogenous urban LCLU, which therefore is not capturing the different microclimates present in the metropolitan area and thus is producing a more uniform temperature distribution throughout the area. The reduction of daytime high temperatures in the simulations with more urban details might be due to a reduction of sensible heat flux and an increase in soil heat flux, or heat storage. Although the model is still has a tendency for over predicting temperatures from late morning to early afternoon, the results shows potential for further improvement by incorporating other in-situ and remote sensing measurements of physical parameters that are part of the Vegetation Index, like emissivity, surface roughness, leaf area index (LAI), vegetation fraction, among other surface characteristics, as well as other important parameters used in regional atmospheric modeling, like volumetric soil moisture content and soil textural class.

4.3 PRESENT1 Simulations

As mentioned before, the PRESENT1 simulation consists of present LCLU and present atmospheric conditions. Results from the PRESENT1 simulation for maximum and minimum temperatures were compared with observations obtained from the stations located in the SJMA (Figure 4.3) and El

Yunque (Figure 4.4). The comparison for the SJMA shows that the overall model performance is satisfactory, even though it produced higher maximum temperatures than the observed ones. The over prediction of maximum temperatures is evident, with the modeling-results time-series above the observations line and in the observations-results scatter plot, with the entire data points below the 45˚ line.

The comparisons for the minimum temperature results were much better. This prediction pattern of max and min temperatures is in agreement with the results obtained with the same atmospheric modeling methodology in the same geographical area presented in the previous sub-section, where the model showed a tendency for over predicting temperatures from late morning to early afternoon in short simulations during the Caribbean dry season (Comarazamy et al., 2010; Appendix E). The validation exercise for the PRESENT1 scenario in the SJMA proves that the methodology of running the atmospheric model with the five new urban categories generated using the ATLAS-derived albedo information is appropriate to conduct the climate impact study proposed in Chapter 3.

The validation procedure for El Yunque shows an accurate prediction of both maximum and minimum temperatures in that area. There is a section of the maximum temperature time series where the two datasets depart from each other. Near the end of May there is a marked increase in observed temperatures that does not carry over into June, when the atmospheric model predicts high maximum temperatures. This can also be seen in the horizontal spread of the observations-results scatter plot, even though the 45˚ line splits the data points approximately in half (Figure 4.4). The model prediction of minimum temperatures in El Yunque appears to be the most precise of the datasets compared with observations, with time series lines close to each other and data points around the 45˚ line in the scatter plot.

4.2 PAST2 Simulations

The validation of modeling results for the PAST2 simulation is of particular importance and interest. First, it is important to see how the model reacts to the ingestion of several reconstructed boundary conditions, namely the past LCLU specifications, generated from maps originally created in the 1950s, and

the extended reconstructed SST dataset, generated for the past timeframe from various sources. Second, it is of interest because no such exercise has been found in the literature for the region of study. Unfortunately there is no temperature data available for El Yunque for the 1955-59 timeframe (Table 4.2), hence only the model-reconstructed past climatology of maximum and minimum temperatures in the SJMA are validated (Figure 4.5).

Modeling results for the PAST2 climatology in the SJMA show higher predicted maximum temperatures than the observations, as seen in the time series plot; it also presents instances of higher variability, shown in the large horizontal spread in the scatter plot. Minimum temperatures, much as in the PRESENT1 case, are more accurate than the maximum temperatures, even though they are slightly hotter than the recorded values.

The over prediction of maximum temperatures over the area occupied by the SJMA during the climate simulations, as well as in the 10-day Atlas period validation results, could be an indication of the model mishandling the full effects of volumetric soil moisture content in vegetated areas within cities and of the effects of wet building materials (e.g., concrete, asphalt) on atmospheric surface heat fluxes. It has been thought for a long time that these materials are impervious and that their effect is primarily to increase sensible heat flux while drastically decreasing latent heat flux, but it has been recently reported, and starting to be widely accepted, that such materials as concrete and asphalt absorb and retain water after precipitation events (Ragab et al., 2003; Mansell and Rollet, 2006), and that the effects of wet building materials are not included in the surface exchange schemes of current releases of mesoscale atmospheric models (Lemonsu et al., 2007). Moreover, during the Atlas Mission in the SJMA, a small and short precipitation event (~4mm of rainfall) practically completely mitigated the UHI produced by the city. It was only a few days later, that the UHI reached the levels observed during the previous dry days, a pattern that was repeated after other similar events during the mission (González et al., 2006). Given all the results, it is concluded that the atmospheric mesoscale modeling methodology used in this work may not fully account for the effects of soil moisture in urban areas and wet building materials on surface and air temperatures, and that this should be addressed in future research.

In general, after the validation was performed and analyzed for the PRESENT1 and PAST2 climate results, and acknowledging that there are slight tendencies for over prediction of maximum temperatures, it is considered that the Regional Atmospheric Modeling System, complemented with digital LCLU maps, airborne remote sensing information, and reconstructed SSTs, and when driven with past and present atmospheric conditions, is an adequate tool to perform the proposed climate impact study due to LCLU changes in coastal tropical regions under conditions of global climate change.

Table 4.1: COOP Station Identification

Stn #	Station ID	Lat (deg min)	Lon (deg min)	Elev (m)
1	Isabela	18 28	67 10	128.05
2	Coloso	18 23	67 10	13.72
3	Mayagüez	18 11	67 08	30.49
4	Lajas	18 02	67 04	30.49
5	Magueyes	17 58	67 03	3.05
6	Maricao	18 09	66 59	862.80
7	Quebradillas	18 28	66 56	112.80
8	Adjuntas	18 10	66 48	524.39
9	Arecibo Observatory	18 21	66 45	–
10	Dos Bocas	18 20	66 40	60.98
11	Cerro Maravilla	18 10	66 34	1204.27
12	Ponce	18 02	66 32	12.20
13	Manati	18 26	66 28	83.32
14	Corozal	18 20	66 22	121.95
15	Dorado	18 28	66 19	12.20
16	Aibonito	18 08	66 15	640.24
17	Aguirre	17 57	66 13	15.24
18	Cayey	18 08	66 09	426.83
19	Guayama	17 59	66 05	54.88
20	Rio Piedras	18 23	66 03	15.24
21	Trujillo Alto	18 20	66 01	39.63
22	San Juan	18 26	66 00	21.34
23	Gurabo	18 16	65 59	76.22
24	Juncos	18 14	65 55	82.32
25	Canovanas	18 23	65 53	9.15
26	Pico del Este	18 16	65 45	1051.83

Table 4.2: COOP Station Variables and Period of Record for this Study

Stn #	Station ID	Max Temp	Min Temp	Precip.
1	Isabela	1950-2005	1950-2005	1908-2005
2	Coloso	1950-2006	1950-2006	1908-2006
3	Mayagüez	1950-2005	1950-2005	1908-2005
4	Lajas	1950-2006	1950-2006	1947-2006
5	Magueyes	1959-2005	1959-2005	1959-2005
6	Maricao	1969-2005	1969-2005	1969-2005
7	Quebradillas	1955-1975	1955-1975	1955-2000
8	Adjuntas	1970-2006	1970-2006	1970-2006
9	Arecibo Observatory	1980-2006	1980-2006	1980-2006
10	Dos Bocas	1950-2005	1950-2005	1937-2005
11	Cerro Maravilla	1969-2005	1969-2005	1969-2005
12	Ponce	1954-2005	1954-2005	1954-2005
13	Manati	1955-2005	1955-2005	1908-2005
14	Corozal	1950-2006	1950-2006	1931-2006
15	Dorado	1950-2005	1950-2005	1931-2005
16	Aibonito	1950-2006*	1950-2006*	1908-2006*
17	Aguirre	1970-2005	1970-2005	1955-2005
18	Cayey	1955-2001	1955-2001	1955-2001
19	Guayama	1950-2006	1950-2006	1911-2006
20	Rio Piedras	1955-2006	1955-2006	1959-2006
21	Trujillo Alto	1956-2006	1956-2006	1969-2006
22	San Juan	1956-2006	1956-2006	1959-2006
23	Gurabo	1956-2006	1956-2006	1956-2006
24	Juncos	1950-2006	1950-2006	1931-2006
25	Canovanas	1955-1968	1955-1968	1955-2005
26	Pico del Este	1970-2006	1970-2006	1970-2006

* No data from 1977 to 1993

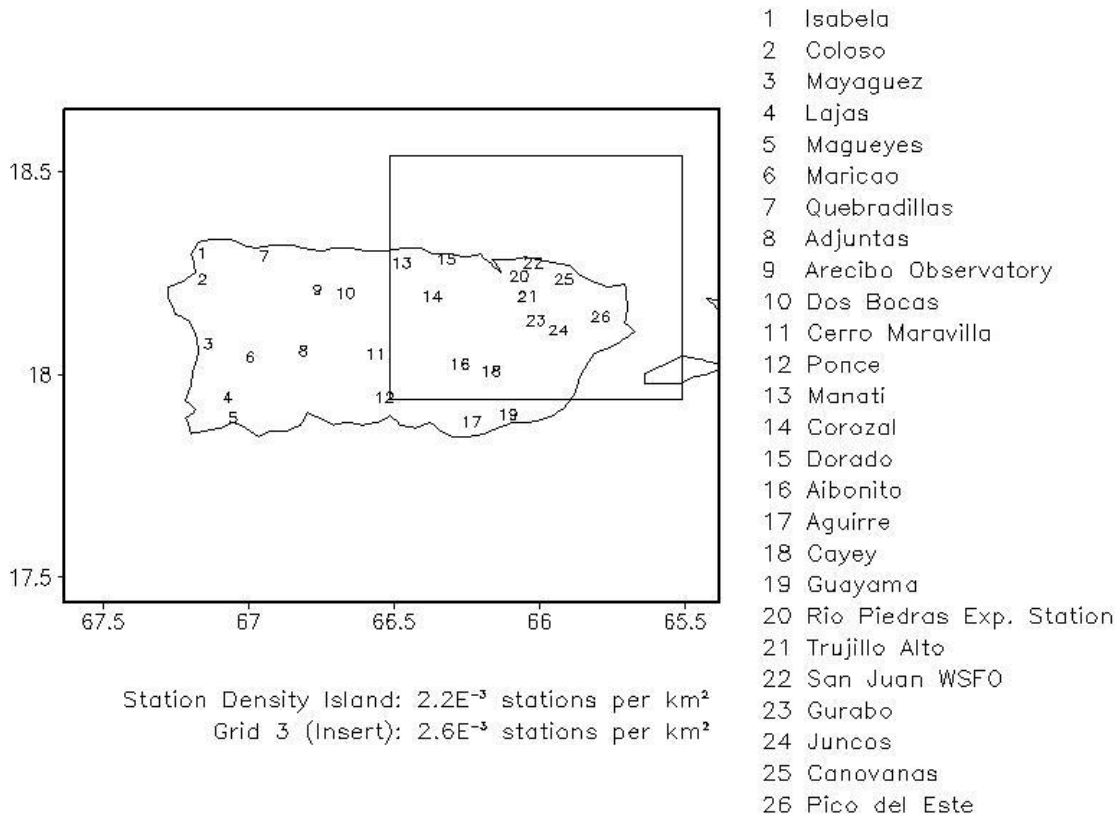

Figure 4.1: Location of the 26 COOP surface weather stations selected for this study. Box insert indicates the location of modeling Grid 3.

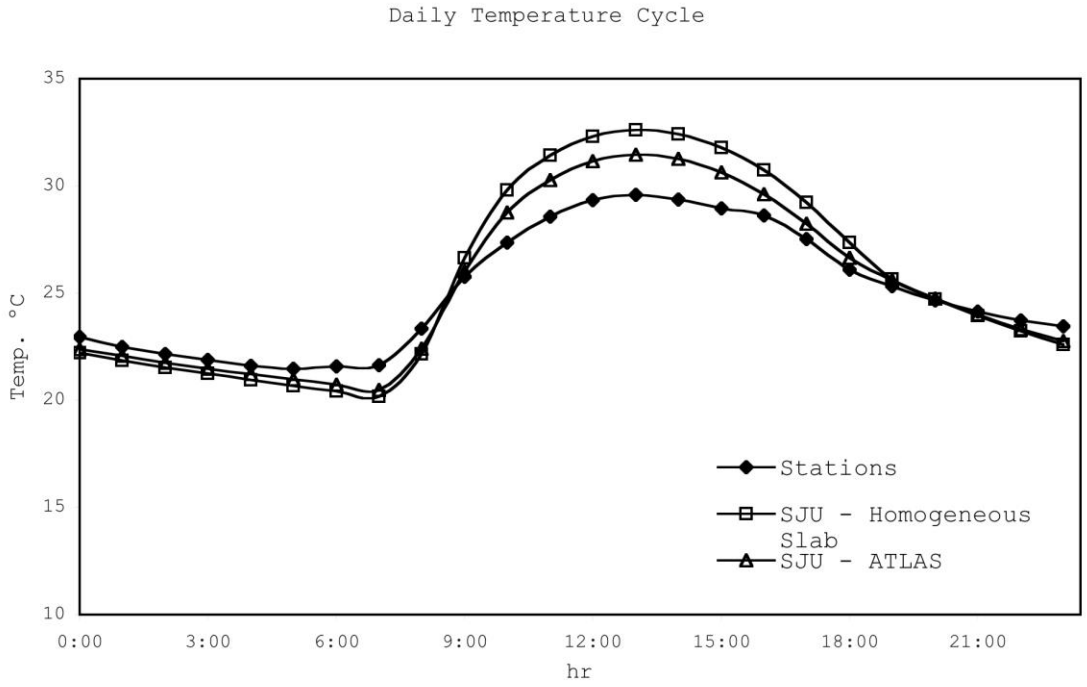

Figure 4.2 Comparison of the air temperatures from the regional model results and the stations and sensors deployed in the San Juan Metropolitan Area (SJU in the legend).

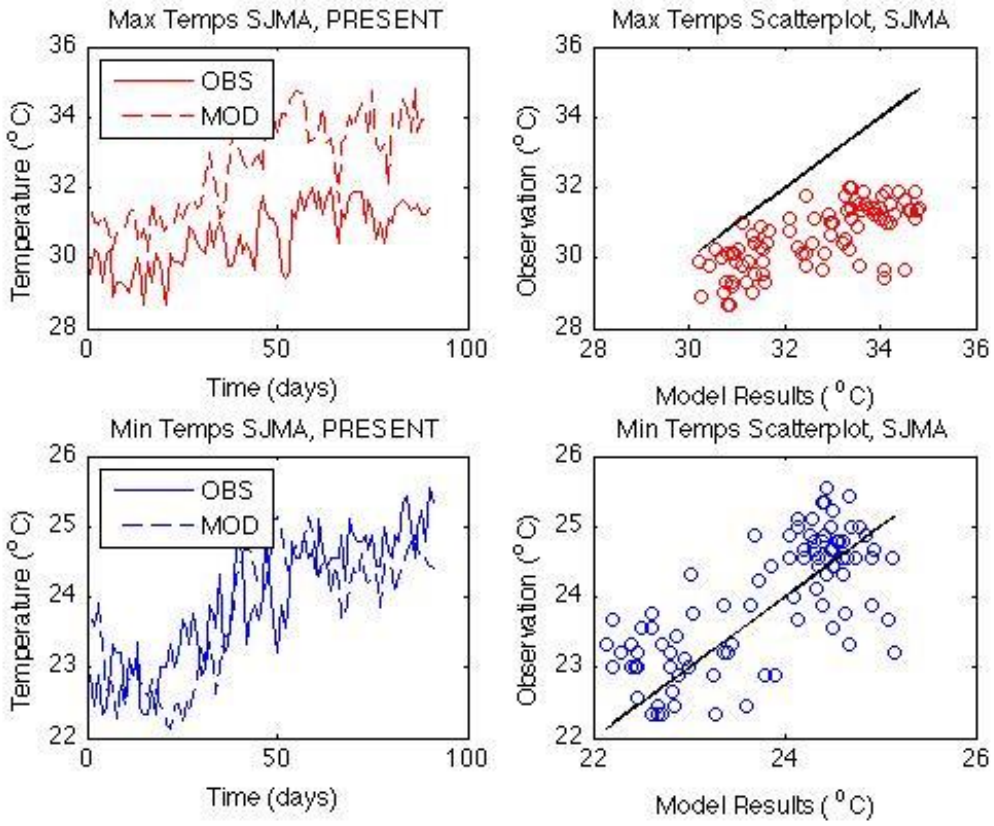

Figure 4.3: Time series of modeled and observed maximum and minimum temperatures (top left and bottom left, respectively) and observation-model scatter plots of maximum and minimum temperatures (top right and bottom right, respectively) for the PRESENT1 climatology in the SJMA.

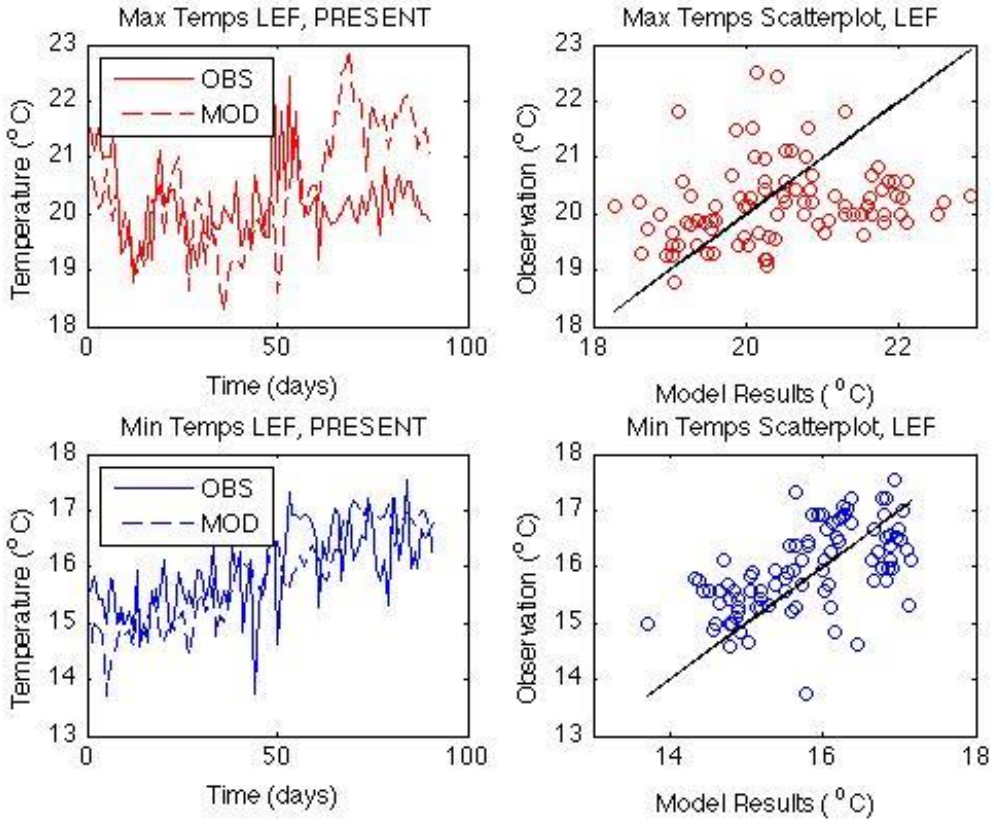

Figure 4.4: Time series of modeled and observed maximum and minimum temperatures (top left and bottom left, respectively) and observation-model scatter plots of maximum and minimum temperatures (top right and bottom right, respectively) for the PRESENT1 climatology in El Yunque.

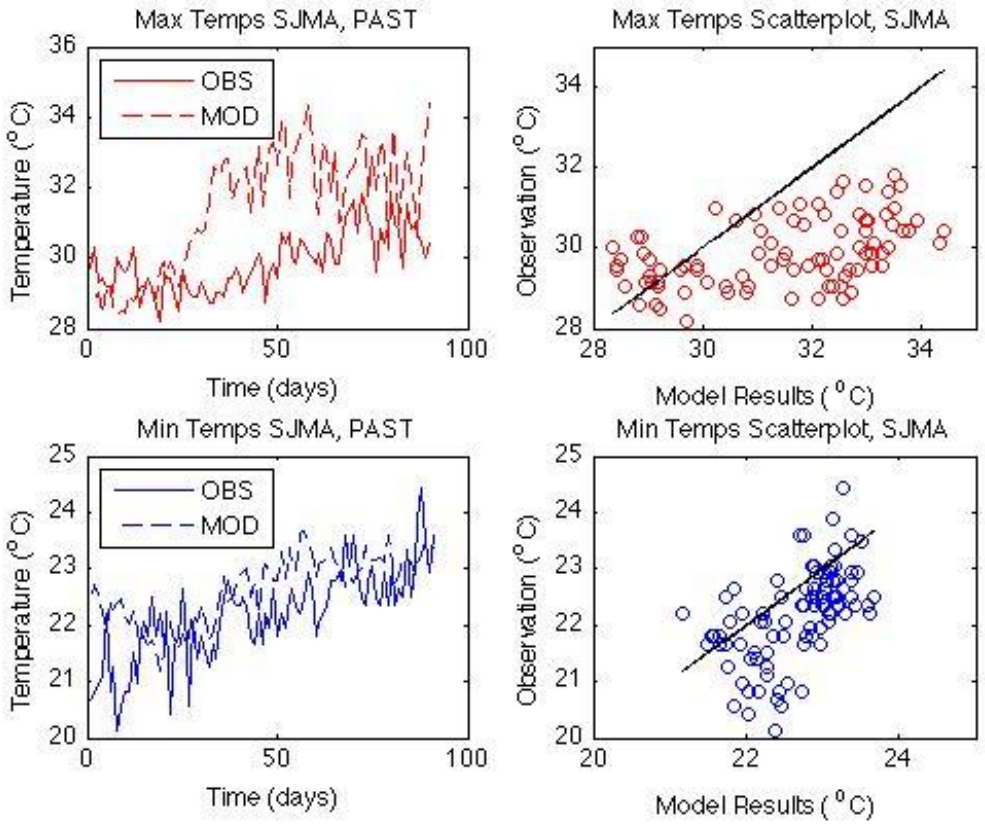

Figure 4.5: Time series of modeled and observed maximum and minimum temperatures (top left and bottom left, respectively) and observation-model scatter plots of maximum and minimum temperatures (top right and bottom right, respectively) for the PAST2 climatology in the SJMA.

Chapter 5

Climate Impacts of LCLU Changes in Coastal Tropical Regions Under Conditions of Global Climate Change

To study the impact of land cover and land use (LCLU) changes and of global warming in coastal tropical regions, the northeastern region of the Caribbean island of Puerto Rico was taken as the test case. Climate impacts, mainly on air temperature and accumulated precipitation, are analyzed by calculating the difference between the possible combinations of simulations in Table 3.1 that have a physical meaning. These combinations explain the climate impacts due to LCLU changes under present atmospheric conditions (PRESENT1 – PAST1), due to LCLU changes under past conditions (PRESENT2 – PAST2), due to global warming with present LCLU (PRESENT1 – PRESENT2), due to global warming with past LCLU (PAST1 – PAST2), and what is determined to be Total Change due to LCLU changes and global warming (PRESENT1 – PAST2). Table 5.1 summarizes these different combinations, what aspect of the climate impact analyzed they explain, and which panel in Figures 5.1-5.10 shows each effect.

Also incorporated into the analysis is the factor separation method of Stein and Alpert (1993), which calculates the individual contribution of the two factors in question, determined to be two of the calculations presented above and the contribution to the Total Change due to the non-linear interaction between the two factors. Appendix D contains a detailed description of the factor separation method and formulation, along with other statistical techniques applied to the model results to determine the statistical significance of the difference in means calculated. As with the validation, the results presented in the next sections refer to the five-year climatology of each of the simulation scenarios described in Table 3.1.

5.1 Impacts on Temperature

Since the most noticeable indicator of climate change, at any scale, is changes in temperature, near surface (2m above ground level [AGL]) differences are analyzed for mean daily minimum and maximum temperatures over land areas in Grid 3, which has results at 1km horizontal resolution (Figures 5.1and 5.2,

respectively). Results for minimum temperature change (Figure 5.1), show positive differences for the Total Change, panel c (upper right) that range from 1 to 2˚C throughout the domain, with minimum temperature differences peaking around 2.4˚C. Panel a (upper left) shows the mean daily minimum temperature difference due to the land cover and land use change between the two periods in study, while driving the model with the present atmospheric conditions and SSTs. Panel b (center top) shows the same LCLU signal, but driving the model with the 1955-1959 atmospheric and SST conditions. The statistical significance test reveals that minimum temperature differences over land areas for the two LCLU change cases are significant, at $\alpha_{LS} = 0.05$ (see Appendix D), over the major urban regions, which are identified by the thick black contour, though the full horizontal distribution does not clearly indicate an urban influence in the temperature differences. Differences are also significant in pockets of increased temperature differences. The global warming signal using the present LCLU surface characteristics, panel d) (lower left), shows that results are significant over a larger portion of the domain, with the exception of small areas in elevated terrain, specifically along the Central Mountain ridge and El Yunque, the two regions identified by the thick green contour. Panel e) (center bottom) also shows the global warming signal in the mean daily minimum temperature differences, but using the past LCLU specifications as surface characteristics. Panels d) and e) show the same domain-wide heating trend of 0.8-1.6˚C, with increased heating of ~1.6˚C along the northeastern and southeastern coastlines and at interior lowlands.

The fact that the panels a) and b), and d) and e), in Figure 5.1 are strikingly similar indicates that the impact of LCLU changes on minimum temperatures during the period analyzed is relatively independent of the large-scale climate conditions, and vice versa. The difference between the temperature change shown in panels a) and b), which yields the same results as the calculation of the difference between panels d) and e), is shown in panel f) (lower right), where small temperature differences and no statistical significance exist throughout the domain. This indicates that the sum of the individual effects is not significantly different from the combined linear effect of both (Stein and Alpert, 1993). This shows that for the late 20th century changes in minimum temperatures, the differences induced by LCLU changes and those due to large-scale climate change are independent, being able then to be combined linearly to obtain the Total Change distribution (panel c, upper right).

The results for mean daily maximum temperature change are shown in Figure 5.2. Temperature differences due to LCLU changes, while driving the model with present atmospheric conditions and SSTs, panel a) (upper left), clearly show the influence of the urban areas, including the SJMA, Caguas, and the ring of ongoing development around El Yunque, on the early afternoon daytime high temperature change. These urban areas, identified by the thick black contour in the panels of Figure 5.2, show statistically significant (at $\alpha_{LS} = 0.05$) positive temperature increases that range between 2 and 5˚C. The rest of the domain shows temperature increases over land regions between 0.8 and 2.4˚C in sparse locations where LCLU conversions less dramatic than urbanization have occurred from 1951 to 2000 (see Figures 1.4 and 3.13). Results for the temperature differences due to LCLU changes, while driving the model with the 1955-59 atmospheric and oceanic conditions, present the same pattern of maximum temperature change, panel b) (center top). These results show that the strong SJMA urban heat island (UHI) has a significant influence in near surface air temperatures and that this influence has been increasing with time, conclusions that are in agreement with previous studies of the effects of the SJMA UHI (Velazquez-Lozada et al., 2006; González et al., 2006).

Panel d) (lower left in Figure 5.2) shows the maximum temperature differences due to global warming while keeping the present LCLU specification constant. These results present a more homogeneous pattern of significant temperature changes over land regions than the two LCLU cases. The pattern shows a temperature difference gradient increasing inland from the coast to near the Central Mountain ridge; high elevation terrain is identified by the thick green contour in Figure 5.2. Of interest to the topic of the climate impacts in coastal tropical regions is the slight cooling observed along the easternmost coastline of Puerto Rico, 0 to 0.8˚C, due to the global warming signal, which could be attributed to an increase in surface trade winds that are orthogonal to the coastline in the eastern to southeastern region of the island, as will be shown in Section 5.2. Panel e) (center bottom) also represents the global warming signal in the maximum temperature differences, but using the past LCLU specifications as surface characteristics; it shows the same temperature increase pattern as panel d). The coastal cooling in the global warming signal, panels d) and e), might help mitigate or hamper the heating occurring along the

same coastline due to ongoing urbanization observed in the LCLU change panels a) and b). This is of extreme importance in the northeastern part of the domain, where residential and tourism projects account for much of the development around the El Yunque area, a natural reserve protected by law. Maximum temperature changes in the entire coastline of the northeastern region of Puerto Rico, with the exception of the section of coast corresponding to the SJMA, were not shown to be significant, at $\alpha_{LS} = 0.05$ and at $\alpha_{LS} = 0.1$, possibly due to the low values found in the differences in mean daily maximum temperatures for the areas in question.

As with the minimum temperature change shown in Figure 5.1, panels a) and b), and panels d) and e), in Figure 5.2 show almost exactly the same maximum temperature change pattern, indicating that the impact due to LCLU changes during the ~50-year period between 1951 and 2000 is relatively independent of the large-scale climate conditions of the five-year periods of 1955-59 and 2000-04, and vice versa. This is evident in the low temperature values with low significance shown in panel f) (lower right), which is constructed by taking the difference between the maximum temperature change shown in panels a) and b), or between panels d) and e). This indicates that the changes in maximum temperatures due to LCLU changes and those due to global warming are independent of each other, and therefore can be added linearly to obtain the Total Change distribution (panel c, upper right). Regarding the small coastal cooling discussed before in the global climate change signal (panels d and e) as being able to mitigate the temperature increases in coastal urban regions observed in the LCLU change signal (panels a and b), the Total Change in panel c) (upper right) shows that the impact due to LCLU changes still dominates the overall maximum temperature change pattern in the region of interest, especially where there is more urbanization with little coastal cooling effect. In general, the horizontal heating pattern produced by the global warming signal, especially in the interior of the domain, has an enhancing effect to the maximum temperature changes produced by the LCLU change signal.

To observe the impact that LCLU changes and global climate change have on the boundary layer (BL), vertical cross section plots are constructed in the north south solid black line seen in Figures 3.1 and 3.13 and which cuts thru the SJMA, Caguas, and the Central Mountains. The vertical cross sections

presented in Figures 5.3 and 5.4 show temperature differences (shaded contours), vertical wind differences (wind vectors), and atmospheric liquid water mixing ratio (black contours) at the time of minimum and maximum temperature, respectively; the underlying topography in all panels is represented by the green shade. For minimum temperature (Figure 5.3), differences due to LCLU changes with present atmospheric conditions and SSTs, panel a), are limited to near the surface in the region occupied by the SJMA (centered around 18.4 north latitude) and are almost non-existent at higher vertical levels. Panel b) shows the LCLU change signal driving the model with past atmospheric and SST conditions, as with panel a) the changes in temperature are present only near the surface where the city is located, with no changes in the upper levels in temperature, vertical motion, and liquid water content. The global warming signal with present LCLU (panel d) produces positive temperature changes from the surface up to 900m, a band of no changes with a nucleus of small negative values (cooling) from 900 to 2100m, and then with increased heating in the higher elevations. This pattern of minimum temperature changes in the vertical cross sections might be explained as the influence of the input NCEP data that shows a similar behavior in the vertical levels (Figure 3.7). Given the similarity between panels a) and b), and between d) and e), the LCLU change signal and the global climate change signal combine to produce the vertical Total Change pattern shown in panel c), which in turn is similar to the global climate change signal (panels d and e), with the added surface heating over the city produced by the LCLU signal (panels a and b).

As with the horizontal distribution of temperature changes, there is more complexity in the vertical cross section plots at the time of maximum temperature (Figure 5.4) than in the plots at the time of minimum temperature. Even though there are noticeable differences in the vertical motion and liquid water fields due to LCLU changes (panels a and b), changes in temperature are still limited to near the surface, penetrating a little further into the atmosphere than in the minimum temperature LCLU cases, especially the maximum temperature difference due to LCLU change, while driving the model with past atmospheric conditions (panel b). The Total Change of maximum temperature differences (panel c) resembles closely the results of differences due to the global warming signal, whether with present or past LCLU, panels d) and e), respectively; this is a consequence of the low differences found in the LCLU change signal results and of the similarity between panels a) and b) and between panels d) and e). Maximum temperature

differences in the Total Change and global warming signal panels c), d), and e), respectively, penetrate up to 1500m, driven by the vertical motion generated by a convergence zone located north of the Central Mountains (see also Figures 5.5 and 5.6). The circulation generates a cell with subsidence in the mountain range ridge, the location of the convergence zone in the simulations driven by past atmospheric conditions. In all panels the green shaded area identifies the underlying topography. There is also a band of no temperature changes from 1500 to about 3000m, where the main liquid water differences layer are located in panels c), d), and e). For further discussion on the differences in wind convergence zone and atmospheric liquid water content, see Section 5.2.

To study the evolution of temperature differences and surface wind (at 15m AGL) differences during an averaged day, the four-hourly results for the Total Change scenario are analyzed (Figure 5.5). The wind vector difference was calculated by taking the difference between the horizontal wind components, u and v, and constructing the vectors with the resulting components. Figure 5.5 shows the evolution from calm conditions at midnight local standard time (LST), 00LST (panel a, upper left), when low temperature differences and virtually no change in the wind vector field prevail, to the small temperature differences observed at the time when minimum temperatures occur at 04LST in panel b) (center top), compared to panel c) (upper right) in Figure 5.1. At 08LST (panel c, upper right), temperature differences start to increase in the urban areas, identified by the thick black contours in all panels, and the winds in the present climatology begin to increase and take a more easterly direction, reflecting values of up to 7 m s^{-1}, which is on average 2 m s^{-1} faster than winds in the past climatology.

The 12LST panel (panel d, lower left) shows the maximum temperature difference (compare to panel c) in Figure 5.2) and the shift of the convergence axis from the top of the Central Mountain ridge northward to a lower elevation location, as indicated by the wind difference vectors in the direction of the coast from the mountains (identified by the thick green contour) and the relative no change along he northern coastal plain. This setting of increased air temperature, with emphasis on the urban areas, and shift of the mentioned convergence zone, is still present four hours later at 16LST (panel e, center bottom). At 20LST, panel f) (lower right), temperature differences are at their lowest, and the wind vectors have

approximately the same magnitudes (~5 m s^{-1}), but are changed to a slightly northeasterly direction in the present climatology. Regarding the small coastal cooling shown for the southeastern coast in the global warming influence on maximum temperature differences (panels d) and e) in Figure 5.2), in Figure 5.5 it can be seen that there are positive temperature differences in that area during the night hours (panels f, a, and b). This increase starts to diminish when the winds start to increase (panel b), before eventually reaching their lowest values during the highest heating times (panels d and e). Nevertheless, it is also seen that the areas of higher urbanization around El Yunque, identified by the black contours around the easternmost thick green contour, remain with an increasing temperature difference trend throughout the day for the Total Change scenario (PRESENT1-PAST2).

The reported changes in the wind direction and magnitudes could be due to a combination of the changes in SSTs (Figure 3.9) and the differential heating occurring over land (Figures 5.1-5.4). These changes in direction and speed could be producing a more penetrating flow inland from the southeastern coast and therefore driving the convergence zone that climatologically produces precipitation in the Central Mountains northward. In Section 5.2 the effects these results have on cloud formation and accumulated precipitation are expanded.

5.2 Impacts on Surface Accumulated Precipitation

The influence of topography in the precipitation pattern in the island of Puerto Rico is well documented (Daly et al., 2003; Comarazamy and González, 2008; Jury et al., 2009). Precipitation climatologically occurs when the easterly trade wind transport available moisture from ocean evaporation up the mountain slopes, which acts as a lifting mechanism, forming a convergence zone atop the mountain ridge. This in turn leads to cloud formation, rain development, and consequently surface accumulated precipitation (Comarazamy and González, 2008). Any disruption to the wind pattern that sets the mechanism in motion is likely to have a profound effect in the precipitation pattern, or at least in the amounts of precipitation and fresh water available at the surface.

Figure 5.5 shows how that wind pattern has changed from the PAST2 simulations, which consist of past LCLU specifications with past atmospheric conditions and SSTs, to the PRESENT1 simulations, i.e., present LCLU with present atmospheric and SST conditions; this has been referred to as the Total Change. To better visualize the difference in wind patterns, and to easily identify the axis of convergence produced by the past and present simulated climatologies, Figure 5.6 shows the daily evolution of the two wind vector fields without taking the difference in horizontal wind components. In Figure 5.6 it is seen how the two vector fields have similar magnitude and that they follow a similar direction pattern from midnight to the early morning hours, from 00 to 08LST (panels a, b, and c). At 12LST, panel d). This is evident from the position of the convergence zone along the central mountains in the past climatology (red vectors in Figure 5.6) and along the northern region just off the foothills of the mountain range in the present climatology (black vectors in Figure 5.6). This pattern is still in full effect at 16LST, panel e). The convergence in the present climatology is at its strongest point at 12 and 16LST (panels d and e, respectively) in the narrow valley where Caguas is located, identified by the thick black contour south of the SJMA, between the Central Mountains and El Yunque, identified by the two thick green contours in all panels. This strong convergence zone localized in such a narrow geographical area could be due to the downwind low-pressure generated by a free flow around an obstacle, in this case El Yunque; during the past climatology, the flow is slower and approaches the coastline at a different angle.

The convergence zone in the PRESENT1 simulations generates vertical motions that increase the liquid water mixing ratio, and the subsidence that the circulation cells generate on the mountaintops reduces the liquid water content in the atmosphere above the ridge (Figure 5.4, panel c). The liquid water mixing ratio ($g\ kg^{-1}$) contains the amount, in total mass, of cloud droplets and raindrops per kilogram of dry air, and therefore accounts for the two completely non-frozen cloud microphysics hydrometeors in the atmospheric regional model cloud module that indicate the cloud formation and rain development process in the tropics. It has been reported that changes in wind patterns and vertical wind motions should also produce changes in cloud base heights, an important parameter in tropical montane cloud forests (Hamilton et al., 1993; Bruijnzeel and Proctor, 1993; Lawton et al., 2001; Nair et al., 2003; Ray et al., 2006). A montane cloud forest is defined as a tropical or subtropical moist forest in elevated terrain in which the

cloud base is persistently or seasonally at or below the vegetation canopy level. The cloud base height, in turn, is defined as the lowest atmospheric level at which the air contains perceptible amounts of cloud particles. In this sense, the liquid water mixing ratio is the ideal model produced variable to analyze these parameters.

The cloud base height is determined by identifying the first level in the model vertical coordinate, from the surface up, where measurable amounts of liquid water (i.e., 0.005 g kg^{-1}) are present, and then the climate impact calculations are performed and presented in Figure 5.7. Panel a) (upper left) shows that there are no significant changes in cloud base heights due to LCLU changes when driving the model with present climate conditions. In panel b) (center top), where the cloud base heights change due to LCLU changes, but the model is driven with the past atmospheric and SST conditions, it is shown that over land regions, cloud bases have increased an average of 500m. These results, however, might be masked by trace amounts of liquid water mixing ratio at high atmospheric levels in the simulation driven by past LCLU specifications and climate conditions, the PAST2 simulation, and by the fact that differences due to LCLU changes are not expected to occur over ocean regions. For the global warming signal, while keeping the LCLU constant to the present characteristics (panel d, lower left), cloud bases are higher within land regions, while showing large negative values over the ocean, a pattern repeated by the global warming signal with past LCLU as surface characteristics (panel e, center bottom). The results for the non-linear interaction between the two factors (panel f, lower right) show that the contribution of global climate change to the LCLU signal (panel a minus panel b) is higher cloud bases over the ocean surrounding the island. Panel f) is also equivalent to the contribution of LCLU changes to the global warming signal (panel d minus panel e), but while as mentioned before, no significant changes are expected over ocean regions due to LCLU, it is worth noting that SST conditions remain constant in the results presented in panels a) and b). The results, pattern, and values, presented in panels b), c), d), e), and f) of Figure 5.7 might be misleading since trace amounts of liquid water at high atmospheric levels in the simulations driven by the past climatology is producing the large cloud base height difference values (±2500m) observed over ocean regions surrounding the island. Therefore, a more demanding liquid water mixing ratio threshold (0.01 g kg^{-1}) was specified in the algorithm to calculate the cloud base heights.

The impact analysis for the re-calculated cloud base heights is shown in Figure 5.8. Panel a) shows the results for cloud base height difference due to LCLU change, while driving the model with present atmospheric and SST conditions, panel b) also shows the LCLU signal but by driving the model with the past climate conditions. Although the two LCLU signal cases did not produce a pattern of cloud base height difference that clearly follows the regions of larger LCLU changes, the case with past climate (panel b) shows large increases in cloud bases along the north coast, less so along the Central Mountains, and decrease heights along the eastern and southeastern coast. For the cases that represent the impact due to global climate change, both with present and past LCLU specifications (panels d and e, respectively), cloud base heights appear higher at 500, 1000, and 1500m over the higher elevations of the Central Mountains, and by an average of 500m over El Yunque, while decreasing along the coastal plains. A pattern reproduced almost exactly for the Total Change (panel c, upper right). For the case of cloud base height differences presented in Figure 5.8, panels a) and b) show different patterns, indicating that cloud base height differences due to LCLU changes are not independent of the large-scale climate conditions and that their difference, the non-linear interaction between the two factors (panel f), cancels the LCLU signal along the coast from the Total Change. This produces a Total Change pattern (panel c) that closely resembles the global climate change signal in panels d) and e).

The decreasing cloud base heights over low land coastal plains might be due to the slight coastal cooling observed in the easternmost region of the island (see Figure 5.2). These results are in agreement with the increases in cloud base heights observed over the Monteverde region of Costa Rica due to localized deforestation (Lawton et al., 2001; Nair et al., 2003; Ray et al., 2006), although these previous studies did not include the effects of global climate change in the configuration of their modeling experiments and conclusions.

To complement the cloud base heights information, the total column liquid water content (g kg^{-1}) was also analyzed. This gives an indication of how thick or dense the cloud is, and is independent of where in the column the liquid water appears, effectively eliminating some of the problems encountered in the

cloud base height differences. Results for total column liquid water content change, Figure 5.9, show that there is little impact on the differences observed due to LCLU changes when driving the model with present climate conditions, panel a) (upper left), and due to LCLU changes under past atmospheric and SST conditions, panel b) (center top). The impact on total liquid water content are mainly due to the global warming signal, whether with present or past LCLU, panels d) (lower left) and e) (center bottom), respectively, and this is reflected on the Total Change pattern. Results for the Total Change in total atmospheric column liquid water content in panel c) (upper right) of Figure 5.9 shows that liquid water decreases in high amounts all along the Central Mountains (-0.03 to -0.15 g kg^{-1}) and in the El Yunque area and close surroundings (-0.03 to -0.12 g kg^{-1}); both areas are identified in all panels of Figure 5.9 by the thick green contours. These changes in total atmospheric liquid water content are associated with the higher cloud bases observed over the Central Mountain ridge and El Yunque (panel c), Figure 5.8), that in turn occur because of the northward shift of the convergence zone that produced convective activity over these regions (panels d and e, Figure 5.6). The Total Change in atmospheric column liquid water content also shows increasing values (0.03 to 0.12 g kg^{-1}) in the valley between the Central Mountains and El Yunque, south of the SJMA where the residential area of Caguas is located; both of these urban areas are identified by in Figure 5.9 by the thick black contour, and where the enhanced vertical motions are found (panel c), Figure 5.4; panels d) and e), Figure 5.6). Although this valley did not experience a significant change in cloud base height, the increased convective activity produced a deeper or denser cloud layer above the region.

The changes in wind magnitude and direction, cloud base heights, and total column liquid water content result in dramatic changes of total surface accumulated precipitation during the ERS in Puerto Rico, especially over regions where precipitation and low cloud cover occurrence is of extreme importance. Figure 5.10 shows the change in the three-month surface accumulated precipitation. Figure 5.11 presents these differences in terms of percent of change relative to the simulation with past LCLU (PAST1 and PAST2) for the LCLU signal cases, to the simulation with past climate conditions (PRESENT2 and PAST2) for the global warming signal cases, and to the simulation with past LCLU and past atmospheric and SST conditions (PAST2) for the Total Change case (see Table 5.1).

As with the previous variables discussed in this section, the LCLU change signal appears to have a limited contribution to the Total Change of the three-month accumulated surface precipitation, as seen in the results for the impact due to LCLU changes with present climate, panel a) (upper left, Figure 5.10) and with past climate conditions, panel b) (center top, Figure 5.10), and the precipitation differences that these two scenarios produced do not account for a significant percent of change (panels a and b, Figure 5.11). Panels d) and e) represent the global climate change signal for accumulated precipitation change (Figure 5.10) and percent change (Figure 5.11), for the simulation with present and past LCLU specifications, respectively. The similarity between panels a) and b) in Figures 5.10 and 5.11 indicates that changes due to LCLU changes are independent of global climate conditions, and vice versa for the similarity between panels d) and e). This also indicates, combined with the low impact the LCLU signal has on precipitation changes, that the global warming signal has a much stronger contribution to the Total Change and that it will closely follow the pattern observed in panels d) and e) (see panel c, in Figures 5.10 and 5.11). The Total Change, panel c) (upper right, Figures 5.10 and 5.11) presents precipitation difference values that range from -45 to -150mm throughout the Central Mountain range and El Yunque, regions identified by the thick green contours, with a maximum negative precipitation difference of up to 150mm at the higher elevations in the domain in the Central Mountains. These precipitation reductions are equivalent to a range of 6 to 13% change based on annual rainfall totals of 1100–1350mm for this region based on the PAST2 simulations. In the valley between the Central Mountains and El Yunque, the increased convective activity that lead to increased liquid water content also produced increased surface accumulated precipitation in the order of 15-30mm, which is a ~4% change from the 700mm of surface accumulated precipitation over that region.

These results for accumulated precipitation are of particular importance for small island states, mainly because tropical rain forests provide much of the natural resources, including fresh water, consumed in these countries. Therefore, it is equally important that the results for accumulated precipitation differences be compared with other datasets. Unfortunately, a reliable long-term record of station data for precipitation, like the temperature record presented in Chapters 1 and 4, is not available for the past climate

in Puerto Rico (1950s). Regardless, since the results presented in this study show that changes in precipitation appear to be mainly a large-scale global climate change impact, as opposed to be due to LCLU changes, and since most of the warming for the second half of the 20th century occurred since the mid to late 1970s (see Figure 1.3), the same trend should be evident in precipitation records from 1975-2004, a period for which reliable data exist for El Yunque. The analysis for precipitation change for the El Yunque station (Pico del Este, #26 in Figure 4.1) show a linear trend of precipitation decrease during the ERS at 20.7mm per decade, during the five decades that span the current study this results in a total precipitation reduction from 1955-59 to 2000-04 of 103.58mm, which is lower than the ~150mm shown by the model results, but as mentioned before the station results exclude the trend from 1955 to 1975. A large-scale global dataset with a 5x5˚ horizontal resolution reports a reduction in precipitation for the Caribbean basin of between 20 to 40% per century during the 1901-2005 period (Trenberth et al., 2007). This percentage is based on the means for the 1961 to 1990 period, and represents changes in year-round precipitation.

5.3 Thermal Response Number

Since the current release of atmospheric mesoscale model used, and the general surface energy budget model that is part of it, does not completely account for the thermal effects of heat storage or soil heat flux, and the LCLU characterization in RAMS uses a structural classification based on land cover classes and not on a functional classification to asses the impact of land cover in model results, a classifier is needed for the determination of the surface energy budget derived from surface or near surface temperatures for the various types of surfaces in a particular area. One feasible approach would be the use of the thermal response number (*TRN*) developed by Luvall and Holbo (1989) and applied to different surface types. The *TRN* is a surface property defined as the ratio of the surface net radiation, which integrates the effects of the non-radiative fluxes over short periods of time, and the rate of change in surface temperature, that expresses how those fluxes are reacting to radiant energy inputs.

The *TRN* (J m^{-2} $^{\circ}C^{-1}$) is then defined as:

$$TRN = (R_n \Delta t) / \Delta T , \quad (5.1)$$

where $(R_n \Delta t)$ represents the net radiation, R_n, over a time interval Δt and ΔT is the change in mean temperature for each surface type during Δt.

Then, in (5.1) R_n expresses the combined energies of the non-radiative surface processes and how these are partitioned at the surface following:

$$R_n = R_s\downarrow + R_l\downarrow + R_l\uparrow = H + LE + G, \quad (5.2)$$

where $R_s\downarrow$, $R_l\downarrow$, and $R_l\uparrow$ are the incident surface flux of shortwave and longwave radiation and the upward surface flux of longwave radiation, respectively. *H* is the surface sensible heat flux, *LE* the surface latent heat flux, and *G* the surface storage term or soil heat flux. This is a similar approach as the estimates of *G* derived as residuals in (5.2) and an objective hysteresis model (OHM) applied to urban surfaces in previous studies (Grimmond et al., 1991; Grimmond and Oke, 1999; Roberts et al., 2006).

The thermal response of an urban landscape may involve such surfaces as uniform asphalt parking lots, areas of high-rise steel and glass buildings, or residential areas with trees and lawns. The partitioning of energy budget terms depends on these surface types. In natural landscapes, the partitioning depends on canopy biomass, leaf area index, and moisture status, all of which vary according to the development stage of the ecosystem. In all cases, LCLU changes substantially alter the surface energy budget. Large *TRN* values means that more energy is required to increase that surface's temperature (Luvall et al., 1990). Areas that have mostly vegetated surfaces have a greater *TRN* than completely barren or built-up surfaces because the net radiation processed by the surface is mostly used for latent heat (evaporation of water) rather than sensible heat (heating the air). *TRN* values are useful in determining evapotranspiration and surface heat flux characteristics for common urban surfaces, and for assessing the thermal dynamics of these surfaces throughout the day (Luvall and Holbo, 1989; Luvall, 1997).

The 1x1km resolution of the model grid used for this research does not allow for the identification of individual surface elements (e.g., buildings, parking lots, parks), so to analyze the thermal response of different surfaces, as well as the impact of LCLU changes and global climate change on the *TRN*, the

SJMA and El Yunque are taken as regions representing heavily urbanized and vegetated/forested surfaces, respectively (see Figure 3.13).

Results for the *TRN* in the region occupied by the SJMA show how the presence of the city in the PRESENT1 and PRESENT2 simulations produce lower values than the simulations with a pre-urban land specification, PAST1 and PAST2, throughout the Caribbean ERS, showing ~100–200 kJ m^{-2} $^{\circ}C^{-1}$ against ~200–400 kJ m^{-2} $^{\circ}C^{-1}$, respectively, both with a positive slope as the season progresses (Figure 5.12, top left). This difference might be due to an increase in sensible heat flux in the urban scenarios related to an increase in surface temperature, which in turn raises air temperatures (as seen in the air temperature differences shown in Figures 5.1-5.4). The increasing pattern is a response to increasing moisture available in the atmosphere in the onset of the summer season. The partitioning of energy is analyzed using the model results for sensible and latent heat flux to calculate the Bowen ratio, *B*, as *H/LE*. The total change in *B*, PRESENT1 vs. PAST2, shows that there is more latent heat flux via evapotranspiration in the pre-urban scenarios and more sensible heat flux increasing the temperature of the surface in the urban scenarios (Figure 5.12, top right).

By analyzing the *TRN* and *B* patterns of the simulation with constant LCLU, it is concluded that changes in the thermal response of such surface are associated with increases in sensible heat flux in the simulations driven with present atmospheric conditions. Interesting results arise when comparing the simulations that produce similar *B* patterns, where it can be seen that major changes in the relationship between sensible and latent heat fluxes are due to changes in atmospheric conditions, further prove that there are drier atmospheric conditions during the present timeframe than in the past. Taking for example the PRESENT1 and PAST1 simulations having the same *B* pattern, and given that PRESENT1 has a much lower thermal response, then to maintain energy balance, the simulation with an urban representation must have increased thermal storage (*G*) in the SJMA region. Similar conclusions can be drawn from the results for the urbanized residential area of Caguas (Figure 5.12, center panels), with the distinction that the *TRN* and *B* have more variability, that might be due to the presence of more sub-grid vegetation patches in the urban cells in the Caguas region.

The montane cloud forest of El Yunque shows higher *TRN* values than the urban areas, and a much more pronounced increasing slope throughout the ERS, from ~300 kJ m^{-2} $^{\circ}C^{-1}$ to between 700-800 kJ m^{-2} $^{\circ}C^{-1}$ (Figure 5.12, bottom left). These results show how the forest still manages to consistently use more energy for evapotranspiration, increasing the latent heat flux in all scenarios ($B < 1$) for a great portion of the ERS (Figure 5.12, bottom right), in spite of having higher cloud base heights and decreased accumulated precipitation (see Figures 5.8 and 5.10). Also, the thermal response numbers produced by the past LCLU specifications are higher than those for the runs with present surface characteristics in El Yunque, although not as marked a difference as for the urban areas, where LCLU changes are far more dramatic.

In general, it is shown how the *TRN* provides a good measure of how a surface reacts to different radiative inputs in terms of surface temperature change over short periods of time (Δt of 1hr is used in this research), and how this is related to the way each surface type is partitioning the net surface radiation into non-radiative energies by applying the residuals approach to the surface energy budget terms (*H*, *LE*, *G*, and anthropogenic heat). It also provides an excellent indicator of local and regional environmental change that could be used to test different mitigation and adaptation strategies, depending on how the thermal response of a particular area changes to the application of such strategies.

Table 5.1: Climate Impact Scenario Description and Identification

Calculation	Climate Impact	Panel
PRESENT1-PAST1	LCLU change with present climate	a
PRESENT2-PAST2	LCLU change with past climate	b
PRESENT1-PRESENT2	Global climate change with present LCLU	c
PAST1-PAST2	Global climate change with past LCLU	d
PRESENT1-PAST2	Total Climate change (LCLU+GW)	e
[(PRESENT1-PAST1)-(PRESSENT2-PAST2)] ; [(PRESENT1-PRESENT2)-(PAST1-PAST2)]	Non-linear interaction between the two factors	f

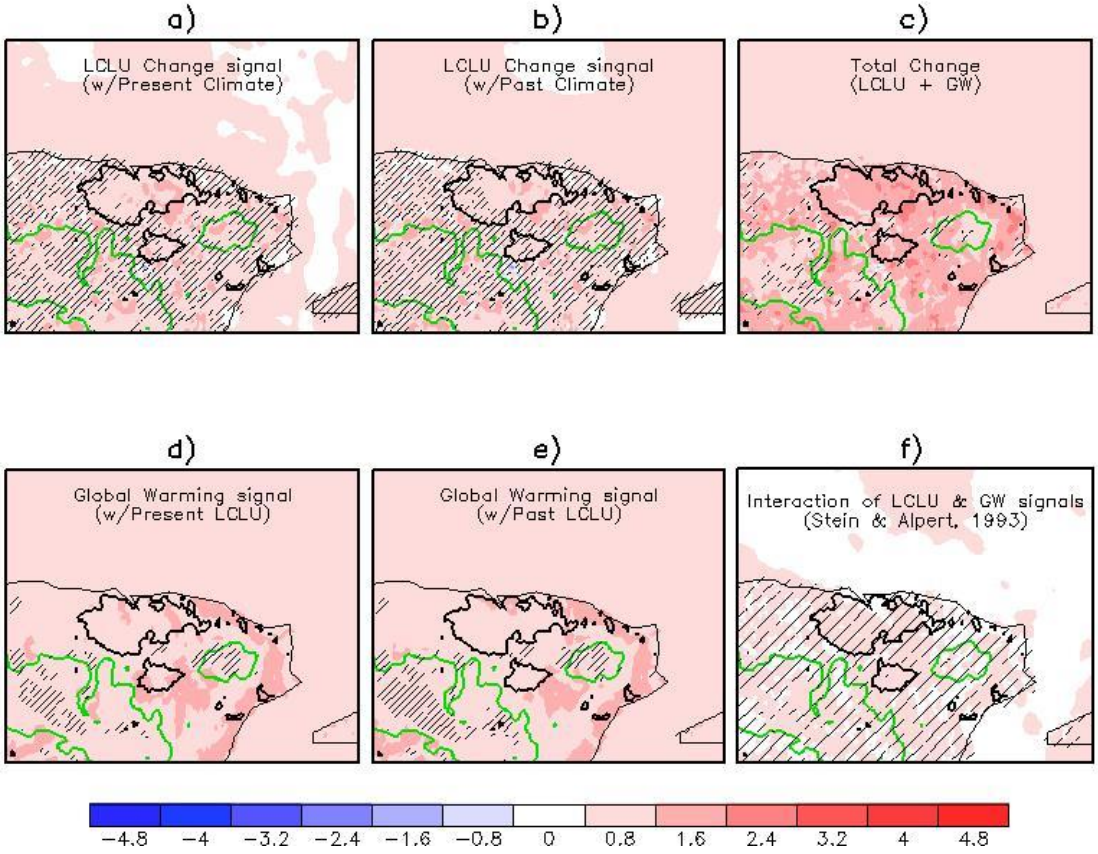

Figure 5.1: Differences in the minimum temperature (˚C) due to LCLU changes while driving the atmospheric mesoscale model with present atmospheric conditions (a, top left), due to LCLU changes while driving the model with past atmospheric conditions (b, top middle), due to global warming with present LCLU specifications (d, bottom left), due to global warming with past LCLU specifications (e, bottom middle), total change due to LCLU changes and global warming (c, top right), and the contribution due to the non-linear interaction among the LCLU and global warming factors (f, bottom right). The thick black line delineates the urban areas and the thick green line delineates the 350m-topography contour. The 45˚ hatch marks identify regions without statistically significant differences (at $\alpha_{LS} = 0.05$) (see Appendix D).

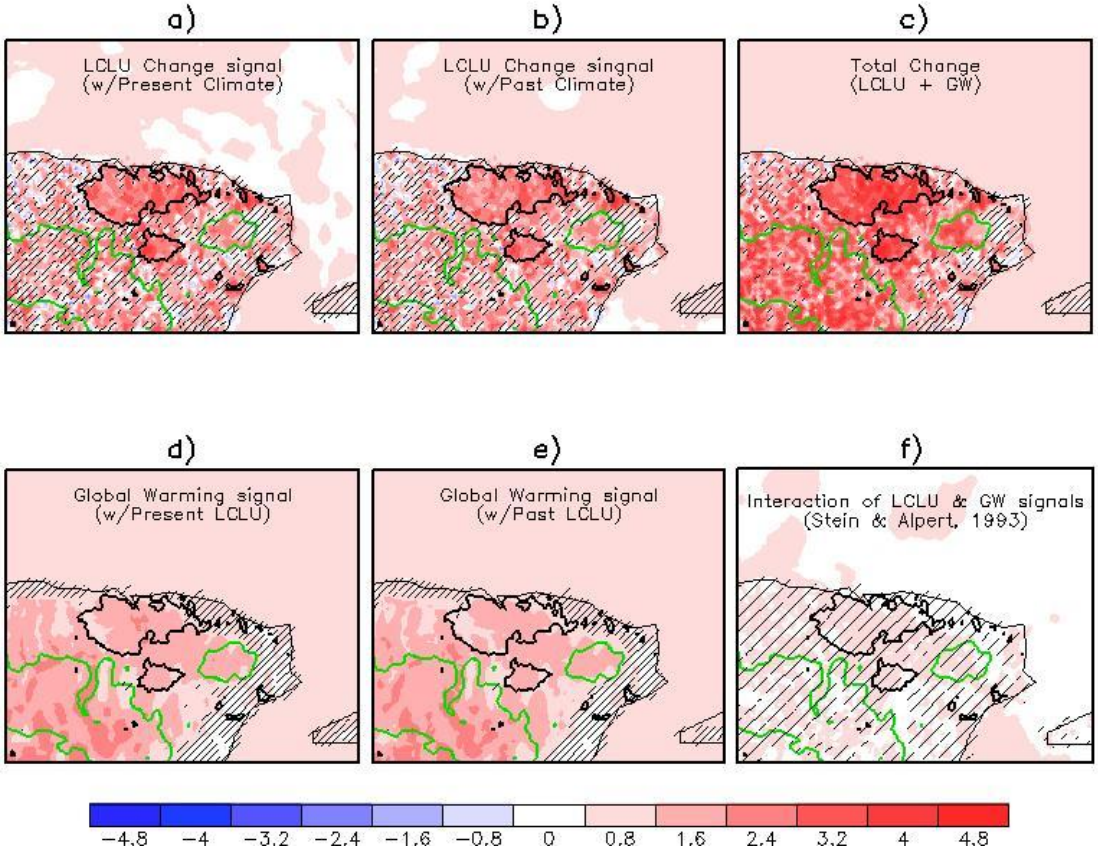

Figure 5.2: Differences in the maximum temperature (˚C) due to LCLU changes while driving the atmospheric mesoscale model with present atmospheric conditions (top left), due to LCLU changes while driving the model with past atmospheric conditions (top middle), due to global warming with present LCLU specifications (bottom left), due to global warming with past LCLU specifications (bottom middle), total change due to LCLU changes and global warming (top right), and the contribution due to the non-linear interaction among the LCLU and global warming factors (bottom right). The thick black line delineates the urban areas and the thick green line delineates the 350m-topography contour. The 45˚ hatch marks identify regions without statistically significant differences (at $\alpha_{LS} = 0.05$).

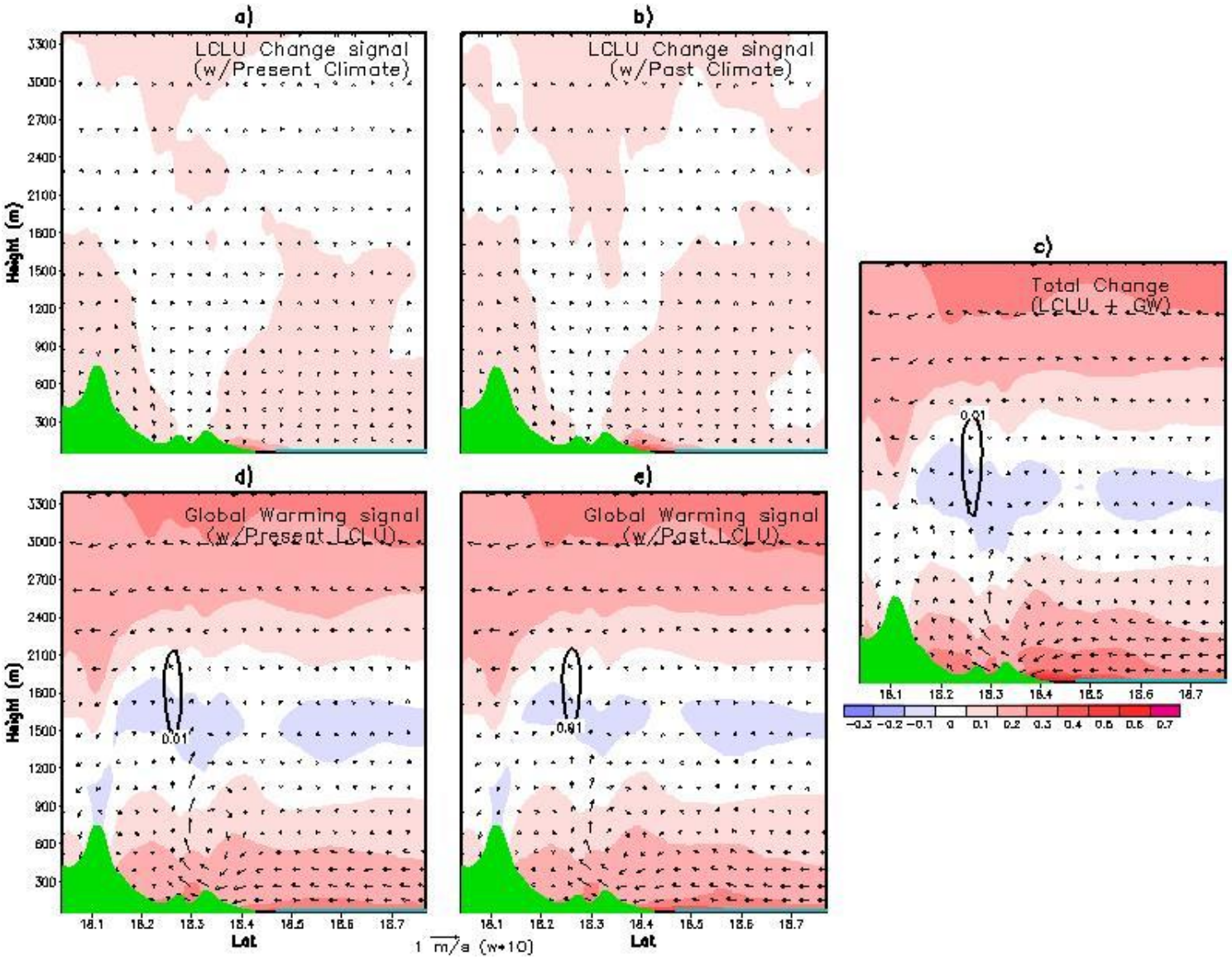
a)
LCLU Change signal
(w/Present Climate)
b)
LCLU Change singnal
(w/Past Climate)
c)
Total Change
(LCLU + GW)
d)
Global Warming signal
(w/Present LCLU)
e)
Global Warming signal
(w/Past LCLU)
Height (m)
Lat
1 m/s (w*10)

Figure 5.3: Vertical cross-sections, at the time when minimum temperatures occur and thru the north-south line in Fig. 3.1, of differences in temperature (˚C, shaded contours), liquid water mixing ratio (g kg^{-1}, black contours), and wind vectors due to LCLU changes while driving the atmospheric mesoscale model with present atmospheric conditions (top left), due to LCLU changes while driving the model with past atmospheric conditions (top right), due to global warming with present LCLU specifications (bottom left), due to global warming with past LCLU specifications (bottom right), and total change due to LCLU changes and global warming (far right). The thick blue line delineates sea surface and the thick green shade indicates underlying topography.

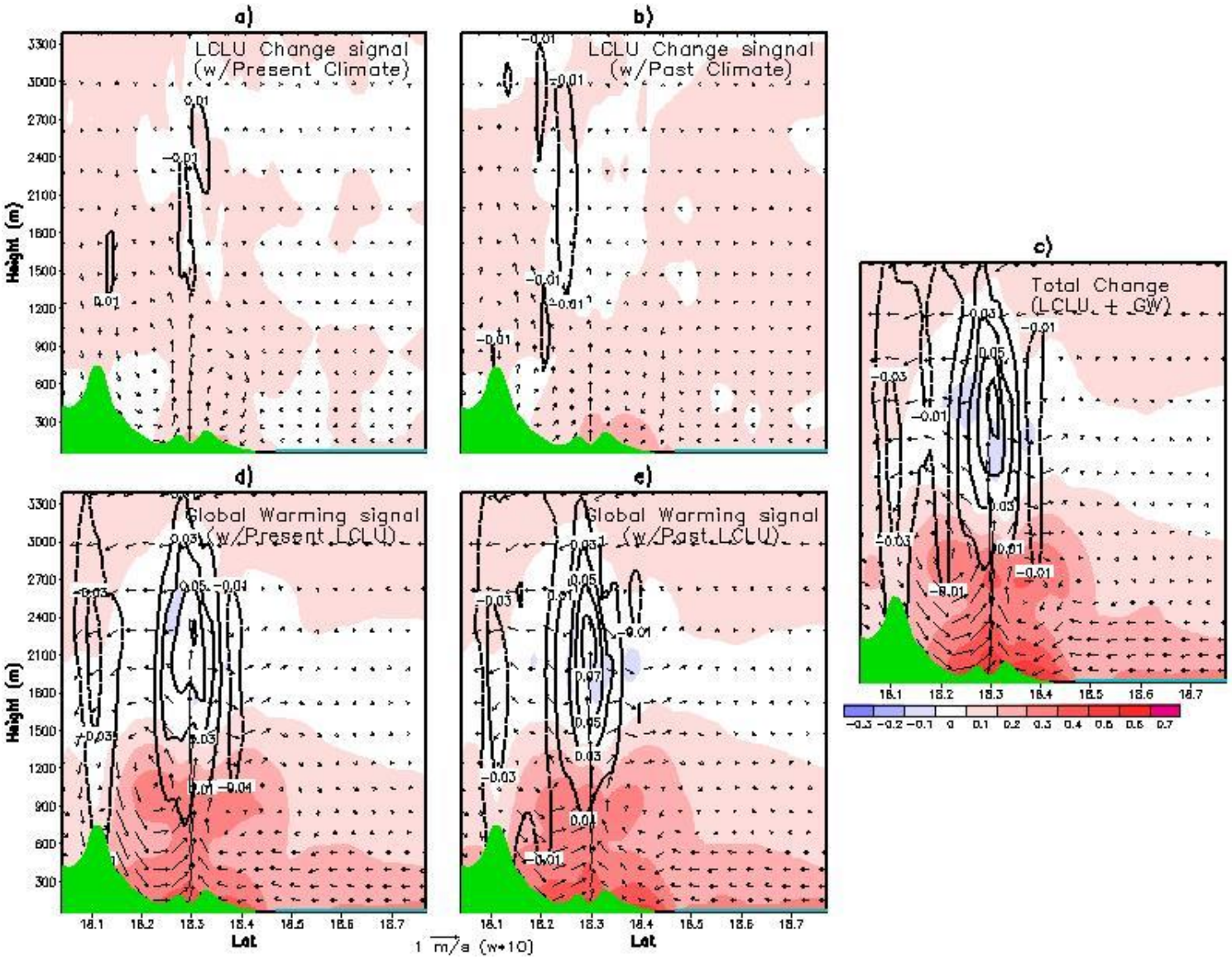
a)
LCLU Change signal
(w/Present Climate)
b)
LCLU Change singnal
(w/Past Climate)
c)
Total Change
(LCLU + GW)
d)
Global Warming signal
(w/Present LCLU)
e)
Global Warming signal
(w/Past LCLU)
Height (m)
Lat
1 m/s (w*10)

Figure 5.4: Vertical cross-sections, at the time when maximum temperatures occur and thru the north-south line in Fig. 3.1, of differences in temperature (˚C, shaded contours), liquid water mixing ratio (g kg^{-1}, black contours), and wind vectors due to LCLU changes while driving the atmospheric mesoscale model with present atmospheric conditions (top left), due to LCLU changes while driving the model with past atmospheric conditions (top right), due to global warming with present LCLU specifications (bottom left), due to global warming with past LCLU specifications (bottom right), and total change due to LCLU changes and global warming (far right).

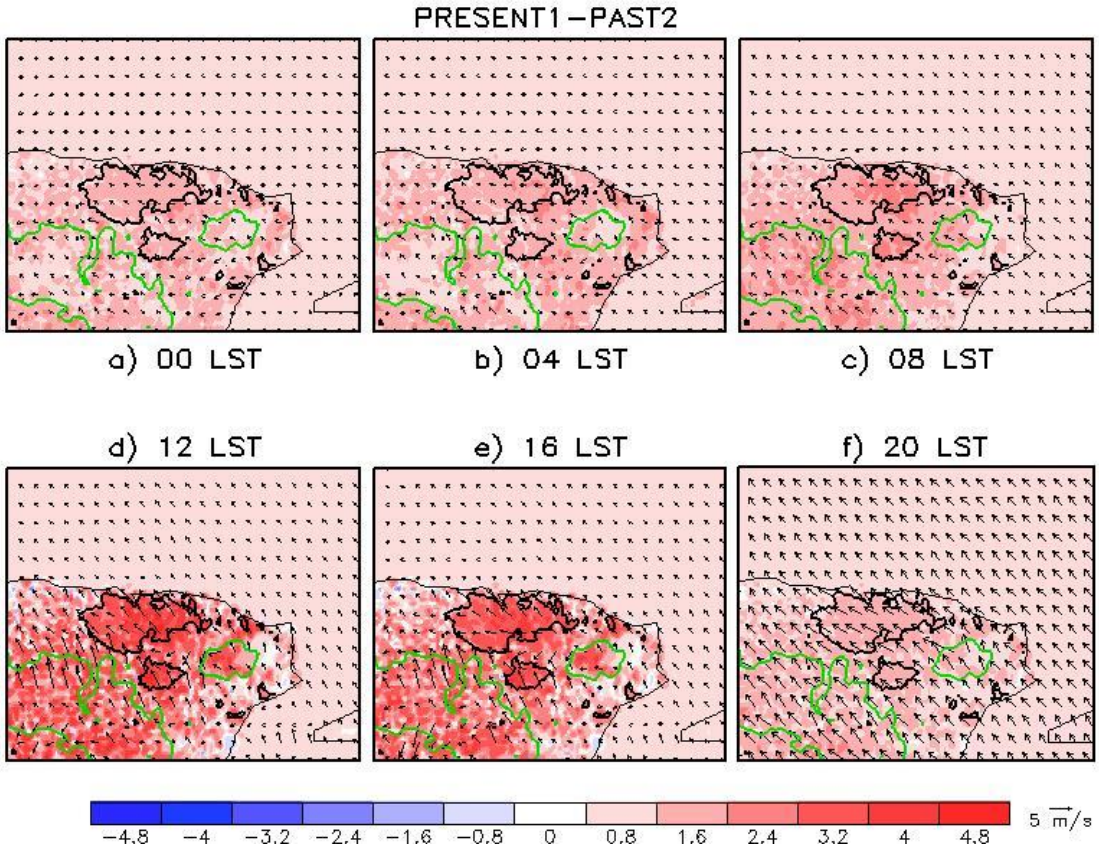

Figure 5.5: Daily cycle of temperature differences (˚C) and wind vector differences for the total climate change due to LCLU changes and global warming. The thick black line delineates the urban areas and the thick green line delineates the 350m-topography contour.

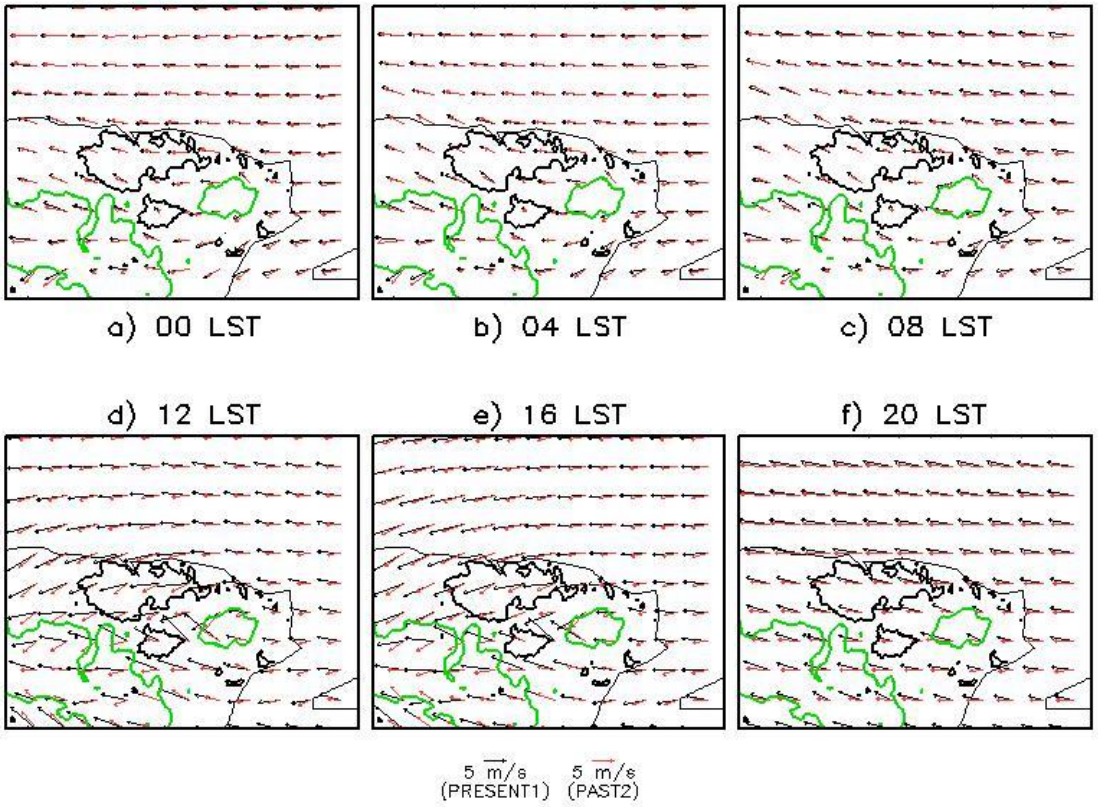

Figure 5.6: Daily cycle of the wind vector fields produced by the PRESENT1 simulations (black vectors) and the PAST2 simulations (red vectors). The thick black line delineates the urban area and the thick green line delineates the 350m-topography contour.

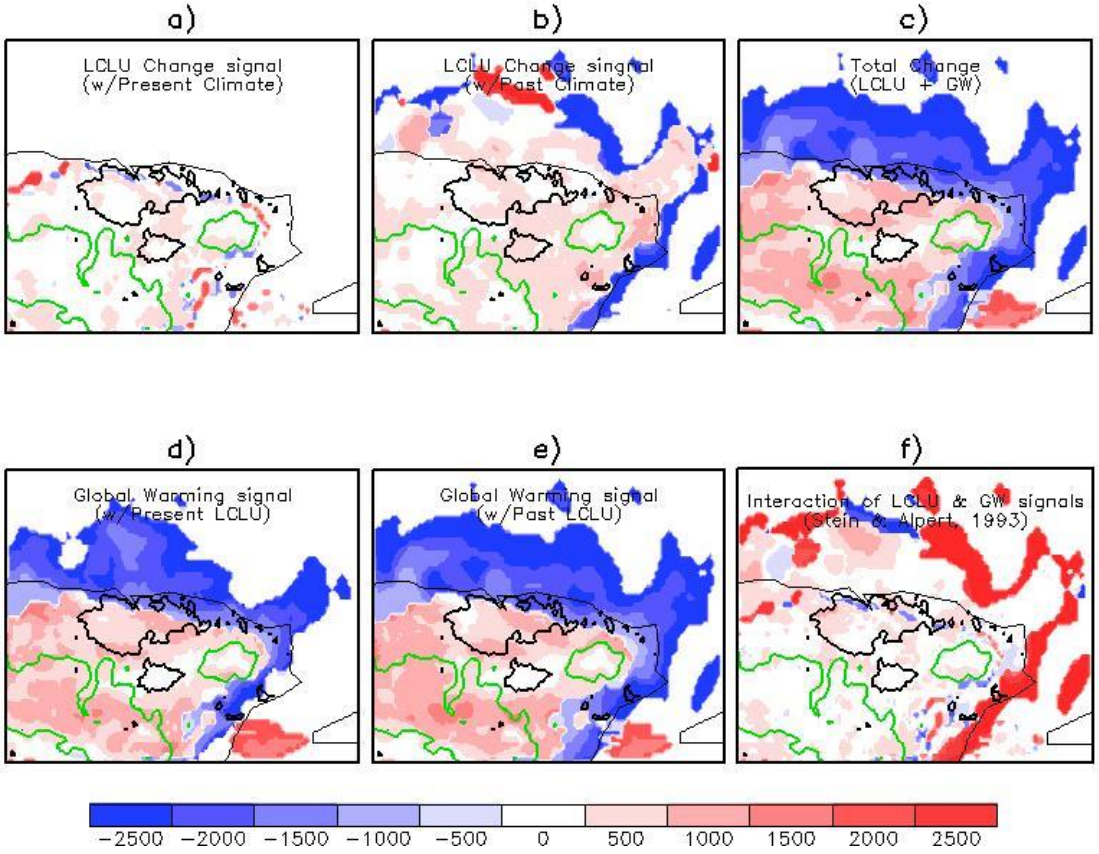

Figure 5.7: Differences in the cloud base height (m), at the 0.005 g kg^{-1} liquid water mixing ratio threshold, due to LCLU changes while driving the atmospheric mesoscale model with present atmospheric conditions (top left), due to LCLU changes while driving the model with past atmospheric conditions (top middle), due to global warming with present LCLU specifications (bottom left), due to global warming with past LCLU specifications (bottom middle), total change due to LCLU changes and global warming (top right), and the contribution due to the non-linear interaction among the LCLU and global warming factors (bottom right). The thick black line delineates the urban areas and the thick green line delineates the 350m-topography contour.

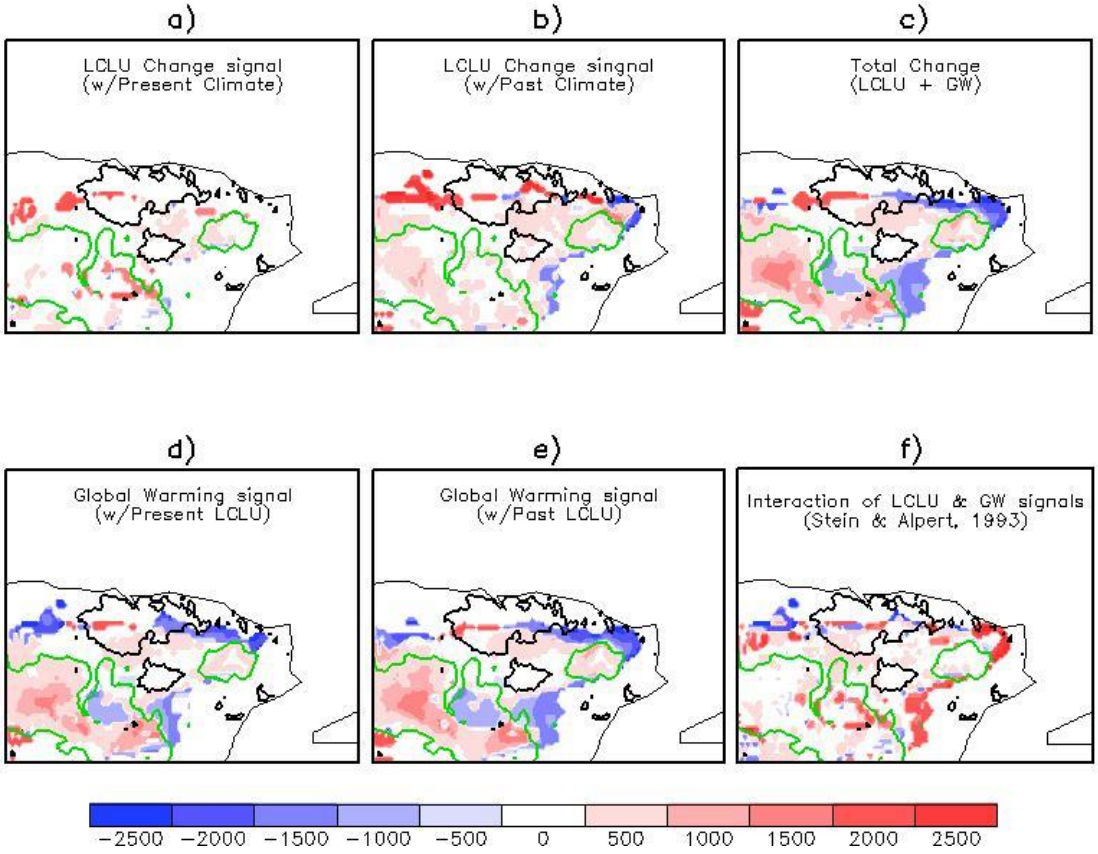

Figure 5.8: Differences in the cloud base height (m), at the 0.01 g kg^{-1} liquid water mixing ratio threshold, due to LCLU changes while driving the atmospheric mesoscale model with present atmospheric conditions (top left), due to LCLU changes while driving the model with past atmospheric conditions (top middle), due to global warming with present LCLU specifications (bottom left), due to global warming with past LCLU specifications (bottom middle), total change due to LCLU changes and global warming (top right), and the contribution due to the non-linear interaction among the LCLU and global warming factors (bottom right).

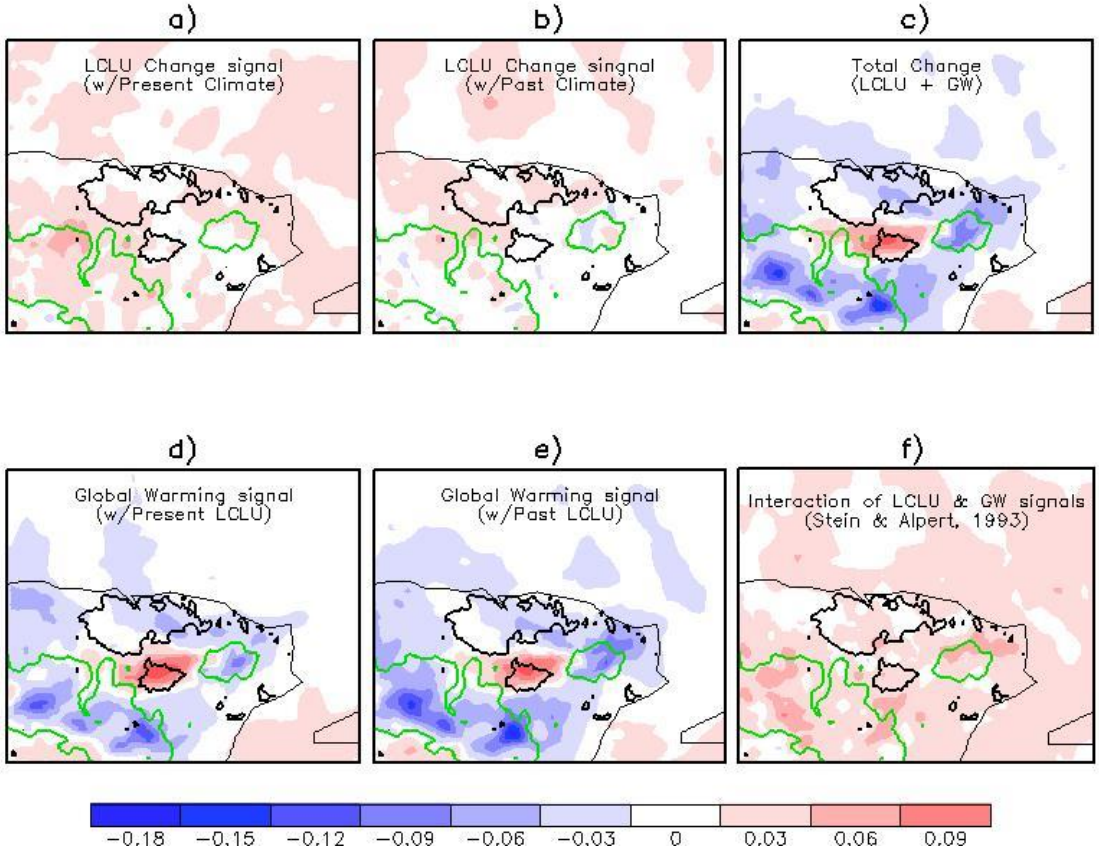

Figure 5.9: Differences in the total column liquid water content (g kg^{-1}) due to LCLU changes while driving the atmospheric mesoscale model with present atmospheric conditions (top left), due to LCLU changes while driving the model with past atmospheric conditions (top middle), due to global warming with present LCLU specifications (bottom left), due to global warming with past LCLU specifications (bottom middle), total change due to LCLU changes and global warming (top right), and the contribution due to the non-linear interaction among the LCLU and global warming factors (bottom right).

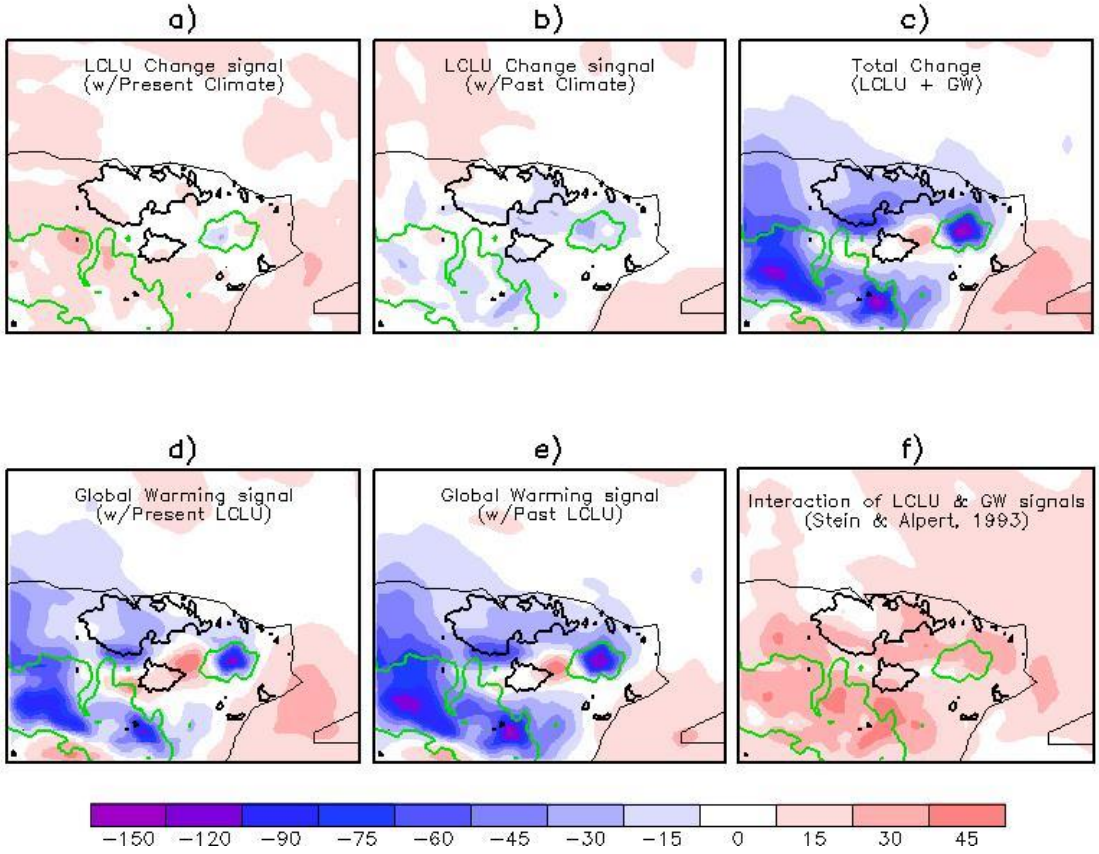

Figure 5.10: Differences in the total three-month accumulated surface precipitation (mm) due to LCLU changes while driving the atmospheric mesoscale model with present atmospheric conditions (top left), due to LCLU changes while driving the model with past atmospheric conditions (top middle), due to global warming with present LCLU specifications (bottom left), due to global warming with past LCLU specifications (bottom middle), total change due to LCLU changes and global warming (top right), and the contribution due to the non-linear interaction among the LCLU and global warming factors (bottom right).

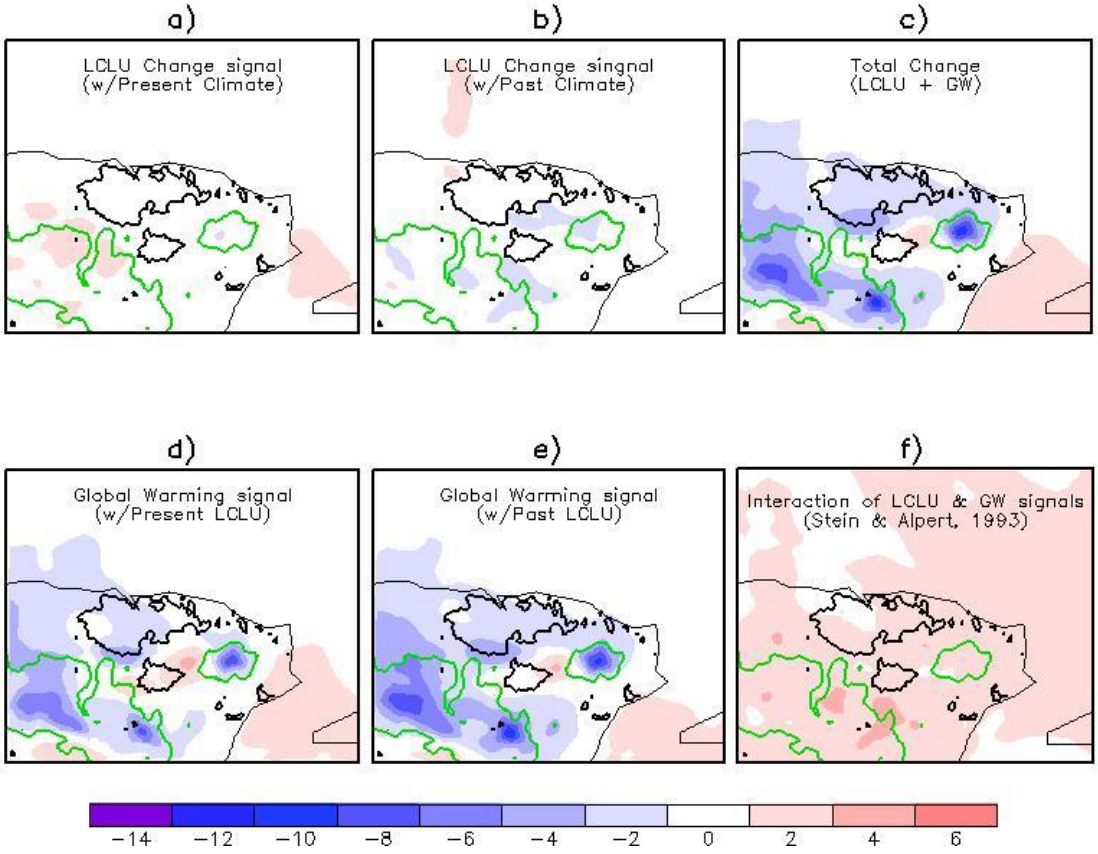

Figure 5.11: Percent change in the total three-month accumulated surface precipitation (%) due to LCLU changes while driving the atmospheric mesoscale model with present atmospheric conditions (top left), due to LCLU changes while driving the model with past atmospheric conditions (top middle), due to global warming with present LCLU specifications (bottom left), due to global warming with past LCLU specifications (bottom middle), total change due to LCLU changes and global warming (top right), and the contribution due to the non-linear interaction among the LCLU and global warming factors (bottom right).

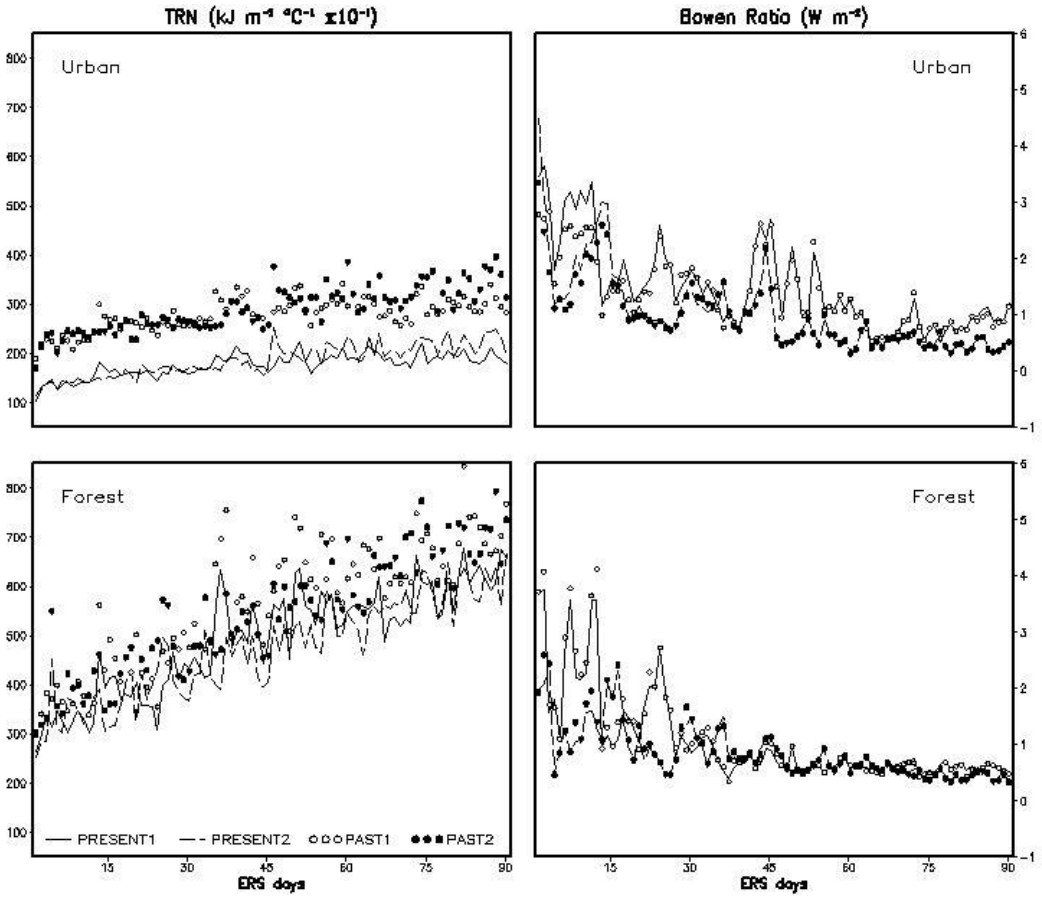

Figure 5.12: Time series of daily Thermal Response Number (kJ m^{-2} $^{\circ}C^{-1}$) (left panels) and Bowen ratio values (right panels) during the Caribbean ERS, calculated for the San Juan Metropolitan Area (top) and El Yunque (bottom). In all panels the four simulations in Table 3.1 are shown describing the runs with present LCLU and present atmospheric conditions (solid line), with present LCLU and past atmospheric conditions (dashed line), with past LCLU and present atmospheric conditions (open circles), and with past LCLU and past atmospheric conditions (closed circles).

Chapter 6

Summary and Conclusions

The work presented here is an investigation of the climate impacts of land cover and land use (LCLU) changes in coastal tropical regions under conditions of global climate change (global warming, GW) using the Regional Atmospheric Modeling System (RAMS) as the main research tool and by taking the northeastern region of the Caribbean island of Puerto Rico as the test case. A numerical modeling matrix was designed to answer the following research questions:

1) What has been the effect of LCLU changes on the local and regional early rainfall season climate of tropical coastal regions?

2) What has been the climatic impact of global climate change on tropical coastal regions during the region's early rainfall season?

3) Under these conditions of LCLU changes and global climate change, what has been their combined effect (LCLU and global climate change) in tropical coastal regions?

The simulation matrix combines two large-scale atmospheric conditions to drive the model and two LCLU scenarios for the corresponding atmospheric timeframes to provide the surface characteristics for the simulations. The two five-year periods from 1955 to 1959, for the past conditions, and from 2000 to 2004, for the present conditions, were selected under a series of criteria that minimizes the influences of global scale oscillations (e.g., ENSO and NAO) in the Caribbean early rainfall season (ERS) climate, that represents a significant climate change in the region of interest and that are in accordance with historical LCLU changes in Puerto Rico. The NCEP Reanalysis 2.5˚ 6-hourly data and the Smith and Reynolds ERSST v3b monthly data provided the large-scale atmospheric and oceanic conditions, respectively. The LCLU specifications for each period were obtained from digital maps of vegetation cover for 1951 and 2000, with the present specifications

complemented by remote sensing information to have a better representation of the current urban areas located in the modeling domain.

To validate the model's ability to reproduce the climate corresponding to each timeframe, the five-year climatology from the simulations with present LCLU and present atmospheric and SST conditions (PRESENT1), and from the simulation with past LCLU and past atmospheric conditions and SSTs (PAST2), were compared against observations of maximum and minimum temperatures recorded by cooperative (COOP) surface stations located in the SJMA and El Yunque. The validation exercise demonstrated that the proposed modeling methodology is capable of replicating specific weather events and represents an improvement in producing surface and air temperature in the region of study (Comarazamy et al., 2010), as well as the past and present climatology used to perform the climate impact study. The validation was particularly satisfactory taking into account the different reconstructed datasets that are incorporated into the modeling system, and it was thus considered appropriate to conduct the type of climate impact study presented in this document.

In terms of the climate impacts due to LCLU changes in tropical coastal regions, Question 1, model results show that LCLU changes produced the largest air temperature difference values, with high statistical significance (at $\alpha_{LS} = 0.05$) over heavily urbanized regions, especially for the case of maximum temperatures, but the pattern was also present in the results for minimum temperatures. Over non-urban areas, the areas of heating are scattered throughout the rest of the domain, as the changes in LCLU were not as homogeneous in space as in the expansion of the SJMA and Caguas. The changes in minimum and maximum temperature due to LCLU changes are limited to vertical levels near the surface (below 400m). To further emphasize the impact of LCLU changes, the thermal response number (TRN) of the area occupied by the SJMA has decreased as a consequence of replacing the low land coastal plain vegetation with man made materials, indicating that it takes less energy to raise the surface temperature of the region in question, whereas the thermal response of the forested region has remained virtually unchanged.

The influence of the global warming signal to the reported temperature changes, Question 2, is to induce a temperature change gradient for maximum temperature inland from the coastline to the higher elevations of the Central Mountains. This gradient of temperature changes starts with a slight cooling in the low land coastal plains along the eastern and southeastern coastlines, possibly due to increased trade winds in the present climatology, but results across these regions had low statistical significant values (at $\alpha_{LS} = 0.1$). In terms of minimum temperatures, the global warming signal induces temperature increases along the coastal plains and in a narrow valley located between the Central Mountains and El Yunque. The changes in minimum and maximum temperatures due to global climate change penetrate deeper into the atmosphere that in the LCLU change cases, following the vertical temperature change of the large-scale NCEP input.

The global climate change signal was also found to have an important role in producing changes in the region's wind pattern by increasing the magnitude of the approaching trade winds and by changing its direction to an easterly or slightly southeasterly flow. These changes cause a shift in the location of a convergence zone at the time of highest temperature difference values in the daily evolution of the Total Change case. The convergence zone had its axis along the ridge of the Central Mountain range in the simulations driven by past climate conditions, and this axis changed to a northern position just off the range's foothills in the simulations driven by the present climatology. Without the added orographic lifting mechanism that enhance convection above the mountaintops and accounts for cloud formation and rain development in those area, the base of the clouds are higher and the total column liquid water content decreased along the Central Mountain ridge and El Yunque. This combination of elements translates into a dramatic decrease in surface accumulated precipitation during the ERS in the region of interest, with strong precipitation reductions in the Central Mountain range and El Yunque. The shift in the convergence zone leads to increase vertical motions over its present location that do not cause a lifting of the cloud base heights along its axis in the present location, but increased amounts of total column liquid water content are present in the region between El Yunque and the Central Mountains. This suggests the presence of either a thicker cloud layer in that column, or a cloud with increased concentration of cloud droplets and/or raindrops over Caguas that

turn leads to an increase of surface accumulated precipitation in that zone. The global warming signal also has effects on the thermal response of the region occupied by the SJMA, where the dryer present conditions generate lower TRN values than in the past climate conditions for both LCLU chases. These differences from the global warming signal are more evident in the Bowen ratio pattern for the simulation driven by the present atmospheric and SST conditions and in those driven with past climate conditions. Differences in the thermal response of the forest due to global climate changes are less evident, with the exception of the onset of the ERS, when the pattern in the Bowen ratio follows the same pattern as in the urban area.

Regarding the combined effects of LCLU changes and global warming, Question 3, the similarity between the LCLU signal while running the model with the present climate conditions and the past climate conditions indicates that the impact of LCLU changes on minimum and maximum temperatures is relatively independent of the large-scale conditions that drive the model in those simulations, and vice versa for the similarity between the global warming signal cases, where changes due to global climate change are independent of the LCLU specifications used as surface characteristics. This results in both signals having an important role in the Total Change results for temperature changes, producing higher temperature differences over urban areas and a difference gradient inland that peaks over the Central Mountain ridge. A similar situation was found for the cases of total column liquid water content and surface accumulated precipitation, but in these cases the LCLU change signal did not produce significant changes in the variable in question, so it was concluded that only the global climate change signal had a strong contribution to the Total Change. In the case of cloud base height difference, a large-scale climate influence was found in the LCLU signal, and vice versa, but this was mainly due to trace amounts of liquid water present at high atmospheric levels in the PAST2 simulation; this influence was not found in the results for total column liquid water content.

6.1 Implications to Local Populations

The reported changes in temperature and precipitation would have serious consequences to small island states located in tropical regions. The world's industrial powers are responsible for over 50% of total global emissions of green house gases, the main cause of global warming and resultant climate change. Developing countries emit less than 25% of the total GHG emissions, and Small Island Developing States (SIDS) are responsible for less than 1% of global emissions. SIDS have had a limited contribution to the problem of global warming, but are among the most vulnerable groups to global climate change, and because of their nature, have low mitigation capacity. Hence adaptation rather than mitigation is a more appropriate course for dealing with global warming. In terms of local environmental changes, SIDS and other developing coastal tropical regions are responsible for much of the LCLU changes and therefore responsible for its underlying climate impacts, probably because of the limited availability of resources. In many instances local governments have made a conscientious effort to protect their natural areas by setting aside large portions of tropical montane rain and cloud forests as natural reserves, but uncontrolled urban sprawl remains one of the most important contributors to total climate changes due to LCLU changes.

The increase temperatures caused by LCLU changes and global warming could lead heat stress, danger of heat stroke, and hazardous atmospheric conditions due to increased pollution and temperatures, especially for the more sensitive sectors of the population, due to a combination of increased air temperature and pollution. Increased air conditioning demands within urban centers would in turn increase energy demands in regions with serious utilities distribution problems. Changes in precipitation patterns can cause droughts or floods, depending on the actual climate change impact for a particular location, and can induce a reduction in dam capacity and fresh water availability, which is one of the most important long-term impacts to the local population.

Tropical montane cloud forests occupy approximately 0.4% of the Earth's surface, but they support approximately 20% of the planet's plant and vertebrate diversity. Its main characteristic is that the base of its cloud is climatologically below the vegetation canopy (Hamilton et al., 1993). During the dry season and in the onset of the rain season, tropical montane cloud forests directly capture

moisture from the clouds, accounting for 15–100% of their total precipitation (Bruijnzeel and Proctor, 1993). Therefore, the predicted rise in cloud base heights reported in this study would seriously hamper this moisture source. This in turn would impact local ecological communities and the area's biodiversity, and would thus affect the geographic extension of the forest, effectively reducing the area covered by montane cloud forests (Lawton et al., 2006). The local and regional changes reported here and in other studies would increase the rate of extinction of cloud forest species, and thus many cloud forests around the world are now threatened by local and global factors (Still et al., 1999; Pounds et al., 1999). The Luquillo Experimental Forest, a well-protected montane cloud forest in Puerto Rico, is an example of this, as they are threatened by global changes that have an impact in the region's hydrological cycle and that are impossible to manage locally (Figures 5.7-5.10). This research shows that the rise of cloud base heights in elevated terrain is most likely a consequence of global climate change. In agreement with previous studies, the currently predicted increasing SSTs are found responsible for rising cloud base heights in tropical montane cloud forests (Still et al., 1999; Pounds et al., 1999). The current results, however, seem to be in partial contradiction with results from the Monteverde forest in Costa Rica, where lowland deforestation (LCLU changes) in the coastal plains is responsible for drying the air masses, leading to rising clouds bases (Lawton et al., 2001; Nair et al., 2003; Ray et al., 2006). These latter studies in Costa Rica only explore the deforestation signal in their numerical experiments, completely neglecting other cases of LCLU changes and the global warming signal.

There could also be impacts to the tourism industry due to coastal flooding and erosion, loss of biodiversity could affect ecotourism, and milder northern winters could reduce the number of annual visitors. Reported economic impacts of climate change in the Caribbean range from loss of employment in the tourism industry, loss of crops because of droughts, possible flood damages, loss of fisheries production, increased costs of public health care, among others.

To summarize, there is a myriad of secondary and tertiary social, economic, and cultural implications of the total climate change due to the combine effects of LCLU changes and global

warming in coastal tropical regions. This is the main reason why comprehensive research like the one described in this document is of extreme importance. To have the most reliable information, with the most relevant factors included in the analysis, is to be able to make appropriate adaptation and mitigation strategies that would have the most impact.

6.2 Future Work

To improve the results presented in this document, an investigation of parameters that can be extracted from remote sensing information to update the atmospheric model surface characteristics should be performed. Parameters such as albedo, emisivity, surface roughness, leaf area index, vegetation fraction, among other surface characteristics, as well as other important parameters used in regional atmospheric modeling, like skin/canopy temperature, volumetric soil moisture content, and soil textural class could be incorporated into the measurements obtained by the next generation of remote sensors, like the Hyperspectral-Infrared Imager (HyperIRI) satellite which may launch in 2023. Given the sensitivity to cloud base for pristine tropical forests, next generational sensors should include capabilities to detect cloud base and depth, may be through the use of active sensors (e.g., radars and lidars). In addition to an improvement on input parameters, in terms of analysis of the model results, a better representation of the cloud base height difference should be explored, as well as a more adequate re-sampling method to perform the Monte Carlo experiments in the test for field significance (see Appendix D).

For future studies in other tropical coastal regions, a natural extension of the work presented in this document is to apply the methodology of separating the signals of LCLU changes and global climate change in other islands in the Caribbean region, areas in Mesoamerica (southern Mexico and Central America), and some regions of Southeast Asia. The methodology proposed in this research could be applied to other islands in the Caribbean. These regions follow similar LCLU change patterns and urban development, are located in a region dominated by the same large-scale climate regime, and would have comparable changes in the surrounding SSTs. In Costa Rica for example, several numerical studies of climate impacts due to LCLU changes have been performed (Lawton et al., 2001;

Nair et al., 2003; Ray et al., 2006). These studies have taken into consideration the effects of forestation and deforestation in the Monteverde cloud forest (Ray et al., 2006). With the inclusion of urbanization around the protected area and the major urban center in Costa Rica, combined with two global climate change scenarios (IPCC, 2007; Trenberth et al., 2007), the relative contribution to the total climate change in Costa Rica due to LCLU changes and global warming could be quantified. Other coastal tropical regions where similar research could be carried out could include several areas in Southeast Asia: the Philippines, Indonesia, and other islands (Myers et al., 2000). They represent regions where large populations live in sprawling urban centers located in close proximity to pristine rain forests and other areas where LCLU changes are present.

Projections for future climate changes in tropical coastal regions could be performed using both different GHG emissions scenarios (Meehl et al., 2007) and statistical data for future population growth as a proxy for urban development (Velazquez-Lozada et al., 2006). Downscaled and detailed climate change projections are a priority to be able to establish critical mitigation and adaptation policies. In cases where the LCLU change includes urban areas with deep urban canyons and where the balance of energy at the surface could be affected by the presence of tall buildings, a more sophisticated urban canopy energy model should be coupled to the atmospheric model chosen for the studies (Masson, 2000; Martilli et al., 2002; McCarthy et al., 2010). The findings discussed in Chapter 5 apply to late 20th century urbanization and climate change, a period what saw a dramatic expansion of urbanization and other cases of LCLU changes in Puerto Rico, and only modest large-scale warming. The implications would be that if the warming continues as projected above, what has been experienced recently, presuming that urbanization has reached a relative stable extent (and may see some reduction of its impact due to expansion of reflective and green roofs, greater urban vegetation, reforestation programs, etc), the future will not show the same relative effects as experienced during the study period presented in this document.

References

Aceituno, P., 1988. On the functioning of the Southern Oscillation in the South American sector. Part I: surface climate. Monthly Weather Review, 116, 505-524.

Angeles, M. E., Gonzalez, J. E., Erickson III, D. J., and Hernández, J., L., 2007. Predictions of future climate change in the Caribbean region using global circulation models. International Journal of Climatology, 27, 555-569.

Angeles, M. E., González, J. E., Ramírez- Beltrán, N. D., Tepley, C. A., and Comarazamy, D. E., 2010. Origins of the Caribbean rainfall bimodal behavior. Journal of Geophysical Research, 115, D11106, doi:10.1029/2009JD012990.

Bornstein, B., and Lin, Q., 2000. Urban heat islands and summertime convective thunderstorms in Atlanta: three case studies. Atmospheric Environment, 34, 507-516.

Brockman, V. M., 1952. The rural land classification program of Puerto Rico. Northwestern University, Studies in Geography, Evanston, IL.

Bruijnzeel, L. A., and Proctor, J., 1993. Hydrology and biogeochemistry of tropical montane cloud forests: What do we really know? In: Tropical Montane Cloud Forests: Proceedings of an International Symposium [L. S. Hamilton, J. O. Juvik, and F. N. Scatena (Eds.)]. pp. 25-46.

Burnaby, T. P., 1953. A suggested alternative to the correlation co- efficient for testing the significance of agreement between pairs of time series, and its application to geologic data. Nature, 172, 210-211.

Cenedese, A., Miozzi, M., and Monti, P., 2000. A laboratory investigation of land and sea breeze regimes. Experiments in Fluids, 29, 291–299.

Cenedese, A., and Monti, P., 2003. Interaction between n inland urban heat island and a sea-breeze flow: A laboratory study. Journal of Applied Meteorology, 42, 1569-1583.

Chen, A. A., and Taylor, M. A., 2002. Investigating the link between early season Caribbean rainfall and the El Niño+1 year. International Journal of Climatology, 22, 87-106.

Comarazamy, D. E., and González, J. E., 2008. On the validation of the simulation of early season precipitation on the island of Puerto Rico using a mesoscale atmospheric model. Journal of Hydrometeor, 9, 507-520.

Comarazamy, D. E., González, J. E., Luvall, J. C., Rickman, D. L., and Mulero, P. J., 2010. Impacts of urbanization in the coastal tropical city of San Juan, Puerto Rico. Earth Interactions, *In Press*.

Cotton, W. R., Pielke Sr., R. A., Walko, R. L., Liston, G. E., Tremback, C. J., Jiang, H., McAnelly, R. L., Harrington, J. Y., Nicholls, M. E., Carrio, G. G., and McFadden, J. P., 2003. RAMS 2001: Current status and future directions. Meteorology and Atmospheric Physics, 82, 5-29.

Dai, A., Tremberth, K. E., and Karl, T. R., 1999. Effects of clouds, soil moisture, precipitation, and water vapor on diurnal temperature range. Journal of Climate, 12, 2451-2473.

Daly, C., Helmer, E. H., and Quiñones, M., 2003. Mapping the climate of Puerto Rico, Vieques and Culebra. International Journal of Climatology, 23, 1359-1381.

Dickinson, R. E., Sellers A. H., Kennedy P. J., and Wilson, M. F., 1986. Biosphere-Atmosphere Transfer Scheme (BATS) for the NCAR Climate Community Model. Technical Note NCAR/TN-275+STR. 69 pp.

Dixon, P. G., and Mote, T. L., 2003. Patterns and causes of Atlanta's urban heat island-initiated precipitation. Journal of Applied Meteorology, 42, 1273-1284.

Duchon, C. E., 1986. Temperature trends at San Juan, Puerto Rico. Bulletin of the American Meteorological Society, 67, 1370-1377.

Elmore, K. L., Baldwin, M. E., and Schultz, D. M., 2006. Field significance revisited: spatial bias errors in forecasts as applied to the Eta model. Monthly Weather Review, 134, 519-531.

Ewel, J. J., and Whitmore, J. L., 1973. The ecological life zones of Puerto Rico and the U.S. Virgin Islands. Research Paper ITF-018, USDA Forest Service, Institute of Tropical Forestry, 74 pp.

Feddema, J., Oleson, K., Bonan, G., Mearns, L., Washington, W., Meehl, G., and Nychka, N., 2005. A comparison of a GCM response to historical anthropogenic land cover change and model sensitivity to uncertainty in present-day land cover representations. Climate Dynamics, 25, 581–609, DOI 10.1007/s00382-005-0038-z.

Franco, P. A., Weaver, P. L., Eggen-McIntosh, S., 1997. Forest resources of Puerto Rico, 1990. Resource Bulletin SRS-22, USDA Forest Service, Southern Research Station, Ashville, NC, 45 pp.

Freitas, E. D., Rozoff, C. M., Cotton, W. R., and Silva Dias, P. L., 2007. Interactions of an urban heat island and sea-breeze circulations during winter over the metropolitan area of Sao Paulo, Brazil. Boundary-Layer Meteorology, 122, 43-65, DOI 10.1007/s10546-006-9091-3.

Giannini, A., Kushnir, Y., and Cane, M. A., 2000. Interannual variability of Caribbean rainfall, ENSO and the Atlantic Ocean. Journal of Climate, 13, 297–311.

Giannini, A., Cane, M. A., and Kushnir, Y., 2001a. Interdecadal changes in the ENSO teleconnection to the Caribbean region and the North Atlantic Oscillation. Journal of Climate, 14, 2867-2879.

Giannini, A. Kushnir, Y., and Cane, M. A., 2001b. Seasonality in the impact of ENS0 and the North Atlantic high on Caribbean rainfall. Physics and Chemistry of the Earth, 26, 2, 143-147.

González, J. E., Luvall, J. C., Rickman, D., Comarazamy, D. E., Picón, A. J., Harmsen, E. W., Parsiani, H., Ramírez, N., Vázquez, R., Williams, R., Waide, R. B., and Tepley, C. A., 2005. Urban heat islands developing in coastal tropical cities. EOS Transactions, AGU, 86, 42, pp. 397 & 403.

González, J. E., Luvall, J. C., Rickman, D., Comarazamy, D. E., and Picón, A. J., 2006. Urban heat island identification and climatological analysis in a coastal, tropical city: San Juan, Puerto Rico. In: Urban Remote Sensing [Q. Weng and D. Quattrochi (Eds.)]. CRC Press, Boca Raton, FL, pp. 223-252.

Grimmond, C. S. B., H. A. Cleugh, and T. R. Oke, 1991. An objective heat storage model and its comparison with other schemes. Atmospheric Environment, 25B, 311–326.

Grimmond, C. S. B., and T. R. Oke, 1999. Heat storage in urban areas: local-scale observations and evaluation of a simple model. Journal of Applied Meteorology, 38, 922–940.

Hamilton, L. S., Juvik, J. O., and Scatena, F. N., 1993. The Puerto Rico tropical cloud forest symposium: Introduction and workshop synthesis. In: Tropical Montane Cloud Forests [L. S. Hamilton, J. O. Juvik, and F. N. Scatena (Eds.)]. pp. 1-16.

Hastenrath, S. 1976. Variations in the low-latitude circulation and extreme climatic events in the tropical Americas. Journal of Atmospheric Science, 33, 202-215.

Helmer, E. H., Ramos, O., López, T. del M., Quiñonez, M., and Diaz, W., 2002. Mapping the forest type and land cover of Puerto Rico, a component of the Caribbean biodiversity hotspot. Caribbean Journal of Science, 38, 165-183.

Herlmer. E. H., 2004. Forest conservation and land development in Puerto Rico. Landscape Ecology, 19, 29-40.

Imamura, I. R., 2005. Micrometeorological observations of urban heat islands in different climate zones. International Journal of Climatology, 1-31.

Intergovernmental Panel on Climate Change, 2007. Summary for policymakers. In: Climate Change 2007: The Physical Science Basis. Contribution of Working Group I to the Fourth Assessment Report of the Intergovernmental Panel on Climate Change [Solomon, S., D. Qin, M. Manning, Z. Chen, M. Marquis, K.B. Averyt, M.Tignor and H.L. Miller (eds.)]. Cambridge University Press, Cambridge, United Kingdom and New York, NY, USA.

Inoue, T., and Kimura, F., 2004. Urban effects on low-level clouds around the Tokyo metropolitan area on clear summer days. Geophysical Research Letters, 31, L05103, doi:10.1029/2003GL018908.

Jauregui, E., 1997. Heat island development in Mexico City. Atmospheric Environment, 31, 3821-3831.

Jauregui, E., and Romales, E., 1996. Urban effects of convective precipitation in Mexico City. Atmospheric Environment, 30, 3383-3389.

Jury, M. R., Chiao, S., and Harmsen, E. W., 2009. Mesoscale structure of trade wind convection over Puerto Rico: composite observations and numerical simulation. Boundary-Layer Meteorology, DOI 10.1007/s10546-009-9393-3.

Kennaway, T., and Helmer, E. H., 2007. The Forest types and ages cleared for land development in Puerto Rico. GIScience & Remote Sensing, 44, 4, 356-382.

Kalnay, E., Kanamitsu, M., Kistler, R., Collins, W., Deaven, D., Gandin, L., Iredell, M., Saha, S., White, G., Woollen, J., Zhu, Y., Leetmaa, A., Reynolds, R., Chelliah, M., Ebisuzaki, W.,

Higgins, W., Janowiak, J., Mo, K.C., Ropelewski, C., Wang, J., Jenne, R., and Joseph, D., 1996. The NCEP/NCAR 40-year reanalysis project. Bulletin of the American Meteorological Society, 77, 437-471.

Landsberg, H. E., 1981. The urban climate. Academic Press, Maryland. 275 pp.

Lawton R. O., Nair, U. S., Pielke Sr., R. A., and Welch, R. M., 2001. Climatic impact of tropical lowland deforestation on nearby montane cloud forests. Science, 294, 584-587.

Lawton, R. O., Nair, U. S., Ray, D. K., Regmi, A., Pounds, A., and Welch, R. M., 2006. Quantitative measures of immersion in cloud and the biogeography of cloud forest. In Mountains in the Mist: Science for Conserving and Managing Tropical Montane Cloud Forest [L. A. Bruijnzeel et al., (Eds.)]. Univ. of Hawaii Press, Honolulu.

Lemonsu, A., Masson, V., and Berthier, E., 2007. Improvement of the hydrological component of an urban soil–vegetation–atmosphere–transfer model. Hydrological Processes, 21, 2100-2111.

Livezey, R. E., and Chen, W. Y., 1983. Statistical field significance and its determination by Monte Carlo techniques. Monthly Weather Review, 111, 46-59.

Lugo, A. E., and Helmer, E., 2004. Emerging forests on abandoned land: Puerto Rico's new forests. Forest Ecology and Management, 190, 145-161.

Luvall, J. C. and Holbo, H. R. 1989. Measurement of short-term thermal responses of coniferous forest canopies using thermal scanner data. Remote Sensing of Environment, 27, 1-10.

Luvall, J. C., Lieberman, D., Lieberman, M., Hartshorn, G. S., and Peralta, R., 1990. Estimation of tropical forest canopy temperatures, thermal response numbers, and evapotranspiration using an aircraft-based thermal sensor. Photogrammetric Engineering and Remote Sensing, 56, 1393-1401.

Luvall, J. C., 1997. The use of remotely sensed surface temperatures from an aircraft-based Thermal Infrared Multispectral Scanner (TIMS) to estimate the spatial and temporal variability of latent heat fluxes and thermal response numbers from a White Pine (Pinus strobus L.) plantation. In Scale in Remote Sensing and GIS [D. A. Quattrochi and M. F. Goodchild (Eds.)]. CRC Press, Boca Raton, FL, pp. 169-185.

Magaña, V., Amador, J. A., and Medina, S., 1999. The mid-summer drought over Mexico and Central America. Journal of Climate, 12, 1577-1588.

Malmgrem, B. A., Winter, A., and Chen, D., 1998. El Niño–Southern Oscillation and North Atlantic Oscillation control of climate in Puerto Rico. Journal of Climate, 11, 2713-2717.

Malmgren, B. A., and Winter, A., 1999. Climate zonation in Puerto Rico based on principal components analysis and an artificial neural network. Journal of Climate, 12, 977-985.

Mansell, M., and Rollet, F., 2006. Water balance and the behaviour of different paving surfaces. Water and Environment Journal, 20, 1, 7-10

Martilli, A., Clappier, A., and Rotach, M. W., 2002. An urban surface exchange parameterisation for mesoscale models. Boundary-Layer Meteorology, 104, 261-304.

Martinuzzi, S., Gould, W. A., Ramos González, O. M., 2007. Land development, land use, and urban sprawl in Puerto Rico integrating remote sensing and population census data. Landscape and Urban Planning, 79, 288-297.

Masson, V., 2000. A physically-based scheme for the urban energy budget in atmospheric models. Boundary-Layer Meteorology, 94,357-397.

Maurer, E. P., and Lettenmaier, D. P., 2003. Predictability of seasonal runoff in the Mississippi River basin. Journal of Geophysical Research, 108, 8607, doi:10.1029/2002JD002555.

McCarthy, M. P., Best, M. J., and Betts, R. A., 2010. Climate change in cities due to global warming and urban effects. Geophysical Research Letters, 37, L09705, doi:10.1029/2010GL042845.

Meehl, G. A., Stocker, T. F., Collins, W. D., Friedlingstein, P., Gaye, A. T., Gregory, J. M., Kitoh, A., Knutti, R., Murphy, J. M., Noda, A., Raper, S. B. C., Watterson, I. G., Weaver, A. J., and Zhao, C. Z., 2007. Global climate projections. In: Climate Change 2007: The Physical Science Basis. Contribution of Working Group I to the Fourth Assessment Report of the Intergovernmental Panel on Climate Change [Solomon, S., D. Qin, M. Manning, Z. Chen, M. Marquis, K.B. Averyt, M. Tignor and H.L. Miller (eds.)]. Cambridge University Press, Cambridge, United Kingdom and New York, NY, USA.

Melas, D., Ziomas, I. C., and Zerefos, C. S., 1995. Boundary layer dynamics in an urban coastal environment under sea breeze conditions. Atmospheric Environment, 29, 3605-3617.

Meyers, M. P., Walko, R. L., Harrington J. Y., and Cotton, W. R., 1997. New RAMS cloud microphysics parameterization. Part II: the two-moment scheme. Atmospheric Research, 45, 3-39.

Myers, N., Mittermeier, R. A., Mittermeier, C. G., da Fonseca, G. A. B., and Kent, J., 2000. Biodiversity hotspots for conservation priorities. Nature, 403, 853-858.

Nair, U. S., Lawton, R. O., Welch, R. M., and Pielke Sr. R. A., 2003. Impact of land use on Costa Rican tropical montane cloud forests: Sensitivity of cumulus cloud field characteristics to lowland deforestation. Journal of Geophysical Research, 108 (D7), 4206, doi:10.1029/2001JD001135.

Noto, K., 1996. Dependence of heat island phenomena on stable stratification and heat quantity in calm environment. Atmospheric Environment, 30, 475-485.

Ochi, S., Uchihama, D., Takeuchi, W., and Yasuoka, Y., 2002. Monitoring urban heat environment in East Asia. GIS development, 6, 10, 18-20.

Oke, T. R., 1987. Boundary layer climates. Routledge. 464 pp.

Pielke, R. A., and coauthors, 1992. A comprehensive meteorological modeling system-RAMS. Meteorology and Atmospheric Physics, 49, 69-91.

Pounds, A. J., Fogden, M. P. L., and Campbell, J. H., 1999. Biological response to climate change on tropical mountain. Nature, 389, 611-614.

Ragab, R., Rosier, P., Dixon, A., Bromley, J., and Cooper, J. D., 2003. Experimental study of water fluxes in a residential area: 2. Road infiltration, runoff and evaporation. Hydrological Processes, 17, 2423-2437.

Ray, D. K., Nair, U. S., Lawton, R. O., Welch, R. M., and Pielke Sr., R. A. 2006. Impact of land use on Costa Rican tropical montane cloud forests: Sensitivity of orographic cloud formation to deforestation in the plains. Journal of Geophysical Research, 111, D02108, doi:10.1029/2005JD006096.

Regional Atmospheric Modeling System, 1995. Technical description. Atmospheric, Meteorological, and Environmental Technologies. 50 pp.

Rickman, D. L., Luvall, J. C., and Schiller, S., 2000. An algorithm to atmospherically correct visible and thermal airborne imagery. Workshop on Multi/Hyperspectral Technology and Applications, Redstone Arsenal, Alabama.

Roberts, S. M., Oke, T. R., Grimmond, C. S. B., and Voogt, J. A., 2006. Comparison of four methods to estimate urban heat storage. Journal of Applied Meteorology and Climatology, 45, 1766-1781.

Ropelewski, C. F., and Halpert, M. S., 1996. Quantifying southern oscillation–precipitation relationships. Journal of Climate, 9, 1043-1059.

Rozoff, C. M., Cotton, W. R., and Odegoke, J. O., 2003. Simulation of St. Louis, Missouri, land use impacts on thunderstorms. Journal of Applied Meteorology, 42, 716-738.

Saleeby, M. S., and Cotton, W. R., 2004. A large-droplet mode and prognostic number concentration of cloud droplets in the Colorado State University Regional Atmospheric Modeling System (RAMS) Part I: module descriptions and supercell test simulations. Journal of Applied Meteorology, 43, 182-195.

Shepherd, J. M., and Burian, S. J., 2003. Detection of urban-induced rainfall anomalies in a major coastal city. Earth Interactions, 7, 1-17.

Shepherd, J. M., 2005. A review of current investigations of urban-induced rainfall and recommendations for the future. Earth Interactions, 9, 1-27.

Smith, T. M., and Reynolds, R. W., 2003. Extended reconstruction of global sea surface temperatures based on COADS data (1854–1997). Journal of Climate, 16, 1495-1510.

Smith, T. M., Reynolds, R. W., Peterson, T. C., and Lawrimore, J., 2008. Improvements to NOAA's historical merged land–ocean surface temperature analysis (1880–2006). Journal of Climate, 21, 2283-2296.

Stein, U., and Alpert, P., 1993. Factor separation in numerical simulations. Journal of the Atmospheric Sciences, 50, 2107-2115.

Still, C. J., Foster, P. N., and Schneider, S. H., 1999. Simulating the effects of climate change on tropical montane cloud forests. Nature, 389, 608-610.

Taylor, M. A., Enfield, D. B., and Chen, A. A., 2002. Influence of the tropical Atlantic versus the tropical Pacific on Caribbean rainfall. Journal of Geophysical Research, 107, 10.1-10.14.

Trenberth, K. E., Jones, P. D., Ambenje, P., Bojariu, R., Easterling, D., Klein Tank, A., Parker, D., Rahimzadeh, F., Renwick, J. A., Rusticucci, M., Soden, B., and Zhai, P., 2007. Observations: surface and atmospheric climate change. In: Climate Change 2007: The Physical Science Basis. Contribution of Working Group I to the Fourth Assessment Report of the Intergovernmental Panel on Climate Change [Solomon, S., Qin, D., Manning, M., Chen, Z., Marquis, M., Averyt, K. B., Tignor, M., and Miller, H. L. (eds.)]. Cambridge University Press, Cambridge, United Kingdom and New York, NY, USA.

Tso, C. P., 1996. A survey of urban heat island studies in two tropical cities. Atmospheric Environment, 30, 507-519.

Van der Molen, M. K., 2002. Meteorological impacts of land use change in the maritime tropic. PhD Thesis, Vrije Universititeit Amsterdam. 262 pp. (available at http://www.geo.vu.nl/~moli/

Van der Molen, M. K., Dolman, A. J., Waterloo, M. J., and Bruijnzeel, L. A., 2006. Climate is affected more by maritime then by continental land use change: a multiple scale analysis. Global and Planetary Change, 54, 128-149.

Velazquez-Lozada, A., Gonzalez, J. E., and Winter, A., 2006. Urban heat island effect analysis in San Juan, Puerto Rico. Atmospheric Environment, 40, 1731-1741.

Wilks, D. S., 2006. Statistical methods in the atmospheric sciences. International Geophysics Series, Vol. 59, Academic Press, 627 pp.

World Meteorological Organization, 1981. Guide to hydrological practices, vol. 1: data acquisition and processing. Geneva, Switzerland.

Appendix A

Regional Atmospheric Model Description

A.1 General Model Formulation

The Regional Atmospheric Modeling System uses the full set of non-hydrostatic, compressible equations that governs atmospheric dynamics and thermodynamics, and the conservation equations for scalar quantities, such as dry air, water vapor, and hydrometeor mixing ratios. It also includes a large selection of parameterizations available in the model. The post-processing component consists of the RAMS Evaluation and Visualization Utility (REVU), which accepts the gridded output from the model and generates files in different formats specified by the user to be visualized in a selection of graphical options. For this research, the processing, and many of the calculations (averages, differences, etc), were done in the Grid Analysis and Display System (GrADS), and the statistical analysis in the Matrix Laboratory (MATLAB).

The general equations used in RAMS are presented below; a full description of the atmospheric model can be found in the RAMS Technical Description (RAMS, 1995). All variables are grid-volume averaged quantities, where the over bar has been omitted. The horizontal and vertical transformations are also omitted for clarity.

Equations of motion:

$$\frac{\partial u}{\partial t} = -u\frac{\partial u}{\partial x} - v\frac{\partial u}{\partial y} - w\frac{\partial u}{\partial z} - \theta\frac{\partial \pi'}{\partial x} + fv + \frac{\partial}{\partial x}\left(K_m \frac{\partial u}{\partial x}\right) + \frac{\partial}{\partial y}\left(K_m \frac{\partial u}{\partial y}\right) + \frac{\partial}{\partial z}\left(K_m \frac{\partial u}{\partial z}\right) \tag{A.1}$$

$$\frac{\partial v}{\partial t} = -u\frac{\partial v}{\partial x} - v\frac{\partial v}{\partial y} - w\frac{\partial v}{\partial z} - \theta\frac{\partial \pi'}{\partial y} - fu + \frac{\partial}{\partial x}\left(K_m\frac{\partial v}{\partial x}\right) + \frac{\partial}{\partial y}\left(K_m\frac{\partial v}{\partial y}\right) + \frac{\partial}{\partial z}\left(K_m\frac{\partial v}{\partial z}\right)$$

$$\frac{\partial w}{\partial t} = -u\frac{\partial w}{\partial x} - v\frac{\partial w}{\partial y} - w\frac{\partial w}{\partial z} - \theta\frac{\partial \pi'}{\partial z} - \frac{g\theta_v'}{\theta} + \frac{\partial}{\partial x}\left(K_m\frac{\partial w}{\partial x}\right) + \frac{\partial}{\partial y}\left(K_m\frac{\partial w}{\partial y}\right) + \frac{\partial}{\partial z}\left(K_m\frac{\partial w}{\partial z}\right)$$

Thermodynamic equation, in term of the ice-liquid potential temperature (θ_{il}):

$$\frac{\partial \theta_{il}}{\partial t} = -u\frac{\partial \theta_{il}}{\partial x} - v\frac{\partial \theta_{il}}{\partial y} - w\frac{\partial \theta_{il}}{\partial z} + \frac{\partial}{\partial x}\left(K_h\frac{\partial \theta_{il}}{\partial x}\right) + \frac{\partial}{\partial y}\left(K_h\frac{\partial \theta_{il}}{\partial y}\right) + \frac{\partial}{\partial z}\left(K_h\frac{\partial \theta_{il}}{\partial z}\right) + \left(\frac{\partial \theta_{il}}{\partial t}\right)_{rad} \tag{A.2}$$

Water species mixing ratio continuity equations (n of them):

$$\frac{\partial r_n}{\partial t} = -u\frac{\partial r_n}{\partial x} - v\frac{\partial r_n}{\partial y} - w\frac{\partial r_n}{\partial z} + \frac{\partial}{\partial x}\left(K_h\frac{\partial r_n}{\partial x}\right) + \frac{\partial}{\partial y}\left(K_h\frac{\partial r_n}{\partial y}\right) + \frac{\partial}{\partial z}\left(K_h\frac{\partial r_n}{\partial z}\right) \tag{A.3}$$

Mass continuity equation:

$$\frac{\partial \pi'}{\partial t} = -\frac{R\pi_0}{c_v\rho_0\theta_0}\left(\frac{\partial \rho_0\theta_0 u}{\partial x} + \frac{\partial \rho_0\theta_0 v}{\partial y} + \frac{\partial \rho_0\theta_0 w}{\partial z}\right) \tag{A.4}$$

Each grid in RAMS is divided into patches in which surface sub-grid processes are calculated. Each patch is identified as water, bare soil (includes urban patches), or vegetated surface. The surface layer parameterization requires temperature values for these classes. For water surfaces, temperature is held constant as the initialization value for each simulation. For land surfaces, the surface values are provided by prognostic equations for bare soil and vegetated surfaces (shaded soil and vegetation canopy) as follows:

Potential temperature at surface for bare soil:

$$C_S \Delta z_g \frac{\partial \theta_g}{\partial t} = \alpha_g R_S \downarrow + R_l \downarrow - \sigma T_g^4 + \rho_a C_p u_* \theta_* + \rho_a C_p u_* r_* - C_S \lambda \frac{\partial \theta_S}{\partial z}|_g \quad \text{(A.5)}$$

Potential temperature at surface for vegetated surfaces (shaded soil):

$$C_S \Delta z_g \frac{\partial \theta_g}{\partial t} = \tau_{veg} \alpha_g R_S \downarrow + \sigma T_{veg}^4 - \sigma T_g^4 + \rho_a C_p u_* \theta_* + \rho_a C_p u_* r_* - C_S \lambda \frac{\partial \theta_S}{\partial z}|_g \quad \text{(A.6)}$$

Potential temperature for the vegetation layer:

$$C_{veg} \Delta z_{veg} \frac{\partial \theta_{veg}}{\partial t} = (1 - \tau_{veg}) \alpha_{veg} R_S \downarrow + R_l \downarrow + \sigma T_g^4 - 2\sigma T_{veg}^4 + 2\rho_a C_p u_* \theta_* + \rho_a C_p u_* r_* \quad \text{(A.7)}$$

Turbulent kinetic energy (TKE), *e*, defined as $e = \frac{1}{2}\left(u_i'^2\right)$; the prognostic equation for *e* is:

$$\frac{\partial e}{\partial t} = -u_j \frac{\partial e}{\partial x_j} + \frac{\partial}{\partial x_j} K_e \frac{\partial e}{\partial x_j} + P_s + P_b + \varepsilon \ , \quad \text{(A.8)}$$

where the shear (P_s) and buoyancy (P_b) production terms, and dissipation (ε) are given by:

$$P_s = K_m \left[\left(\frac{\partial u}{\partial x} \right)^2 + \left(\frac{\partial v}{\partial y} \right)^2 \right]$$

$$P_b = -\frac{g}{\theta} K_\theta \frac{\partial \theta_v}{\partial z} \quad \text{(A.9)}$$

$$\varepsilon = a_e \frac{e^{3/2}}{l}$$

The exchange coefficients for momentum, heat, and TKE are computed by:

$$K_m = S_m l \sqrt{2e} \quad \text{(A.10)}$$

$$K_\theta = S_\theta l\sqrt{2e}$$

$$K_e = S_e l\sqrt{2e},$$

where the turbulent mixing scale, l, is given by Mellor and Yamada (1982). In typical TKE models, S_m, S_θ, and S_e are a function of the Richardson number (Ri).

A.2 Description of Cloud Microphysics Module Water Categories

In RAMS water is categorized in nine forms: vapor, two cloud droplet categories, rain, pristine ice crystals, snow, aggregates, graupel, and hail. The last eight are the actual hydrometeor types and vapor is included for completeness. Cloud droplets and rain are liquid water, but super cooled. Pristine ice, snow and aggregates are assumed to be completely frozen, while graupel and hail are mixed-phase categories, capable of consisting of ice only or a mixture of ice and liquid.

Cloud droplets are assumed small enough not to fall, while all other categories do fall. Cloud droplets and pristine ice crystals are the only categories to nucleate directly from vapor, all other form from existing hydrometeors. Cloud water can also grow by auto conversion; this is the process by which raindrops initially form. Once formed, raindrops may also grow by vapor deposition and more importantly through collision-coalescence processes, in which raindrops collect cloud droplets and other smaller raindrops to grow larger.

Pristine ice crystals may also continue to grow by vapor deposition, and are not permitted to grow by any other process. The pristine ice and snow categories allow a bimodal representation of ice crystals sizes. Aggregates are defined as ice particles that formed by collision and coalescence of pristine ice, snow, and/or other aggregates. Pristine ice crystals, snow and aggregates are all low-density ice particles, having relatively low mass and fall speed for their diameters. Graupel is an intermediate density, mixed phase hydrometeor that is allowed to carry up to only a low percentage of liquid, ~30%. If this percentage becomes larger, graupel is re-categorized as hail, which is a high-density hydrometeor. Freezing raindrops or the partial melting of graupel forms hail, which is allowed to carry any fraction of liquid water up to 99%, but not 100% in which case it is re-categorized as rain.

Appendix B

Large-Scale Global Oscillations Teleconnection to Caribbean Climate

The Caribbean rainfall season, which spans from April to November, is characterized by a bimodal behavior. The two modes represent the early rainfall season (ERS, April – July) and the late rainfall season (LRS, August – November), separated by what is referred to as the mid-summer drought (MSD). This pattern is clearly observed in the island of Puerto Rico (Figure B.1) and in the rest of the Caribbean islands, Central America, and southern Mexico (Magaña et al., 1999; Chen and Taylor 2002, Angeles et al., 2010).

In Puerto Rico, a precipitation peak in May defines the ERS, precipitation is caused by differential heating and local transport of moisture uphill the Central Mountains, which provide the lifting mechanism (Comarazamy and González, 2008). The late season begins after the summer months and peaks in October. Included in the LRS is the hurricane season, occurring between June and November. The precipitation maximum in October occurs mostly due to enhanced low-level convergence to the east of the Lesser Antilles islands, low vertical wind shear, high sea surface temperatures, and greater amounts of deep layer moisture across the tropical North Atlantic (Taylor et al., 2002).

There are numerous studies that have addressed the relationship between warm ENSO events and dry LRS in the Caribbean (Hastenrath, 1976; Aceituno, 1988; Ropelewski and Halpert, 1996). The focus on the LRS is due to its abundance of rain and its coincidence with the hurricane season. It is precisely the relatively smaller amounts of rainfall during the ERS what makes it important, because even small variations in precipitation can lead to seasonal droughts or flooding. Recent studies have reported a strong positive relation between the early season Caribbean rainfall and warm ENSO events (Giannini et al., 2000; Giannini et al., 2001b; Taylor et al., 2002; Chen and Taylor, 2002). The correlation is such that warm winter anomalies in the ENSO index are related to positive ERS rainfall departures in the Caribbean basin one season after, the El Niño+1 years (Figure B.2). The teleconnection accounts for almost half of the season's precipitation variability. The propagation of the warm ENSO event into the Caribbean early rainfall season is attributed to positive spring North Tropical Atlantic (NTA) sea surface temperature anomalies (SSTA) that develop in response to the wintertime equatorial Pacific anomalies. The ERS, in addition to being correlated with winter Pacific SSTAs, also shows robust correlation with concurrent warm Caribbean SSTAs.

Numerical experiments performed with global circulation models (GCMs) show that the concurrent simulated state of the large-scale circulation for an increased early season rainfall is one characterized by lower than normal surface pressures, a warmer and convergent lower atmosphere, a divergent upper atmosphere, and a low shear environment. These atmospheric conditions are consistent with a region biased towards increased precipitation (Taylor et al., 2002; Angeles et al., 2010).

The relationship between NAO and the climate record was determined using the statistical Burnaby test, which gives rise to an E value (Burnaby, 1953). A significant positive E value indicates a direct relationship between the series, whereas a negative value indicates

an inverse relationship. Anomalies in Caribbean annual precipitation have been linked to the variability of the NAO index, where fluctuations in annual rainfall amounts are synchronous with variations in the wintertime NAO and are not controlled by ENSO (Figure B.3). The relation in Malmgren et al. (1998) was calculated using the winter NAO index and the standardized mean annual precipitation for five stations in Puerto Rico, and reported to be: $E_{NAO\text{-}Pcp}$= -0.91.

During years of high winter NAO index, when the axis of moisture transport in the North Atlantic changes to a southwesterly–northeasterly orientation, annual precipitation in Puerto Rico is lower than average. As the precipitation in the Caribbean is believed to be strongly influenced by the North Atlantic high, which is closely connected to the Icelandic low, the relationship between the NAO and precipitation patterns in the Caribbean may result from variations in displacement and strength of the high and the associated trade wind (Giannini et al., 2001a; Malmgrem et al., 1998).

As mentioned in Chapter 3, to reduce these large-scale influences in the simulation matrix in Table 3.1, the long-term ENSO and NAO indices record, archived by the Climate Prediction Center (CPC), was analyzed. Figures B.4 and B.5 show the 1950 to present ENSO and NAO dataset, respectively.

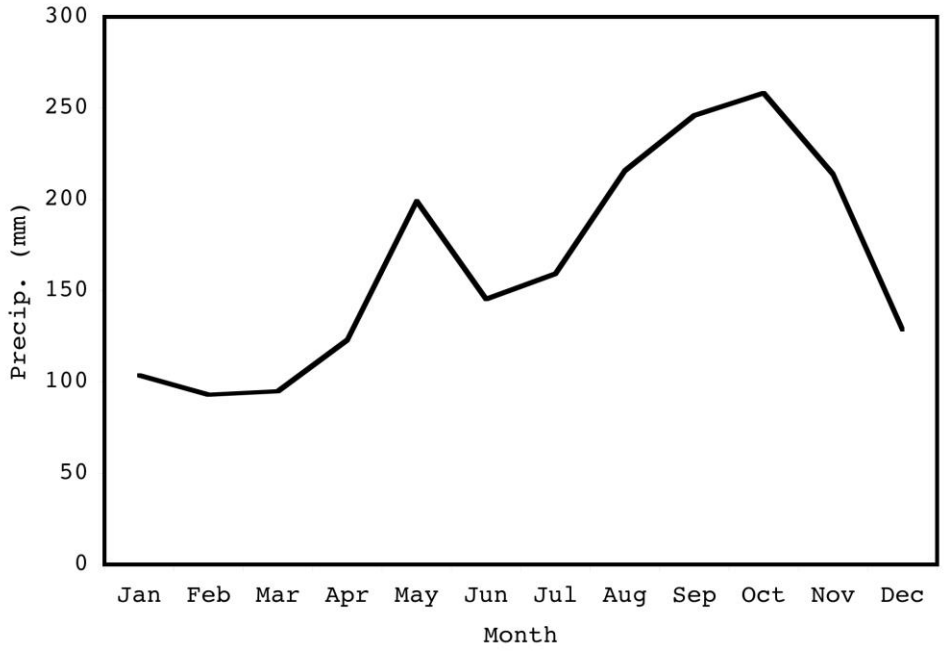

Figure B.1: 30-year (1970-2000) monthly precipitation climatology for 15 COOP stations distributed through out Puerto Rico (adapted from Comarazamy and González, 2008).

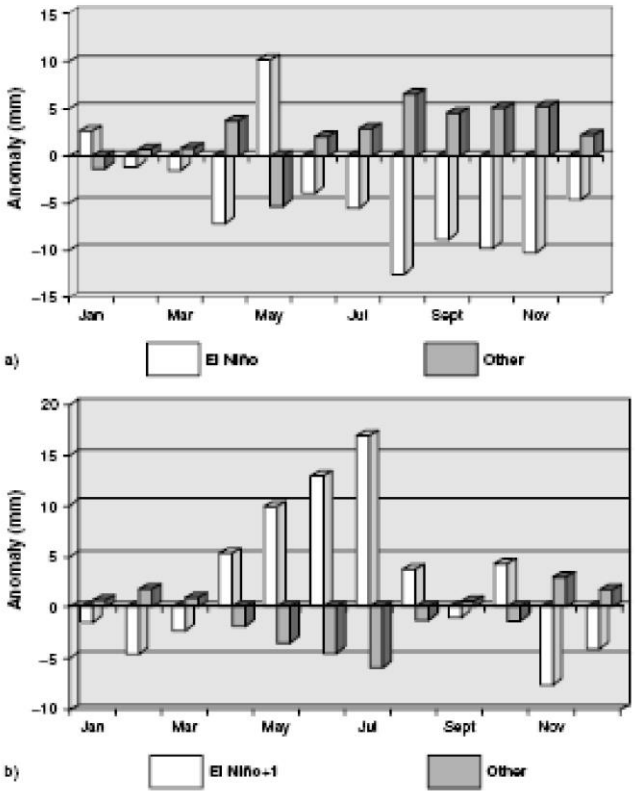

Figure B.2: Mean monthly Caribbean precipitation anomaly for El Niño years (white) versus other years (shaded), showing negative correlation between Caribbean rainfall and Pacific SSTs (top panel). Mean monthly precipitation anomaly for El Niño+1 years (white) versus other years (shaded), showing a tendency towards a wetter Caribbean in El Niño+1 years (bottom panel) (from Chen and Taylor, 2002).

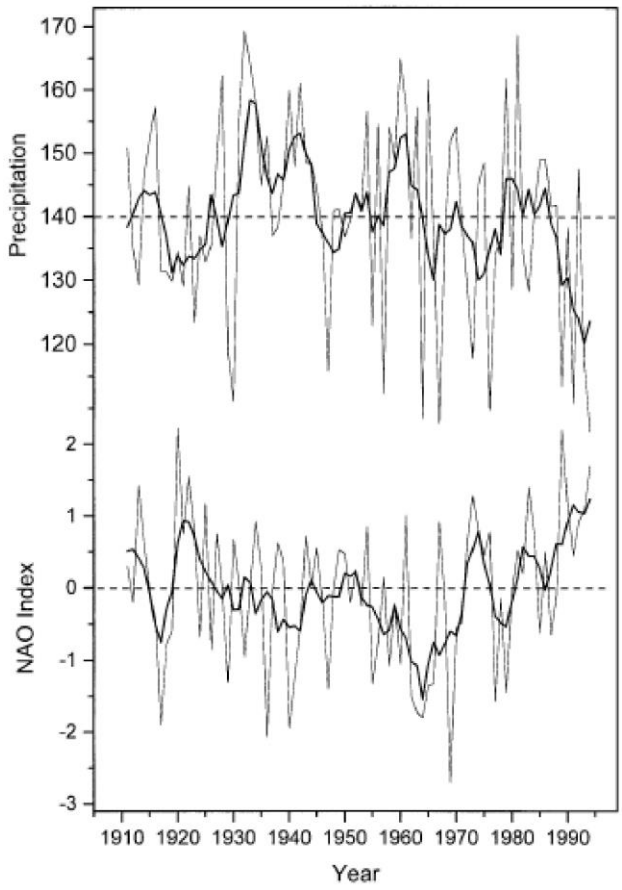

Figure B.3: Relationship between the winter (Dec–Mar) North Atlantic Oscillation index and mean annual precipitation over five climatic stations in Puerto Rico for the period 1911-1995. Thick lines represent five-point running averages (from Malmgren et al., 1998).

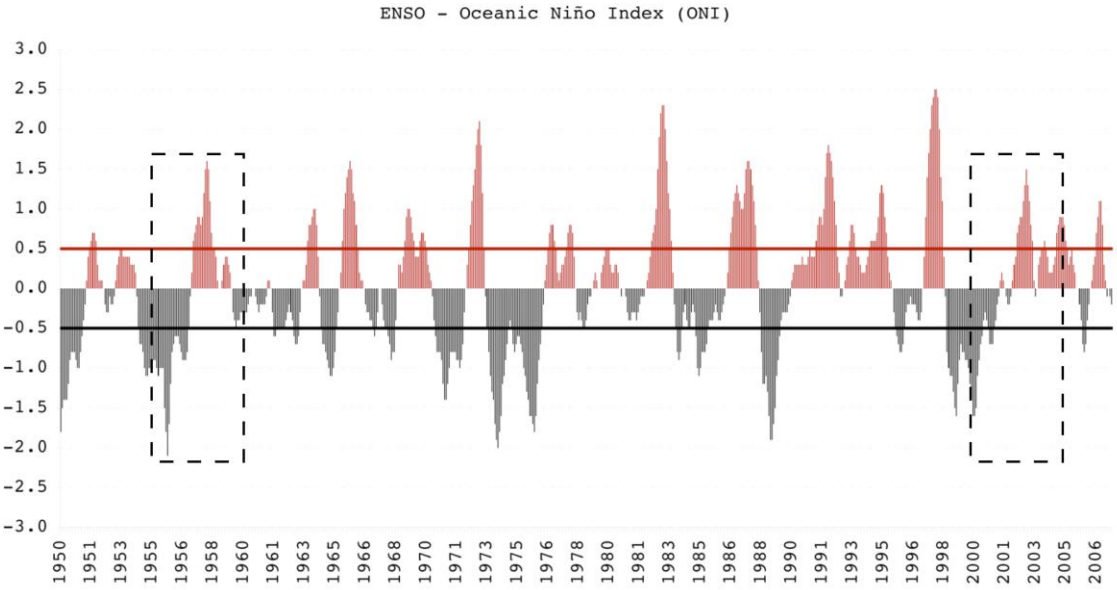

Figure B.4: Three-point running mean of the bimonthly Oceanic Niño Index (ONI) for 1950 to 2006, standardized departures from the 1950-1993 mean. Warm/cold periods, denominated as El Niño/La Niña respectively, occur when a +/-0.5˚C threshold is met for five consecutive overlapping periods as defined by the CPC, and are represented in red/black horizontal lines. Black dashed boxes represent the two timeframes selected for the simulations in Table 3.1.

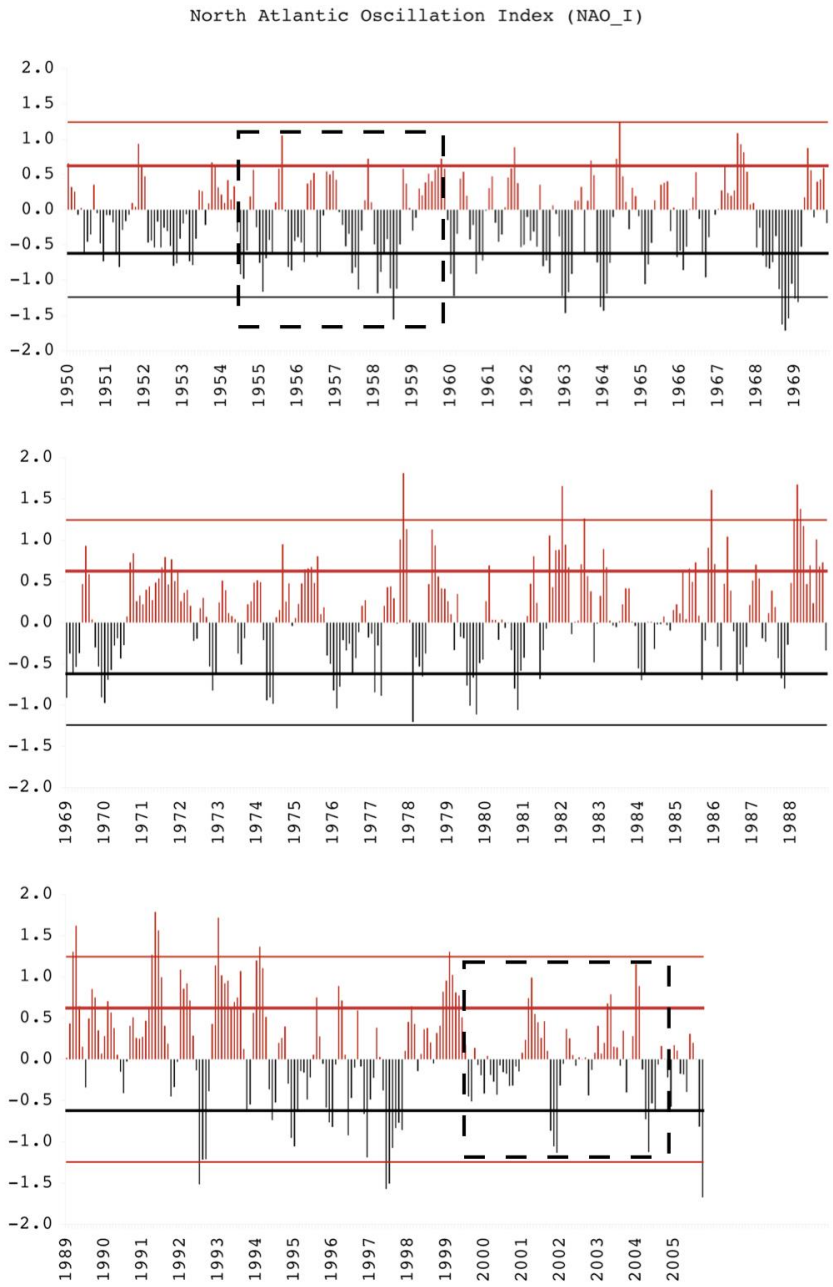

Figure B.5: Three-point running mean of the daily North Atlantic Oscillation Index (NAO_I) for 1950 to 2006, standardized departures from the 1950-2000 mean. Solid horizontal lines represent the standard deviation of the data, ±σ (± 0.6213) and ±2σ (±1.2427). Black dashed boxes represent the two timeframes selected for the simulations in Table 3.1

Appendix C

Table C.1: Biophysical Parameters by Land Use Class Number

#	Description	albedo	emiss	lai	vfrac	zo (m)	zdisp (m)	rootdep (m)
0	Ocean	.14	.99	0.0	.00	.00	0.1	.0
1	Inland Water	.14	.99	0.0	.00	.00	0.1	.0
2	Ice/Glacier	.40	.82	0.0	.00	.01	0.1	.0
3	Evergreen needleleaf tree	.10	.97	6.0	.80	1.00	15.0	1.5
4	Deciduous needleleaf tree	.10	.95	6.0	.80	1.00	20.0	1.5
5	Deciduous broadleaf tree	.20	.95	6.0	.80	.80	15.0	2.0
6	Evergreen broadleaf tree	.15	.95	6.0	.90	2.00	20.0	1.5
7	Short grass	.26	.96	2.0	.80	.02	.2	1.0
8	Tall grass	.16	.96	6.0	.80	.10	1.0	1.0
9	Desert	.30	.86	0.0	.00	.05	.1	1.0
10	Semi-desert	.25	.96	6.0	.10	.10	.5	1.0
11	Tundra	.20	.95	6.0	.60	.04	.1	1.0
12	Evergreen shrub	.10	.97	6.0	.80	.10	1.0	1.0
13	Deciduous shrub	.20	.97	6.0	.80	.10	1.0	1.0
14	Mixed woodland	.15	.96	6.0	.80	.80	20.0	2.0
15	Crop/mixed farming	.20	.95	6.0	.85	.06	.7	1.0
16	Irrigated crop	.18	.95	6.0	.80	.06	.7	1.0
17	Bog or marsh	.12	.98	6.0	.80	.03	1.0	1.0
18	Evergreen needleleaf forest	.06	.97	6.0	.80	.98	10.2	1.0
19	Evergreen broadleaf forest	.08	.95	6.0	.90	2.21	20.7	1.2
20	Deciduous needleleaf forest	.06	.95	6.0	.80	.92	9.2	1.0
21	Deciduous broadleaf forest	.09	.95	6.0	.80	.91	7.2	1.2
22	Mixed cover	.07	.96	6.0	.80	.87	6.5	1.1
23	Woodland	.08	.96	5.7	.80	.83	7.4	1.0
24	Wooded grassland	.18	.96	5.0	.80	.51	3.6	1.0
25	Closed shrubland	.10	.97	5.1	.63	.14	1.4	.7
26	Open shrubland	.12	.97	6.0	.22	.08	.2	.6
27	Grassland	.11	.96	2.6	.73	.04	.2	.7
28	Cropland	.10	.95	6.0	.84	.11	.2	.7
29	Bare ground	.16	.86	0.7	.07	.05	.2	.5
30	Urban and built up	.15	.90	4.8	.74	.80	1.1	.8
31	Urban1*	.13	.90	0.7	.07	.80	1.1	.5
32	Urban2*	.18	.90	0.7	.07	.80	1.1	.5
33	Urban3*	.23	.90	0.7	.07	.80	1.1	.5
34	Urban4*	.28	.90	0.7	.07	.80	1.1	.5
35	Urban5*	.33	.90	0.7	.07	.80	1.1	.5

* Additional Land cover/Land Use classes added for this study

Appendix D

Analysis Methods

The application of several statistical methods to the modeling results represents an important component of the research presented in this document. These methods include a factor separation technique to quantify the climate impacts of the two factors of interest for this work: LCLU changes and global warming. Then a two-sample hypothesis test was applied to the model results to assess the statistical significance of the difference in means obtained with the factor separation calculation.

D.1 Factor Separation

A simple method for calculating the interactions among various factors influencing the results of atmospheric models in sensitivity experiments was developed by Stein and Alpert (1993). This method includes the calculation of the individual contribution of each factor, as well as the combined contribution of the factors in question to the predicted total change in any given atmospheric field. To start, the method developed for n factors requires 2^n simulations, so to separate the contribution and possible interactions of LCLU changes and global warming, the four simulations in Table 3.1 are needed.

Now let a be any model predicted field that depends on initial and boundary conditions, as well as many model parameterizations and user specified options. If a change is made only on two of these input variables, ψ and ϕ multiplied by the changing coefficients b and c respectively, which can assume values of 1 and 0, depending if changes in the factor are taken into account, then a can be expressed mathematically as a constant part ($a\{\psi(0),\phi(0)\}$) and a part dependent on b and c ($\hat{a}\{\psi(b),\phi(c)\}$). In our case, $\psi(b)$ is the LCLU factor and $\phi(c)$ is the atmospheric condition factor, related to the changing coefficients they are expressed as:

$\psi(0) \rightarrow$ Past LCLU

$\psi(1) \rightarrow$ Present LCLU

$\phi(0) \rightarrow$ Past Atmospheric Conditions (D.1)

$\phi(1) \rightarrow$ Present Atmospheric Conditions

And the simulations in Table 3.1 as:

$$
\begin{aligned}
a\{\psi(1),\phi(1)\} &= \hat{a}\{\psi(1),\phi(1)\} + \hat{a}\{\psi(1),\phi(0)\} + \hat{a}\{\psi(0),\phi(1)\} + a\{\psi(0),\phi(0)\} \\
a\{\psi(1),\phi(0)\} &= \hat{a}\{\psi(1),\phi(0)\} + a\{\psi(0),\phi(0)\} \\
a\{\psi(0),\phi(1)\} &= \hat{a}\{\psi(0),\phi(1)\} + a\{\psi(0),\phi(0)\} \\
a\{\psi(0),\phi(0)\} &= \hat{a}\{\psi(0),\phi(0)\}
\end{aligned}
\qquad \text{(D.2)}
$$

In this formulation, $a\{\psi(0),\phi(0)\}$, the PAST2 scenario, is the control simulation, in which none of the factors ψ and ϕ are present, and it is equal to the constant part of a that is independent of the two factors being analyzed, $\hat{a}\{\psi(0),\phi(0)\}$. It is also important to be clear about the meaning of $\hat{a}\{\psi(1),\phi(1)\}$, $\hat{a}\{\psi(1),\phi(0)\}$, and $\hat{a}\{\psi(0),\phi(1)\}$. In that respective sequence they represent the fraction of a that is induced by the combination of ψ and ϕ, by ψ only, and by ϕ only. So to complete the formulation of the factor separation method, we solve for $\hat{a}$ in D.2 to obtain:

$$
\begin{aligned}
\hat{a}\{\psi(1),\phi(0)\} &= a\{\psi(1),\phi(0)\} - a\{\psi(0),\phi(0)\} \\
\hat{a}\{\psi(0),\phi(1)\} &= a\{\psi(0),\phi(1)\} - a\{\psi(0),\phi(0)\} \\
\hat{a}\{\psi(1),\phi(1)\} &= a\{\psi(1),\phi(1)\} - [a\{\psi(1),\phi(0)\} + a\{\psi(0),\phi(1)\}] + a\{\psi(0),\phi(0)\}
\end{aligned}
\qquad \text{(D.3)}
$$

To summarize, putting D.3 in terms of the simulation identification used throughout this document, the climate changes induced by LCLU changes is given by the operation (PRESENT2 – PAST2), the climate changes due to the global warming signal by (PAST1 – PAST2), and the combined contribution of LCLU changes and global warming to the total climate change by either [(PRES1 – PRES2) – (PAST1 – PAST2)] or [(PRES1 – PAST1) – (PRES2 – PAST2)]. In practice, the calculation of the non-linear interaction between the two factors involved in the research can be viewed either as the contribution of global warming to the climate impacts due to LCLU changes, or as the contribution of LCLU changes to the global warming signal. In either case, the result is the same; hence the value is exactly the same regardless of which viewpoint is taken.

D.2 Statistical Significance

The statistical significance test applied for this research considers two separate significance levels, local significance and field or global significance. Local significance is the test for statistical significance at individual grid points. A two-sample *t*-test is used to test the null hypothesis (H_0) that the data in the two vectors at a grid point are independent random samples from normal distributions with equal means and equal but unknown variances. The test returns the *p*-value of the test statistic

$$t = \frac{\bar{a}_1 - \bar{a}_2}{\left[\frac{var(a_1)}{n'_1} - \frac{var(a_2)}{n'_2}\right]^{1/2}}, \tag{D.4}$$

where *a* is any model predicted field with mean $\bar{a}_i$ and variance $var(a_i)$ over n'_i effective samples at each grid point. The effective size sample is calculated to account for the serial correlation of the underlying data and was determined by:

$$n'_i \cong n_i \frac{1-\rho_1}{1+\rho_1}, \tag{D.5}$$

where ρ_1 is the lag-1 serial autocorrelation coefficient.

The *p*-value is the probability, under the null hypothesis, that the calculated value of the test statistic will occur by chance. Therefore, the null hypothesis is rejected if the *p*-value is less than or equal to the test significance level (Wilks, 2006). The test significance level used throughout the analysis in Chapter 5, unless otherwise specified, is 95% ($\alpha_{LS} = 0.05$) so the 45˚ hatch marks in Figures 5.1-5.2 represent grid points of $0 \leq p \leq 0.05$.

After the local tests are performed, it still remains to test for the overall, collective, significance of the differences in means between the fields; this evaluation is called field significance. If we take for example the Total Change of maximum temperature (top right panel in Fig. 5.2), 89.51% of the land area reject H_0 at the 95% level, but what is the probability that this could have occurred by chance, or what percent of land area with significant changes would be equaled or exceeded by accident. These questions arise given the spatial correlation of the underlying data (Livezey and Chen, 1983; Elmore et al., 2006). Spatial correlation describes how variations in one grid point are reflected

at or by other grid points due to processes larger than the grid's horizontal resolution. To answer these questions, a null distribution of the percent of land area with significant test statistic results is needed.

Livezey and Chen (1983) propose a Monte Carlo method to develop such a distribution to test for field significance. In a Monte Carlo simulation, the experiment to be tested is duplicated with fictitious data generated in the same manner as the original, but in which the null hypothesis is true; it is then repeated many times with random inputs. The percent of grid points with statistically significant test statistic results at the α_{LS} level in each Monte Carlo calculation is plotted in a histogram and used to estimate a specified percent tail of the distribution and the threshold fraction required for field significance at a α_{FS} level. In this research $\alpha_{LS} = \alpha_{FS} = 0.05$, but different significance levels could by chosen in the local and field significance tests, depending on the physical nature of the data and the analyst's own preferences.

As mentioned above, the random inputs for the Monte Carlo experiments should be performed as to mimic the original data being tested to maintain the spatial correlation of the underlying data, whose effects are the main reason to test for field significance. Another important consideration is that enough simulations need to be performed to estimate the probability distribution accurately. To comply with the first consideration, a day from the PRESENT1 and PAST2 scenarios is chosen randomly with replacement, the resulting LAT-LON slice is assigned as day 1 in the alternative PRESENT1 and PAST2 sets, and the process is repeated n_i times until the two alternative datasets are completed. The test statistic D.4 is applied to the original and alternative datasets, and the percent of grid points with statistical significant results at α_{LS} is stored (pct_{LS}). The process is repeated 10 000 times with replacement, to comply with the second consideration. After all trials are completed, the percent of points with significant differences (pct_{FS}) is plotted in a histogram and the $(1 - \alpha_{FS})$ quantile of percentages is determined. If the percent of grid points showing significant differences is larger than this threshold, then the difference in means observed has field significance. This procedure has been applied in the past to situations where the local significance analysis of the historical and fictional

datasets clearly represented an acceptance of H_0 (Livezey and Chen, 1983; Maurer and Lettenmaier, 2003; Feddema et al., 2005; Elmore et al., 2006).

The entire statistical significance determination process can be summarized as follows:

1) Local significance:
    a. *t*-tests are performed to determine the statistical significance of the difference in means between two scenarios in Table 3.1.
    b. The percent of grid points over land regions with statistically significant test statistic results below the α_{LS} level is determined.
2) Field significance:
    a. The Monte Carlo method developed by Livezey and Chen (1983) is used to estimate the distribution of the percent of points that would show significant differences by chance.
    b. The percent of points with significant differences (pct_{LS}) is compared with the upper α_{FS} quantile of pct_{FS} from the Monte Carlo trials to determine if the differences in mean have field significance.

The fraction of land area from Figures 5.1-5.2 with significant differences in means at the 95% confidence level, (pct_{LS}), along with the required percent for field significance, is summarized in Tables D.1 and D.2 for maximum and minimum temperatures, respectively. Clearly the results for difference in means in maximum and minimum temperatures are located well out of the upper tail, and therefore are considered to have field significance. A more adequate re-sampling technique for this case should be explored, since the procedure performed seems to generate alternative datasets that do not show the level of randomness observed in the fictitious sets generated for similar field significance tests in previous studies.

Table D.1: Local and Field Statistical Significance Results for Maximum Temperature

Land % Required for Field Significance	
95% Tail – PRESENT1 = 7.08; PAST2 = 7.46	
Local Significance	
Scenario	**% of Land Area**
PRESENT1 – PAST2	89.51
PRESENT1 – PAST1	76.00
PRESENT2 – PAST2	75.43
PRESENT1 – PRESENT2	78.55
PAST1 – PAST2	81.32
(PRE1 – PAS1) – (PRE2 – PAS2)	36.48

Table D.2: Local and Field Statistical Significance Results for Minimum Temperature

Land % Required for Field Significance	
95% Tail – PRESENT1 = 4.57; PAST2 = 5.33	
Local Significance	
Scenario	**% of Land Area**
PRESENT1 – PAST2	95.05
PRESENT1 – PAST1	62.90
PRESENT2 – PAST2	58.76
PRESENT1 – PRESENT2	93.58
PAST1 – PAST2	90.18
(PRE1 – PAS1) – (PRE2 – PAS2)	41.48

Appendix E

Publications

Comarazamy, D. E., González, J. E., Luvall, J. C., Rickman, D. L., and Mulero, P. J., 2010. A Land–Atmospheric Interaction Study in the Coastal Tropical City of San Juan, Puerto Rico. Earth Interactions, 14, 1–24, doi: 10.1175/2010EI309.1

González, J. E., Luvall, J. C., Rickman, D., Comarazamy, D. E., and Picón, A. J., 2006. Urban heat island identification and climatological analysis in a coastal, tropical city: San Juan, Puerto Rico. In: Urban Remote Sensing [Q. Weng and D. Quattrochi (Eds.)]. CRC Press, Boca Raton, FL, pp. 223-252.

González, J. E., Luvall, J. C., Rickman, D., Comarazamy, D. E., Picón, A. J., Harmsen, E. W., Parsiani, H., Ramírez, N., Vázquez, R., Williams, R., Waide, R. B., and Tepley, C. A., 2005. Urban heat islands developing in coastal tropical cities. EOS Transactions, AGU, 86, 42, pp. 397 & 403.